Gas-Phase Spectroscopic Studies on Energetics and Reactions of Transition-Metal Complexes

Ph.D. dissertation

Ágnes Rokobné Révész

Advisor:

Dr. Bálint Sztáray, Ph.D.
Associate Professor
University of the Pacific, Stockton, CA

Consultants:

Prof. László Szepes, D.Sc.
Eötvös Loránd University, Budapest

Dr. Detlef Schröder, Ph.D. habil.
Institute of Organic Chemistry and Biochemistry, AS CR, Prague

Eötvös Loránd University, Budapest

Doctoral School of Chemistry
Head of School: Prof. György Inzelt, D.Sc.

Theoretical and Physical Chemistry,
Structural Chemistry Ph.D. Program
Head of Program: Prof. Péter Surján, D.Sc.

2011

Contents

Introduction

The importance of transition-metal complexes in various fields of chemistry would be hard to overestimate; prominent examples may be biochemistry and industrial catalytic processes. The stability, catalytic activity and selectivity of these compounds depend on the nature of the metal center, its redox state, as well as the steric and electronic properties of the ligands. Knowledge of their dissociation kinetics and energetics, especially the metal–ligand bond energies could significantly support our understanding of structure–property relationships. However, accurate data about thermochemistry and ionic bond energies of transition-metal complexes are usually not available; experiments aimed at determination of these are therefore of great value.

During my Ph.D. work, I have been involved in studying model compounds using two techniques: threshold photoelectron photoion coincidence spectroscopy (TPEPICO) and ion-trap mass spectrometry (IT-MS). The former is the combination of photoelectron spectroscopy and mass spectrometry, and it is a useful tool in investigating the unimolecular dissociation of energy selected ions in the gas phase. Fragmentation pathways, accurate bond energies, and heats of formation of the ions and neutral molecules can be determined. The latter is a widely used mass spectrometer type, and its connection to an electrospray ionization (ESI) source allows the gas-phase investigation of species that are present in solution.

The observed trends in dissociation energies can often be explained in terms of the varying electronic structure or coordination sphere, which may deepen the understanding of the role played by the ligands. These data and the fragmentation pathways as well can indirectly help in answering questions about reaction mechanisms, which might be of interest for a wider community.

The chemistry of transition-metal complexes is a huge field; in this thesis, I focus on four selected topics. The first of them is the effect of *carbonyl–chalcocarbonyl change*. Complexes containing carbonyl ligands are not only interesting from a theoretical point of view due to the "prototypical" metal–carbonyl bonding, but they are also widely used in catalytic reactions as well as in chemical vapor deposition. The usual starting step for the formation of the catalytically active, coordinatively unsaturated species is the metal–carbonyl bond rupture. We investigated the effect of replacing carbonyls with carbon monosulfide (CS) or carbon monoselenide (CSe) on the bond energies by TPEPICO measurements. These ligands differ in their electronic properties

from CO, and although being unstable molecules, they can be stabilized as ligands in transition-metal complexes. The model compounds chosen in this work were the chalcocarbonyl analogues of $CpMn(CO)_3$ (Cp = cyclopentadienyl, C_5H_5).

Metallocenes and their derivatives also represent a particularly important class of organometallic complexes. However, their thermochemistry is not well known and the *ionic bond energies* found in the literature show considerable uncertainties. The mechanism, energetics and kinetics of the ionic dissociation processes of manganocene were investigated earlier in our laboratory by photoelectron photoion coincidence spectroscopy. In this thesis, I present the TPEPICO investigation of chromocene, cobaltocene and nickelocene. The $[CpM–Cp]^+$ bond dissociation energies were determined and the accompanying dissociation and isomerization pathways were revealed. The experimental data were analyzed using two different theoretical approaches, and the results were compared. The relation between the trends in the M–Cp bond energies along the Cr . . . Ni series and the electronic structures of the metallocene ions determined in previous photoelectron studies is also discussed.

Pyridine complexes can serve as a model for the biologically relevant interactions between transition metals and histidine residues. The gas-phase chemistry of copper(I) ions with pyridine has been investigated quite thoroughly, consequently in this thesis we focused on the influence of this ligand on the stability of gaseous *copper(II)* species, using ESI-IT-MS experiments. The observed trends in dissociation energies and fragmentation pathways are explained as a response of the Cu^{I}/Cu^{II} redox couple to the changes of the coordination sphere. Furthermore, the measurements indicate the possibility of the determination of approximate fragmentation thresholds using IT-MS.

Copper-catalyzed oxidations form the basis of several key synthetic processes, both in the laboratory and on industrial scale. The possible use of *disulfides* as electron acceptors in these reactions has recently enjoyed growing attention. In this work, the intramolecular oxidation of imines featuring a nearby disulfide group was investigated with ESI-IT-MS in order to identify possible intermediates and reveal the mechanism of the reaction, with particular emphasis on the number of the copper atoms involved in the reaction and their oxidation state. This last part of my thesis presents results from an area slightly different from the three previous ones, which indicates the necessity and utility of this type of experiments for a broader field of chemistry.

Acknowledgements

During my Ph.D. studies, I received support from several people, without which this work could not have been done. Here, I would like to express my grateful thanks:

- to my advisor, Dr. Bálint Sztáray;
- to my consultants, Prof. László Szepes and Dr. Detlef Schröder;
- to Prof. Tomas Baer;
- to the team of the laser center CLIO;
- to all members of the research groups at Budapest, Chapel Hill and Prague;
- to my husband, my family, and my friends.

I highly appreciate financial support from the following institutions:

- Richter Gedeon Centenary Foundation;
- Hungarian Science Research Fund, grants F61153, T032489, NN71044, F60679;
- U.S. National Science Foundation;
- U.S. Department of Energy;
- Academy of Sciences of the Czech Republic, grant Z40550506;
- Grant Agency of the Academy of Sciences of the Czech Republic, grant KJB400550704;
- Grant Agency of the Czech Republic, grants 203/08/1487, 203/08/1318;
- Ministry of Education of the Czech Republic, grant MSM0021620857.

Notations and Abbreviations

AC	alternating current
AE	(visual) appearance energy
AE_0	zero-kelvin appearance energy ($IE_{\mathrm{ad}} + BDE$)
Ar	aryl [group]
BDE	bond dissociation energy
BR	branching ratio
BSSE	basis set superposition error
CID	collision-induced dissociation
CVD	chemical vapor deposition
Cp	cyclopentadienyl [group]
DFT	density functional theory
EI	electron ionization
ESI	electrospray ionization
FT-ICR	Fourier transform ion cyclotron resonance
FWHM	full width at half maximum
h	Planck constant
H°	enthalpy at standard pressure
$\Delta_{\mathrm{f}}H^\circ$	heat of formation
$\Delta_{\mathrm{r}}H^\circ$	reaction enthalpy
IE	ionization energy
IE_{ad}	adiabatic ionization energy
IR	infrared [spectroscopy]
IT-MS	ion-trap mass spectrometry
k_{B}	Boltzmann constant
KS-DFT	Kohn–Sham DFT
MO	molecular orbital
MS	mass spectrometry
NMR	nuclear magnetic resonance [spectroscopy]
PES	photoelectron spectoscopy
PE	photoelectron [spectrum]
PST	phase space theory
py	pyridine

RAC-RRKM	rigid activated complex RRKM
RRKM	Rice–Ramsperger–Kassel–Marcus [theory]
SACM	statistical adiabatic channel model
SSACM	simplified statistical adiabatic channel model
TCID	threshold collision-induced dissociation [experiments]
TOF	time-of-flight
TPEPICO	threshold photoelectron photoion coincidence [spectroscopy]
TS	transition state
VTST	variational transition state theory
VUV	vacuum ultraviolet [light]
ZPVE	zero-point vibrational energy

In all the figures showing molecular geometries, the following atom coloring is used: carbon, hydrogen, sulfur, copper, nitrogen, oxygen, chlorine. Selected bond lengths are given in ångströms.

Chapter 1

Literature Overview and Aims of the Present Work

1.1 Chalcocarbonyl Complexes

Carbon monoxide is undoubtedly one of the most important and most widely studied ligands in organometallic chemistry. It was more than hundred years ago that the first binary metal carbonyl complex ($Ni(CO)_4$) was successfully prepared by Mond et al. [1]. The long and continuous interest in the CO ligand and its compounds is not unjustified. Transition-metal carbonyls are frequently used as starting materials in the synthesis of other metal complexes. Metal carbonyl derivatives futhermore play an important role as intermediates in homogeneous catalysis (e.g., in the hydroformylation process) [2].

CO can be considered as the prototype of σ-donor, π-acceptor ligands. The qualitative description of the bonding between the metal center and the CO molecule consists of two interactions (see Figure 1.1): donation of the lone pair of CO into a suitably directed vacant orbital on the metal forming a σ bond, and accompanying π-type back-donation from an occupied metal orbital into an empty antibonding CO orbital [2,3]. As a result, only metals in the center of the *d* block have stable neutral binary carbonyl derivatives, because they have low-lying empty orbitals to accept σ-donated lone pairs and also filled *d* orbitals for π back-donation. Outside this area, carbonyl compounds need additional ligands besides CO for stabilization (e.g., $Cp_2Ti(CO)_2$).

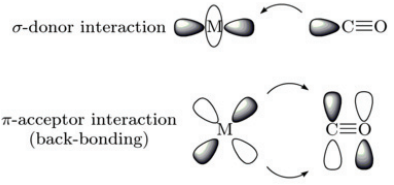

Figure 1.1: The interactions establishing the bonding in metal carbonyls [2,3]

σ bonding slightly strengthens, while π back-bonding markedly weakens the carbon–oxygen bond; the net weakening is manifested in the decrease of the C–O stretching frequency in the infrared (IR) spectrum of transition-metal carbonyls compared to free CO. On the other hand, complexes of CO with main-group Lewis acids incapable of π back-bonding show the expected blue shift of the IR absorption (see Table 1.1).

Table 1.1: Effect of σ donation and π back-donation on the CO stretching vibration [2,4]

Compound	Position of CO absorption band (cm^{-1})
free CO	2143
$Ni(CO)_4$	2060
H_3BCO	2165

Apart from acting as a terminal ligand, the carbonyl also engages in a range of other bonding modes in metal carbonyl cluster chemistry. Compounds have been synthesized having CO in an unsymmetrical or symmetrical bridging position between two metals (μ_2-CO), or even as triply bridging ligand (μ_3-CO). Much less common bonding modes are in which both C and O bound to one or two metal atoms. Figure 1.2 shows several examples for the typical bonding modes. The increased π back-bonding from multiple metal centers results in further weakening of the C–O bond [2,3].

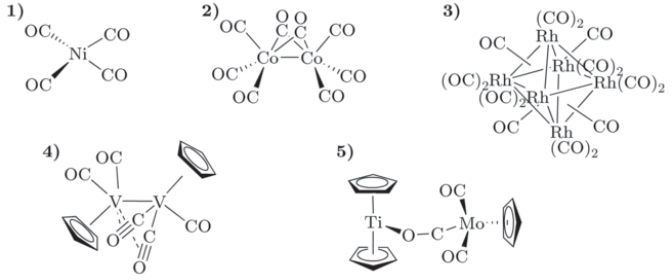

Figure 1.2: The coordination modes of the CO ligand: **(1)** terminal CO (η^1-CO), **(2)** doubly bridging CO (μ_2-η^1:η^1-CO), **(3)** triply bridging CO (μ_3-η^1:η^1:η^1-CO), **(4)** unsymmetrical, σ/π bridging type (μ_2-η^1:η^2-CO) and **(5)** [M]-CO-[M′] bridging form (μ_2-κC:κO-CO) [2,5]

Upon substituting heavier chalcogens for the oxygen atom, homologues of CO can be obtained, such as CS and CSe. Due to the diminished tendency of heavier main-group elements to form π bonds [6], they are unstable under ordinary conditions, but they have been subject of several theoretical and *in situ* spectroscopic studies [7–9]. Carbon monosulfide is a very reactive species even at −196 °C; it reacts with the other chalcogens and with halogens to give CSE (E = Se, Te) and CSX_2 (X = Cl, Br) [10–12]. At room temperature, it forms a brown CS polymer [10]. It can be synthesized by high-frequency electrical discharge from CS_2 or with photolysis [11,13]. The properties of CSe are similar to those of CS [12].

Although CS and CSe as monomers are unstable at room temperature, a number of transition-metal complexes with chalcocarbonyls as ligands are known [2,3]. They are considered as stronger σ donors and π acceptors [14–17]. The known coordination modes (like in the case of CO) include terminal, bridging and polyhapto versions; apparently, CS is even more suited as a bridging ligand than CO [2,18].

Transition-metal carbonyls are used as catalysts in various chemical reactions, including several transformations of industrial relevance. Characteristic examples of such processes are the $HCo(CO)_4$ catalyzed olefin isomerization [2,19], the hydroformylation of olefins leading to aldehydes using $HCo(CO)_4$ or $HRh(CO)_2(PPh_3)_2$ [20,21] and the Reppe synthesis of acrylic acids or esters from acetylene, CO, and ROH, for which appropriate catalysts may be $HCo(CO)_4$, $Ni(CO)_4$, or $Fe(CO)_5$ [2]. As exemplified by the catalytic cycle of the hydroformylation shown in Figure 1.3, the usual starting step

for the formation of the catalytically active, coordinatively unsaturated species is the metal–carbonyl bond cleavage. The thermochemistry of the carbonyl complexes, and especially the transition metal–carbonyl bond energies, are thus of great importance in catalyst design. Effect of other ligands on the M–CO bonds can also be of interest. In this respect, the consequences of replacing a coordinated CO ligand with its analogues containing heavier chalcogens may be worth closer studying.

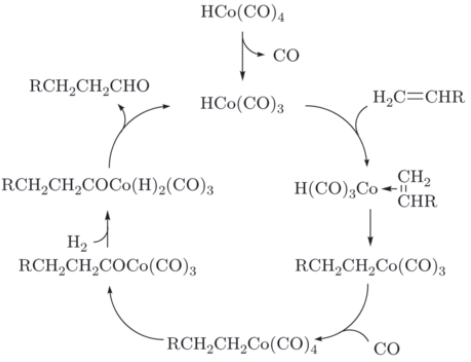

Figure 1.3: The catalytic cycle of hydroformylation [2]

However, thermochemistry data of the chalcocarbonyl complexes are scarce in the literature. Reactivity of several thiocarbonyl complexes [22–24] compared to their carbonyl analogues suggest that the $[M–CS]^+$ bond is stronger than $[M–CO]^+$. Several thiocarbonyl complexes have been studied by electron ionization (EI) mass spectrometric (MS) experiments [18, 25–29], and the fragmentations showed that the thiocarbonyl ligand forms a stronger bond to the transition-metal center than the carbonyl ligand. By comparing the appearance energies (*AE*s) of fragments from $M(CO)_6$ molecules with those from the analogous $M(CO)_5CS$ (M = Cr, Mo, W) complexes [25], it was found that the $[M–CS]^+$ dissociation energy is 1.5–2.0 eV larger than that of the $[M–CO]^+$ bond. The EI mass spectrometric study of $CpMn(CO)_3$, $CpMn(CO)_2CS$ and $CH_3C_5H_4Mn(CO)_3$, $CH_3C_5H_4Mn(CO)_2CS$ complexes [27] provided $[CpMn–CO]^+$ = (2.39 ± 0.04) eV and $[CpMn–CS]^+$ = (3.00 ± 0.03) eV bond energies, as well as (2.20 ± 0.04) eV and (3.05 ± 0.01) eV for the methyl-substituted analogues. However, due to the neglect of the thermal energy distribution of the sample and the low energy resolution of the EI experiment, these values may be in significant error. Furthermore, the slow dissociation dynamics were also neglected in the data analysis. The gas-phase reactions of bare transition-metal ions with CS_2 yielding two major products, MS^+ and MCS^+ (M = Sc, Ti [30], V, Mo [31], Fe [32] Y, Zr, Nb [33]), were investigated with guided ion beam and Fourier transform ion cyclotron resonance (FT-ICR) mass spectrometry. Analysis of the MCS^+ cross-sections provided values for

$[M–CS]^+$ dissociation energies. Quantum chemical calculations also indicate stronger M–CS bonds [34–36], in line with experimental results.

There are even less data on the thermochemistry and gas-phase ion energetics of selenocarbonyl complexes and their fragments. IR and Raman experiments on $Cr(CO)_5CSe$ and $MeO_2C(C_6H_5)Cr(CO)_2CSe$ suggested that the Cr–CSe bond is stronger than the Cr–CS bond [37], nevertheless, accurate bond dissociation energies and heats of formation are not available in the literature.

In the past few years, our group has investigated the gas-phase thermochemistry of a number of transition-metal carbonyls, such as $CpMn(CO)_3$ [38], $CpCo(CO)_2$ [39], $C_6H_6Cr(CO)_3$ [40] and $Co(CO)_3NO$ [41] using the TPEPICO technique, and it was demonstrated that this is a useful tool in determining accurate bond dissociation energies. For $CpMn(CO)_3^+$, sequential loss of the three COs was observed:

$$CpMn(CO)_3^+ \longrightarrow CpMn(CO)_2^+ \longrightarrow CpMnCO^+ \longrightarrow CpMn^+,$$

which made possible to determine $[CpMn(CO)_x–CO]^+$ bond energies (obtained values are (1.11 ± 0.04) eV, (0.63 ± 0.04) eV and (1.08 ± 0.06) eV for $x = 2$, 1 and 0, respectively).

The synthesis of chalcocarbonyl analogues of $CpMn(CO)_3^+$ is known in the literature. $CpMn(CO)_2CS$ and $CpMn(CO)_2CSe$ are both air-sensitive, yellow, crystalline solids. The compounds have been characterized by various spectroscopic techniques (NMR, MS, IR) [16, 27, 42–46]. The first He I photoelectron spectrum (PE spectrum) of $CpMn(CO)_2CS$ was taken by Lichtenberger and coworkers [47]. Recently, we have undertaken a He I and He II photoelectron spectroscopic (PES) study of this compound, and with the aid of quantum chemical calculations, proposed a new ordering of the molecular energy levels, and by that means a new assignment for the PE spectrum [48].

Our aims in this thesis were to carry out a detailed TPEPICO study of the $CpMn(CO)_2CS$ and $CpMn(CO)_2CSe$ model compounds, in order to determine the metal–chalcocarbonyl bond energies and obtain insight into the effect of chalcocarbonyl substitution on the bonding of other ligands to the metal center.

1.2 Metallocenes

π-donor complexes are characterised by L→M donor as well as L←M acceptor interactions involving ligand orbitals that exhibit π symmetry with respect to the ligand. Probably the most important member of the family of cyclic π-donor ligands is the cyclopentadienyl ligand.

The first cyclopentadienyl (Cp) metal compound was prepared as early as in 1901 by Thiele [49]. Half a century passed before the C_5H_5 ligand again came into the focus of interest with the discovery of ferrocene (Cp_2Fe) [50]. At that time, the structure of ferrocene was conceptually new and presented significant challenge to the theory of chemical bonding [51–53].

By now, the chemistry of Cp complexes has immensely widened and the known Cp-containing compounds show high diversity of structures. As a π-donor ligand, the haptocity of Cp is usually 5, but it can also act as a η^3 or even a η^1 ligand, the latter by forming an M–C σ bond. Mixed complexes are sometimes obtained; such complexes are often found to be fluxional in solution at room temperature [2, 3, 54]. C_5H_5 compounds having η^5 coordination can be further classified, e.g., to correspond to one of the five basic types: 1. parallel sandwich complexes (metallocenes), 2. multidecker sandwich complexes, 3. half-sandwich complexes, 4. bent or tilted sandwich complexes and 5. complexes with more than two Cp ligands (see Figure 1.4) [54].

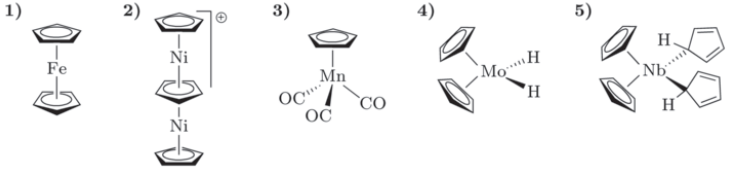

Figure 1.4: Examples of the five types of Cp complexes: **(1)** parallel sandwich complex, **(2)** multidecker sandwich complex, **(3)** half-sandwich complex, **(4)** bent or tilted sandwich complex and **(5)** complex with more than two Cp ligands [54]

Being the analogues of the archetypal ferrocene (orange), dicyclopentadienyl metal compounds of the neighbouring 3*d* elements may be regarded as the conceptually simplest Cp-containing systems. Chromocene (scarlet), manganocene (brown), cobaltocene (purple) and nickelocene (green) have all been prepared as neutral molecules, having melting points of about 170 °C. They possess the same structure and similar bonding as ferrocene with different number of valence electrons. Cobaltocene and nickelocene have more electrons than the stable ferrocene, they can thus be oxidised easily, even by air; while chromocene has less electrons and tends to bind additional ligands that will contribute extra electrons. All these metallocenes except manganocene are known to show strong covalent bonding between the metal and the rings. These metal–Cp bonds are only weakly polar; the compounds do not react like polar organometallic species [2, 54]. Cp_2Mn is very reactive, air-sensitive and considered partially ionic in character. Metallocenes have been studied using a variety of experimental methods; for example, there are several He I photoelectron spectroscopic studies providing vertical ionization energy (*IE*) values and electronic configurations for the metallocene ions [55–57].

The principles of the transition metal–Cp bond in metallocenes is easily illustrated in a molecular orbital (MO) picture. The 5 p_z orbitals on the planar C_5H_5 group can be combined to produce 5 π-type group molecular orbitals. Together with a similar set from the second C_5H_5 group, linear combinations adapted to the full molecular symmetry (D_{5d}) of the metallocene can be obtained. These can then overlap with metal orbitals having appropriate symmetry properties, giving the MOs of the molecule.

Donation and back-donation type interactions are both involved in the bond formation between the metal and the $C_5H_5^-$ anion, much like in the case of the CO ligand, but donation yields σ and π, back-donation gives δ bonding in this case. Figure 1.5 depicts the most important donor and acceptor interactions in metallocenes [54, 58].

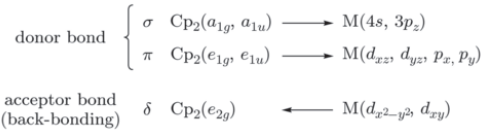

Figure 1.5: Schematic diagram of the metal–ligand interactions in metallocenes [54, 58]

To date, metallocenes and their derivatives have become a particularly important class of organometallic complexes also from a practical point of view. For example, they are widely used as catalysts in polymerization reactions [2, 59–64] and as precursors in chemical vapor deposition (CVD) [65–69]. Besides these two prevailing uses, metallocene derivatives are known to be important nonlinear optical materials, metallocene-containing polymers have emerged as a notable category of polymeric materials and some of the bent metallocene derivatives have antitumor activity [2, 54]. In addition, chiral derivatives of metallocenes have been recognized as useful chiral ligands in many stereoselective syntheses (see Figure 1.6) [2, 54].

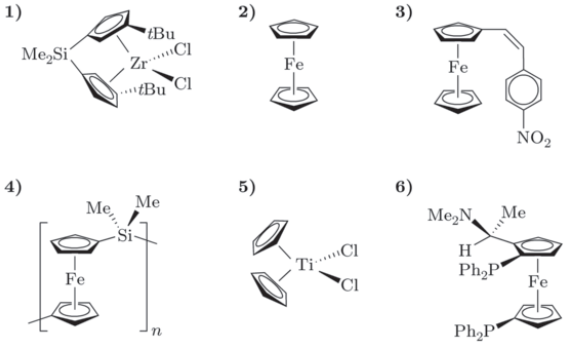

Figure 1.6: Examples for the uses of metallocenes: **(1)** as catalyst in polymerization of alkenes yields highly isotactic polymers; the CVD of xylene with **(2)** gives carbon nanotubes; **(3)** has excellent second harmonic generation efficiency; **(4)** is a film-forming thermoplastic polymer; **(5)** exhibits antitumor activity; **(6)** is used in nickel catalyzed asymmetric cross-coupling reaction [54, 68].

A crucial aspect in many of the above applications is the stability of the metal–Cp bond, an important factor of which is the bond energy. However, detailed thermochemistry and bond energy data is scarce even for the simplest 3*d* metallocene compounds

and their ions. Only for manganocene are reliable data available; these stem from a TPEPICO measurement done earlier in our group [70]. In contrast, literature data for the derivatives of the neighbouring elements show considerable uncertainties, often due to the completely missing treatment of the kinetic shift (see Table 1.2).

Table 1.2: Metallocene fragment appearance energies and bond dissociation energies from the literature (*BDE* = bond dissociation energy). See text for details.

Metal	Treatment of kinetic shift	CpM^+ *AE* (eV)	$[CpM–Cp]^+$ *BDE* (eV)	Ref.
Cr	none	12.81 ± 0.10	6.55 ± 0.15[a]	[71]
Co	none	14.00 ± 0.10	7.79 ± 0.15[a]	[71]
Co	none	12.3 ± 1.0	6.3 ± 1.0[a]	[72]
Co	none	13.2 ± 0.2	—[b]	[73]
Co	none	14.0 ± 0.3	—[b]	[74]
Co	$\log I$ extrapol.	10.21 ± 0.30	4.86 ± 0.50[a]	[75]
Ni	none	12.59 ± 0.1	5.43 ± 0.15[a]	[71]
Ni	none	11.9 ± 1.0	5.2 ± 1.0[a]	[72]
Ni	none	12.4 ± 0.3	—[b]	[76]
Ni	none	12.6 ± 0.2	—[b]	[74]
Ni	none	13.00 ± 0.25	> 6.0	[77]
Ni	2-point RRKM	—[c]	3.24 ± 0.07	[78]

[a] Calculated as difference in *AE*s.
[b] Not given.
[c] Not determined.

So far, only one paper has been published on the investigation of chromocene by EI mass spectrometry, written by Müller et al. [71]. In that study, the authors determined the $[CpCr–Cp]^+$ bond dissociation energy as the difference of the appearance energies measured for Cp_2Cr^+ and $CpCr^+$ using the method published by Warren earlier [79], arriving at a value of (6.55 ± 0.15) eV. In the same work, $[CpM–Cp]^+$ bond energies of (7.79 ± 0.15) eV and (5.43 ± 0.15) eV were obtained for M = Co and Ni, respectively. In addition, several other fragmentation channels have been observed for each metallocene ion, but their intensities were too low for quantitative analysis. There are three other early works on the electron ionization mass spectrometry of cobaltocene, publishing $CpCo^+$ *AE*s of (12.3 ± 1.0) eV [72], (13.2 ± 0.2) eV [73] and (14.0 ± 0.3) eV [74]. However, as indicated previously, the values coming from EI mass spectrometric measurements might have significant errors because of the low energy resolution of EI experiments, unfavorable threshold laws, and neglect of the kinetic shift and that of the thermal energy distribution.

In a more recent electron ionization study [75], considerable efforts were made to take the kinetic shift into account. The dissociation onsets were measured by monitoring the fragment ions generated from metastable parent ions, and the thresholds were calculated by extrapolation of the line of log(ion intensity) vs. electron energy to a vanishing ion intensity, which gave a $CpCo^+$ appearance energy of (10.21 ± 0.30) eV and a $[CpCo–Cp]^+$ dissociation energy of (4.86 ± 0.50) eV.

For $CpNi^+$ appearance energies, several data can be found in the literature, again from electron ionization investigations. Pignataro et al. reported a value of (11.9 ± 1.0) eV [72], while (12.4 ± 0.3) eV [76] and (12.6 ± 0.2) eV [74] were published by Schissel et al. and Begun et al., respectively. The highest number, (13.00 ± 0.25) eV, comes from Flesch's group [77], in addition, they predict that the $[CpNi–Cp]^+$ bond dissociation energy is larger than 6.0 eV. Other researchers performed time-resolved photodissociation rate measurements on nickelocene cation at two different UV wavelengths in an ion cyclotron mass spectrometer [78]. Rice–Ramsperger–Kassel–Marcus (RRKM) theory was used to extrapolate the two rate constants to zero internal energy and the reported bond energy was (3.24 ± 0.07) eV.

In our group, besides the carbonyls, several transition-metal π complexes were succesfully investigated by TPEPICO (Cp_2Mn [70], $(C_6H_6)_2Cr$ [80]). These measurements provided accurate bond dissociation energies in the ionic species, with the kinetic shift and thermal energy distribution adequately taken into account.

Our aims in this thesis were to continue the TPEPICO investigation of Cp_2M^+ systems, in order to reveal the mechanism, energetics and kinetics of the ionic dissociation processes of chromocene (Cp_2Cr), cobaltocene (Cp_2Co) and nickelocene (Cp_2Ni), and to determine the $[CpM–Cp]^+$ (M = Cr, Co, Ni) bond energies.

1.3 Copper–Pyridine Complexes

Transition metals usually form compounds in several oxidation states. The stability of the various states is essentially influenced by the ligand environment, and vice versa, the preferred structure of the coordination sphere strongly depends on the oxidation state of the metal center. Metal–ligand interactions are therefore key factors in redox reactivity.

The situation is complicated even further by the fact that the presence of huge number of solvent molecules in the condensed phase can sometimes hide the inherent preference of the metal ions toward some coordination sphere structures. Gas-phase studies of complexation and solvation can therefore provide valuable complementary information for the understanding of the behavior of metal ions [81–83].

Copper, the first element in group 11 of the periodic table, provides a nice example for the interplay of coordination and redox state stability. For the closed-shell Cu^I ion in solution, the usual stereochemistry is tetrahedral, although lower coordination numbers are found occasionally, such as 2 in linear $[CuCl_2]^-$ [3]. In gas phase, the situation is reversed, and the ion shows preference for the coordination of two ligands, with occasional occurrence of tricoordinated trigonal planar as well as tetracoordinated

tetrahedral structures [84, 85]. Gas-phase studies of Cu^{I} ions solvated by water or ammonia confirmed the strong tendency of Cu^{I} to adopt the twofold linear coordination, showing subsequent solvent molecules binding to the first solvation shell instead of directly to the metal (Figure 1.7/1) [86, 87].

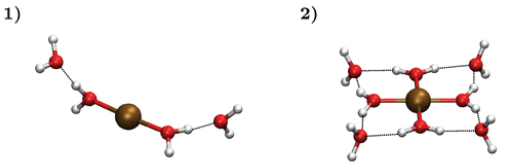

Figure 1.7: Structures of $[Cu(H_2O)_4]^+$ (**1**) and $[Cu(H_2O)_8]^{2+}$ (**2**) complexes in the gas phase [86, 88, 89]

In marked contrast to the Cu^{I} species, Cu^{II} prefers higher coordination numbers (four to six) in the gas phase, as well as in solution [85, 90–92]. As a result of the open-shell electron configuration, Cu^{II} complexes often exhibit strong Jahn–Teller effect resulting in square planar tetracoordinated and tetragonally distorted octahedral geometries [3, 93, 94]. The distinction between the different coordinations in not easy: the Cu^{II} hydrate in solution is classically described as elongated octahedron [3], but recently proposed to have fivefold coordination [91], whereas other researchers suggest a dynamical view where the different structures (including 4, 5 and 6-coordinated ones) exchange among themselves [95]. A further consequence of the Jahn–Teller distortion is the low value of the fifth and sixth stepwise stability constants and bond energies, as compared to the first four ones [3, 93].

Gas-phase measurements on multiply charged ions are less straightforward than on singly charged ones, but significant progress has been made recently [90, 93, 96]. Results indicate preference for four ligands in the case of Cu^{II}; for example, water and ammonia were found to favorably produce $[CuL_8]^{2+}$ species, where four molecules coordinate directly to the copper in a square planar manner with four additional ligands bound to the first shell via hydrogen bonds (Figure 1.7/2) [88, 89].

Higher oxidation states of copper, Cu^{III} and particularly Cu^{IV}, are generally labile, and occur only under unusual conditions [3, 97–101]; it would be thus harder to derive trends in their behavior with respect to coordination.

Copper and copper complexes have huge importance in biochemistry since a wide variety of copper-containing metalloenzymes occur in living organisms [100]. The coordination around the copper and the electronic structure of the metal in the enzymes is a field of intense interest [100, 102–104], as these determine the reactivity of the active site. Paradoxically, results of gas-phase studies may be of particular advantage here, because the coordination around a metal center might resemble the discrete molecular arrangement more than the time-averaged solution-phase picture [90]. For

example, Schröder's group have several ongoing model studies of redox-active copper species in chemical and biological processes [105–110].

Enzymes are often found to provide a mixed coordination environment for copper. Softer ligands like sulphur in cysteine or methionine, and harder ligands like nitrogen in histidine are simultaneously employed, providing stabilization for both the softer Cu^{I} and the harder Cu^{II} [100, 111]. The flexibility of the protein helps to satisfy the preference for different coordination numbers. In this way, redox-active metalloproteins may readily exist in either oxidation state (see an example on Figure 1.8).

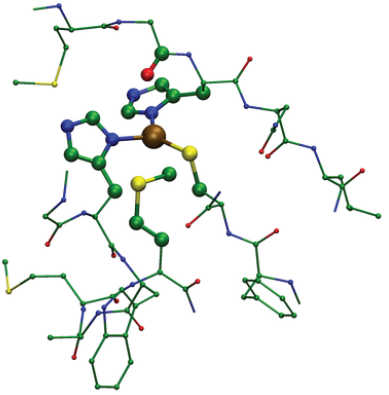

Figure 1.8: Active site of redox protein azurin II in the Cu^{I} state [112]

As a very basic model of the interaction of copper with a basic aromatic nitrogen, often encountered also in biological systems, copper complexes with the conceptually simplest *N*-heterocycle pyridine (py) may be considered. Indeed, theoretical studies of $Cu(py)_n^+$ complexes have demonstrated that pyridine serves as a σ ligand (see Figure 1.9), i.e., metal cations coordinate in plane to the lone pair of the nitrogen atom, rather than to the aromatic ring in a π-type fashion [113–115].

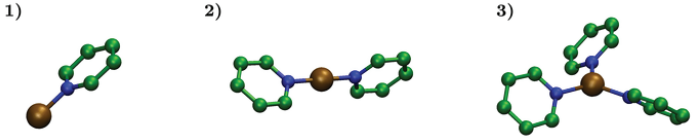

Figure 1.9: B3LYP/6-31G(d) optimized geometries of $Cu(py)_n^+$ complexes (n = 1–3) [114]

The chemistry of Cu^{I} ion with pyridine and other *N*-donor ligands in the gas phase has been investigated thorougly [113–117], and particularly the sequential bond dissociation energies $[Cu–py]^+$ = (2.72 ± 0.08) eV, $[(py)Cu–py]^+$ = (2.45 ±

0.09) eV, $[(py)_2Cu–py]^+$ = (0.85 ± 0.02) eV, and $[(py)_3Cu–py]^+$ = (0.62 ± 0.03) eV have been determined in benchmark studies of Rodgers and coworkers by guided ion beam mass spectrometry [113, 114].

Our aims in this thesis were to extend the investigations to cover the influence of such a reasonably simple σ ligand on the stability of gaseous copper(II) species and have an estimation for the related binding energies.

There are several techniques for determination of accurate bond energies between a metal cation and a ligand (e.g., the PEPICO technique [118], which was used in the first two parts of this thesis, time-resolved photodissociation mass spectrometry [119], time-resolved photoionization mass spectrometry [120] and threshold collision-induced dissociation (TCID) experiments [121]). These methods involve a detailed modeling of ion energy distribution and dissociation rate constants, and are usually available only in custom-built equipment. Instead of turning to these procedures, we have decided to try to obtain approximate fragmentation thresholds from energy-resolved collision experiments using ion-trap mass spectrometer (IT-MS). Part of our motivation was that IT-MS is one of the most widely spread and commercially available type of mass spectrometers, which is easy to operate and offers several advantageous features.

However, the analysis of the results of energy-dependent collision-induced dissociation (CID) experiments in an ion trap is not straightforward. In this respect, a key point is the conversion of the apparent thresholds to binding energies, for which, due to the complicated nature of the ion excitation process in the trap, no rigorous modeling procedure seems to be applicable. Empirical calibration is thus necessary, for which several approaches have been suggested in the literature. Energy-dependent CID in IT-MS has been carefully investigated by Brodbelt et al., who studied various effects relevant for the conversion [122–127]. Futhermore, effects of ion size as well as ion mass have been addressed [128–133]. O'Hair et al. introduced an approximate scheme for the estimation of fragmentation thresholds from energy-resolved IT-MS experiments [134–136]. Despite all of these efforts, nevertheless, the issue looks not to be settled yet.

Our further aim was therefore to study a refined approach that could enable us to estimate more accurate fragmentation thresholds using IT-MS with an appropriate calibration.

1.4 Copper–Disulfide Interaction

As discussed in detail in the previous section, copper has several stable oxidation states, which enables it to play an outstanding role as a redox catalyst. Numerous copper-catalyzed C–C coupling reactions and oxidations have been at the center of chemists' interest for the last decades. Such oxidations, coupled with molecular oxygen in aerobic media [137–141] or with peroxides in anaerobic systems [142, 143], have become cornerstones of analytical, biological, and organic chemistry. Copper catalysts have been investigated, for example, in the oxidation of alkanes to the corresponding alcohols or ketones, benzylic oxidations, or the oxidation of cycloalkanones to lactones

(copper-catalyzed Baeyer–Villiger oxidation) [137]. In addition, copper catalysis can be used even for the oxidation of aromatic C–H bonds, which is one of the most challenging problems in synthetic chemistry because of the resonance stabilization of aromatic groups [137]. While the oxidations have been generally accepted as a valuable tool, the nature of the reaction intermediates and the reaction mechanisms have, despite great efforts, often remained obscure, primarily due to the complexity of the multicomponent processes involved.

In biological systems, the side-on peroxo-bridged dinuclear Cu_2O_2 core is a common structural motif, arising from the reaction of dioxygen with the Cu_2 active site found in several copper containing metalloenzymes [100] (Figure 1.10). This fact guided the design of organic reactions where the catalytically active species involves a dicopper-dioxygen adduct; e.g., C–H activation or oxidation of alcohols to the corresponding oxo derivatives [140, 144–146]. In addition, several mass spectrometric studies showed that single transition-metal cations have a tendency to insert into the weak O–O bond of peroxides, which also represents a simple model system for catalytic oxygenation processes [147–149].

Figure 1.10: Possible reaction of Cu_2 core with dioxygen

Notably, oxygen-based electron acceptors are not the only viable substrates for copper-catalyzed oxidations. Following examples of biological chemistry, copper–disulfide interactions have enjoyed growing attention [150, 151]. Although Cu^{I}–$(SR)_x$–Cu^{I} moieties are relatively common, complexes containing thiolate bridges between two Cu^{II} centers are rare. It was only recently that the possibility of interconversion between disulfide-bridged dicopper(I) and bis(μ-thiolato)dicopper(II) complexes was demonstrated (Figure 1.11/1), which is reminiscent to the reactivity of Cu_2O_2 and proves the capability of disulfide as a copper oxidant [152, 153]. The results also demonstrated that a small perturbation in the coordination environment of the dicopper unit can trigger drastic change in the structure and in oxidation state of metal center and the binding sulfur ligand. It is worth noting that an analogous bis(μ-thiolato)diruthenium(III) complex was obtained from the reaction of disulfides with Cp*RuCl(cod), and it was proposed as a possible active species in the catalytic synthesis of vicinal dithioethers from alkenes and disulfides (Cp* = pentamethylcyclopentadienyl, cod = 1,5-cyclooctadiene) [154].

On the other hand, a CuS_2 stoichiometry, rather than Cu_2S_2, can also be imagined in copper–disulfide systems. The mechanism of several copper-catalyzed coupling reactions presumably involves Cu^{III} intermediates [144, 155–160], including the substitution reaction of alkyl halides with Gilman cuprates [155], and the copper-mediated coupling reaction of boronic acids and *N*-thioimides [160]; which points to the possibility of an

oxidative addition of disulfide forming a single copper(III) center (Figure 1.11/2). For a reaction of alkenes with disulfides resulting in the corresponding 1,2-hydroxysulfenyl derivative, a mechanism relying on cationic sulfur species attacking the electron rich substrate in an electrophilic fashion was proposed [150]. In this process, the copper(I) ion plays the role of a Lewis acid, facilitating the heterolytic cleavage of the sulfur–sulfur bond (Figure 1.11/3).

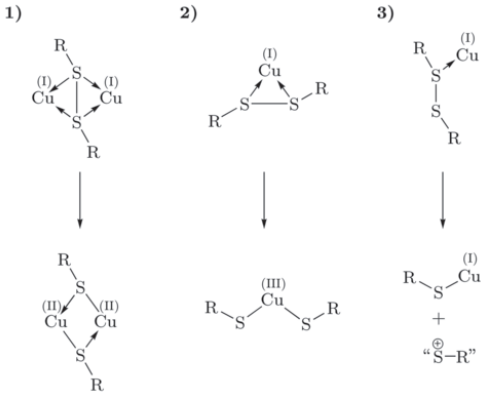

Figure 1.11: Supposed modes of interaction between copper and disulfide: **(1)** interconversion between disulfide and bis-thiolato bridge, **(2)** oxidative addition to copper, **(3)** Lewis acid catalysis of heterolytic cleavage

In order to enhance our understanding of these reactions, we decided to investigate the copper-catalyzed activation of disulfide in a simple yet synthetically interesting reaction, the intramolecular oxidation of imines by disulfides leading to the formation of benzothiazole moiety (see Figure 1.12). As proven later, this reaction opens a convenient way to prepare substituted benzothiazoles [161], which are subject of significant pharmaceutical interest [162, 163].

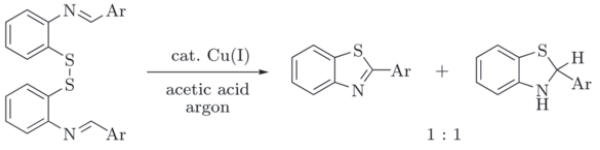

Figure 1.12: Copper-catalyzed intramolecular redox reaction between imine and disulfide functionalities (Ar = aryl). The reduced product is spontaneously oxidized to benzothiazole if exposed to air.

Our aims in this thesis were to study the copper-catalyzed intramolecular redox reaction of an imine disulfide by electrospray ionization mass spectrometry to gain some insight into the reactive intermediates and to try to distinguish between the possible scenarios of copper-disulfide interaction shown in Figure 1.11.

Chapter 2

Techniques and Theory

2.1 Experimental Methods

As it was indicated in Chapter 1, two experimental techniques (TPEPICO and ESI coupled with IT-MS) were used to obtain the results discussed in this thesis. The present section is devoted to a brief description of these methods.

2.1.1 Threshold Photoelectron Photoion Coincidence Spectroscopy

Photoelectron photoion coincidence spectroscopy (PEPICO) is a combination of photoelectron spectroscopy and photoionization mass spectrometry. The method is based on photoionization, i.e., the ejection of an electron due to the absorption of a photon:

$$\mathrm{M_{(g)}} + h\nu \longrightarrow \mathrm{M^+_{(g)}} + \mathrm{e^-_{(g)}}, \tag{2.1}$$

where M is a neutral atom or molecule, $\mathrm{M^+}$ is the resulting ion, and $\mathrm{e^-}$ is the leaving electron [118]. In the PEPICO experiment, both the photoelectrons and the corresponding molecular ions are detected in coincidence. There are two types of PEPICO: the classical PEPICO [164] uses a light source with constant wavelength and analyzes the kinetic energy of the resulting photoelectrons measured in coincidence with the ions, while in threshold photoelectron photoion coincidence spectroscopy (TPEPICO) [165–172] the photon energy is varied and only the zero kinetic energy electrons are detected. The advantage of the latter technique is that the collection efficiency of the electrons and the energy resolution are significantly higher than in classical PEPICO.

As monochromatic light is used, and the electrons (and therefore, also the ions) have zero kinetic energy, the energetics of the ionization process in TPEPICO can be written as follows:

$$E_\mathrm{i} = h\nu - IE_\mathrm{ad} + E_\mathrm{th}, \tag{2.2}$$

where E_i is the internal energy of the ion, $h\nu$ denotes the photon energy, IE_ad denotes the adiabatic ionization energy and E_th is the original thermal energy of the neutral molecule. The internal energy is distributed among the vibrational degrees of freedom of the ion, and since $h\nu$, IE_ad and E_th are known, it is well defined. If it exceeds the lowest bond dissociation energy, the ion dissociates. The parent and daughter ions are identified by their time-of-flight (TOF), which allows the kinetics of the corresponding unimolecular dissociation to be studied. The experimental results along with the precise statistical analysis of processes occuring in the TPEPICO apparatus provide accurate appearance energies of the fragment ions, from which accurate bond dissociation energies of the ionic species can be obtained.

All experimental data presented in this thesis were obtained using the custom-built TPEPICO instrument of Tomas Baer's research laboratory at the University of North Carolina at Chapel Hill [118, 173–177]. The block diagram of the apparatus is shown in Figure 2.1. Not included in the figure is the high vacuum system, which

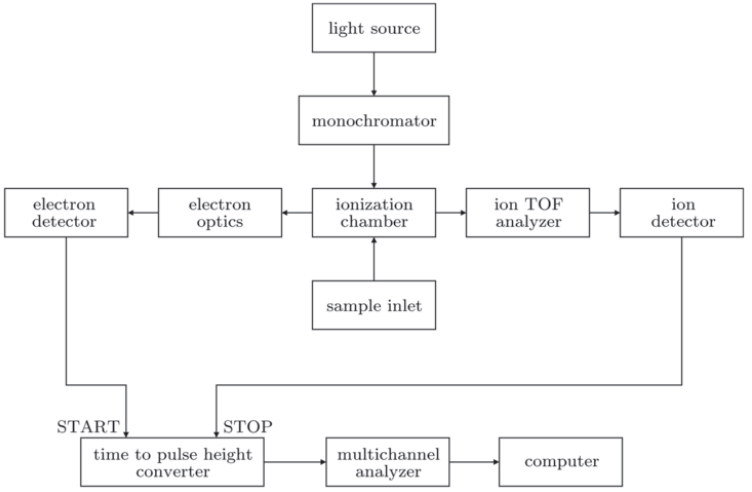

Figure 2.1: Experimental arrangement of the threshold photoelectron photoion coincidence measurements [118]

is necessary since the lifetime of photoelectrons and photoions is very small in any medium and in order to protect detectors.

In TPEPICO experiments, a hydrogen discharge lamp or synchrotron radiation are usually used as photon source [172,173,178,179]. The former has lower cost, and due to the low intensity, the ionization events occur well-separated in time; whereas the latter allows better electron energy resolution. In the TPEPICO apparatus at Chapel Hill, the sample molecules are ionized with vacuum ultraviolet (VUV) light emitted from an H_2 discharge lamp operating at approximately 1 torr H_2 pressure. The desired photon energy is selected with a 1 m normal incidence monochromator, and can be varied between 7 eV and 14.5 eV. The VUV wavelengths are calibrated against the hydrogen Lyman-α resonance line. The photon energy resolution is determined by the size of the exit slit, and in our experiments it was 1 Å in wavelength, corresponding to 8 meV at 10 eV photon energy.

The sample can be introduced into the ionization chamber in several ways. Gases and liquids that have sufficient vapor pressure can be evaporated into the vacuum chamber at room temperature through a needle, serving as a simple inlet system. For low vapor pressure liquids and solids, a temperature-controlled direct inlet system can be used. In this case, the sample is evaporated inside the chamber (in high vacuum) near the ionization region at elevated temperature. After the ionization, the ions and electrons are extracted in opposite directons with an electric field of 20 V/cm, and enter the corresponding ion and electron optics.

In the TPEPICO experiment, the electrons with zero kinetic enegy are detected, thus the electron analyzer is designed to discriminate against the energetic (hot) electrons. Conceptually, the most simple analyzer is the steradiancy analyzer [180–183], essentially consisting of a closed cylinder, with small holes in the center of the caps. The electrons with zero velocity component perpendicular to the extraction voltage go through the holes, while the analyzer rejects the electrons formed with appreciable perpendicular velocity component. A problem in such analysis, based only on angular discrimination of energetic electrons, is that besides the threshold electrons, energetic electrons with zero perpendicular velocity component are also detected. One possible solution to deal with this problem is to combine the steradiancy analyzer with a cylindrical plate analyzer [171]; here, the electrons travel along a circular arc between two curved parallel plates held at different potentials. For a certain potential difference, only electrons with a specific initial velocity can follow the curved geometry of the analyzer. If the light source is pulsed, the most effective method to get rid of the hot electron contribution is to discriminate the electrons according to their TOF.

The TPEPICO apparatus at Chapel Hill is equipped with an advanced analyzing technique called velocity map imaging [176]. This method increases both the efficiency of the detection and the energy resolution by focusing electrons onto small areas depending on their perpendicular velocity component. The focusing is almost independent from the initial position of electrons in the relatively large photoionization region.

The schematic of the electron flight tube is shown in Figure 2.2. In the usual configuration, the electrons travel ∼0.7 cm through the extracting field of 20 V/cm before they are accelerated into a 13 cm long drift region maintained at about 70 V. With this lens, electrons with zero velocity component perpendicular to the extraction field are focused to a point at the end of the flight tube, whereas electrons with nonzero perpendicular velocity component are focused onto rings around this central spot

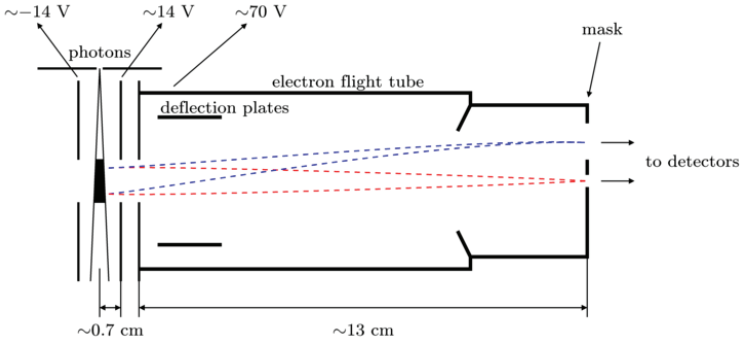

Figure 2.2: The electron velocity map imaging system [176]. The red (blue) lines indicate the path of electrons with zero (certain nonzero) perpendicular velocity component.

with radii according to their initial perpendicular velocity component. A mask is placed at the end of the electron drift tube containing a central 1.4 mm hole and a 2×8 mm rectangular opening for the hot electrons. The electrons passing through these two apertures are detected by two Channeltron electron detectors. Assuming that the signal in the off-axis detector is proportional to the hot electron contribution in the central spot, a weighted fraction of the outer ring signal can be subtracted from the central electrode signal, thereby correcting the threshold electron signal for the contribution of initially energetic electrons [184]. The factor is detemined by the ratio of center parent ion peak to the ring parent ion peak in a TOF distribution at energies well above the observed dissociation limit. At these high energies, the parent ion signal in the center TOF spectrum should be zero, and any nonzero area is due to the hot electron contamination.

Similarly to the case of the electron optics, several setups can be envisaged for the analysis of the ions. The TPEPICO at Chapel Hill can be operated using two different ion optics systems: linear time-of-flight (LinTOF) and reflecting time-of-flight analyzer (ReTOF or reflectron). In the LinTOF system (Figure 2.3), the ions are accelerated in a 20 V/cm field (same as the extraction field) over approximately 5 cm to about 100 eV. A short second acceleration region, terminated by grids, increases the ion energy to 260 eV and the resulting velocity of the ions is dependent on the square root of their mass. The ions proceed to a 26 cm long first field-free drift region at constant velocity and reach the detector. It is also possible to decelerate the ions before they enter a 8 cm long second drift region. Finally, the ions are detected with a Chevron stack of Burle multichannel plates.

If the parent ion dissociates in the acceleration region, the fragment ion has a time-of-flight falling between the parent and the daughter ion's flight time and as a result, the TOF peak of the daughter ion shows an exponential decay. The deceleration, if applied, slows down fragment ions produced in the first drift region more than parent ions and thus allows the separation of these fragment ions from their precursor ions. In that case, a Gaussian-shaped peak (the drift peak) appears at a TOF larger than the parent ion's flight time, which is due to metastable ions dissociating in the first field-free drift region. The ions that dissociate after the last acceleration/deceleration region are detected as parent ions [185–187]. The kinetic information about the dissociation is provided by the asymmetry of the TOF distribution of the metastable daughter ion, and the fractional abundances of parent and daughter ions as a function of photon energy (breakdown diagram).

In the ReTOF analyzer, the ions, after exiting the 5 cm long first acceleration region, enter the 38 cm long drift region, which ends in a 24 cm long soft reflectron where the ions are reflected by a voltage of 141 V. After traversing the second 35 cm long drift region of the ReTOF, they are detected with a multichannel plate detector. Ions that dissociate in the first drift region do not penetrate as deeply into the reflectron as the parent ions, and thus form the drift peak just after the corresponding metastable daugter ion peak, preceding the parent ion peak. The reflectron setup allows far higher mass resolution than the LinTOF analyzer, because it compensates the ion energy

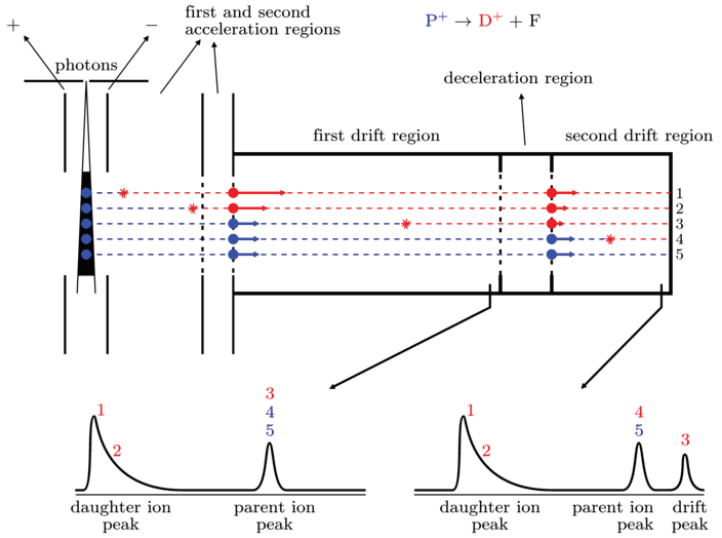

Figure 2.3: Schematic of the linear time-of-flight analyzer, with characteristic features in the TOF distributions detected without (left) and with (right) deceleration. If parent ions (P^+, blue) dissociate in the ion acceleration region, the TOF distribution of the daughter ion (D^+, red) shows an exponential decay (1 and 2). Daughter ions formed in dissociation in the drift region (3) are detected as parent ions if no deceleration is applied (left). However, if deceleration is used, these ions have larger TOF than the parent ions, and a drift peak appears as a sharp symmetric peak (right). The ions that dissociate after the deceleration region or do not dissociate at all are always detected as parent ions (4 and 5).

spread. However, its main downside is that slowly dissociating ions produced in the acceleration region or in the first drift region lose so much kinetic energy that they might be lost in the reflectron, if the mass difference between the parent and daughter ion is large. Hence, this setup is not ideally suited for investigating losses of large fragments, e.g., the cyclopentadienyl loss from metallocene ions.

In both setups, the electron and ion signal serve as start and stop signal of a time to pulse height converter for the acquisition of the ion time-of-flight spectra, and the TOF for each coincidence event is stored in an Ortec multichannel analyzer (the flight time of the electrons is negligible, as compared to the ions). Because both the center and the ring electron signals serve as start signals, two TOF distributions are obtained at each photon energy, from which a TOF distribution corrected for the hot electron contribution is calculated. Data acquisition time of a single TOF distribution ranges from 1 to 48 hours depending on the signal intensity and the desired spectrum quality.

2.1.2 Electrospray Ionization Coupled with Ion-Trap Mass Spectrometry

Mass spectrometry (MS) in general refers to a collection of experimental techniques that allow the generation of gas-phase ions, their separation according to mass-to-charge ratio, and their detection together with some form of measuring the abundance. A wide variety of approaches is available, particularly concerning the method of producing ions from the sample (the ion source), and the method of distinguishing them on the basis of m/z (mass analyzer). This flexibility renders mass spectrometry capable of answering a broad range of questions [188].

Electrospray ionization (ESI, see Figure 2.4) [188–190] is without doubt the most dominant ionization technique currently used in inorganic, organometallic and coordination chemistry. ESI was developed by Dole and coworkers [191] and was subsequently improved and succesfully coupled to a quadrupole mass analyzer by Yamashita and Fenn [192–194]. The latter was awarded a Nobel Prize in chemistry for his contribution [195]. In ESI, the sample dissolved in a moderately polar solvent is pumped through a transfer capillary into a chamber at atmospheric pressure. The capillary is held at a potential of a few kilovolts, and it is often heated. As the solution emerges from the nozzle, the electric field stretches the liquid to a Taylor cone and generates a very fine spray of highly charged droplets at the end of the cone (nebulisation). Evaporation of the solvent from the initially formed droplets by a neutral desolvation gas flow (often nitrogen) increases the charge density to the point at which the charge repulsion becomes comparable to the surface tension. There are two alternative theories explaining the subsequent production of bare sample ions [196]. The first one, called ion evaporation model [197], assumes that the ions are released from the surface of the droplets directly producing bare ions. According to the other explanation, the charged residue model [191], the increased charge density causes large droplets to divide into smaller droplets via Coulomb explosion finally resulting in droplets with one sample ion. The gas-phase ions are then formed by evaporation of the remaining solvent molecules.

ESI is a soft ionization technique, which causes little or no fragmentation of the molecules from the sample. To accomplish the transfer of the ions from the relatively high pressure of the ESI source to the low pressure of the mass analyzer, some part of the spray and the remaining solvent and desolvation gas are pumped away through a differential pumping system. The ions are guided through a little hole (a voltage called cone voltage is usually applied to extract the ions) and focused through a lensing system into the mass analyzer. ESI has several advantageous features making it attractive: it has a very low detection limit (requires low concentrations), and the soft- or hardness of the ionization process can be controlled using the cone voltage through the variation of the degree of collisional activation in the medium-pressure region [189,198]. Furthermore, since it is a solution based technique, it is extremely powerful for the direct analysis of reaction intermediates and complexes present in the solution.

The quadrupole ion trap (IT) [199,200] is a versatile mass analyzer with rapidly increasing popularity. Its invention is attributed to Wolfgang Paul [201], who was

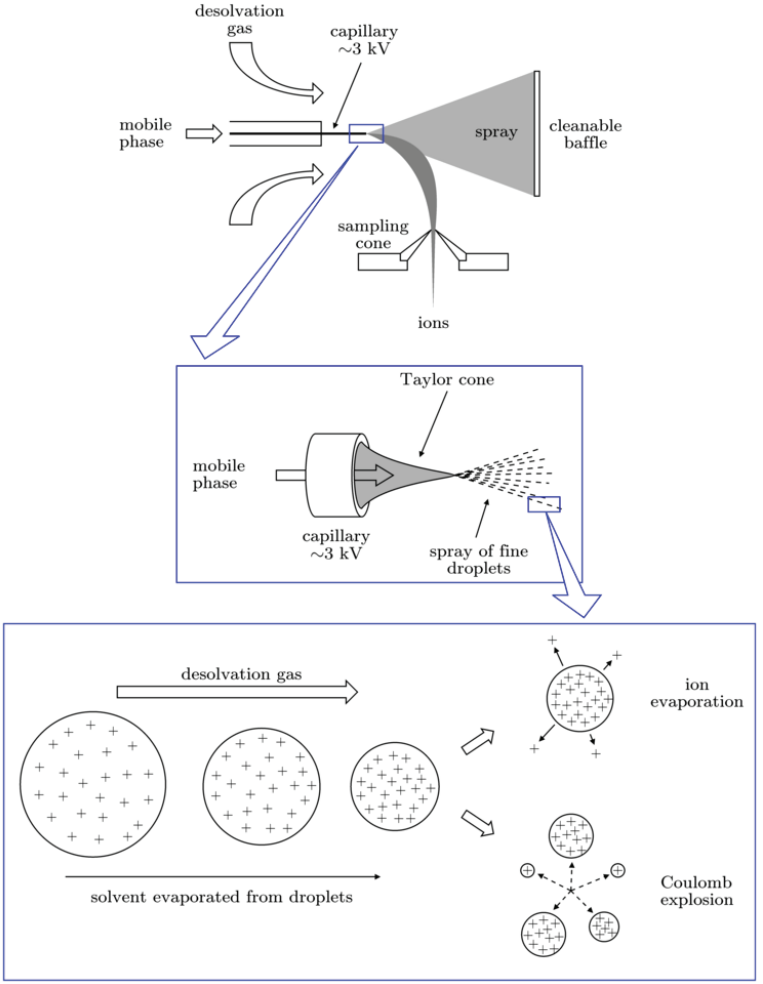

Figure 2.4: An electrospray ionization source. The solution containing the sample is pumped through a transfer capillary, and the liquid coming from the capillary forms a Taylor cone resulting in small droplets. These droplets are dried by the gas flow so that finally ion evaporation or Coulomb explosion can occur to produce gas-phase sample ions [188].

recognized by awarding the Nobel Prize in physics [195]. The quadrupole ion trap, shown in Figure 2.5, consists of three electrodes having hyperboloid geometry: two end-cap electrodes and a ring electrode located between them. Ions enter from the source through one of the end caps. By the application of an AC potential to the ring electrode, while the end-cap electrodes are on ground, an oscillating quadrupole electric field is produced, which can trap the ions for hundreds of milliseconds. Quadrupole ion traps are usually operated with the addition of a buffer gas (typically He) at a constant pressure of ca. 10^{-3} mbar. This gas cools down the ions resulting in more efficient trapping and enhancement of the equipment resolution.

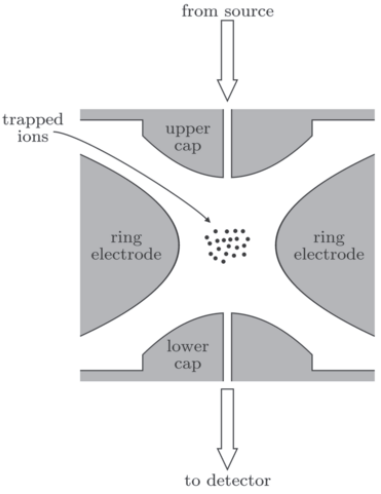

Figure 2.5: Cross-section of a quadrupole ion trap. The ions are injected through the upper cap, and stored with stable trajectories in the trap due to the oscillating quadrupole electric field produced by the ring and cap electrodes. Changing trapping field parameters or application of resonant excitation allow selective ejection of ions of a given m/z resulting in a mass spectrum [188].

The equations of motion of ions in the trap can be easily derived from Newton's law and electrostatics [200]. The properties of the ion, the trap geometry and the external potential enter these equations in a combined form, usually denoted as the a and q parameters; assuming cylindrical symmetry there is a radial and axial counterpart for both (a_r, q_r and a_z, q_z). Detailed analysis of the solutions of the equations of motion shows the ranges of these parameters that allow stable trajectories within the trap. Under the typical operating circumstances of commercial ion traps, it is sufficient to

consider the q_z parameter, which can be expressed as follows:

$$q_z = \frac{8eV}{(r_0^2 + 2z_0^2)\omega^2} \times \left(\frac{m}{z}\right)^{-1}, \tag{2.3}$$

where e is the elementary charge, V denotes the AC amplitude, ω stands for the frequency, r_0 and z_0 are the radial and axial dimensions of the trap, and m/z is the ion mass-to-charge ratio. It can be shown that ions are trapped if $q_z < 0.908$ is fulfilled; for a certain geometrical and electrical situation, this means that all ions above a certain m/z are trapped. Large-scale motion of the trapped ions can be characterized by specific secular frequencies, depending on a, q and ω, and resonant excitation of them is possible, e.g., by applying auxiliary AC fields across the end caps.

The IT can function as a mass analyzer, if the AC amplitude is gradually increased, so that trajectories of trapped ions become sequentially unstable ("mass-selective instability mode"). The ions leave the device in the order of increasing mass-to-charge ratio, and upon ejection from the trap, they reach an external detector. Mass analysis in this way takes about some tens of milliseconds and the achieved resolution is typically between 1000 and 2500. Resonant excitation can be applied to increase ion internal energy due to collisions with the buffer gas, or also to eject specific ions; the combination of the two ejection methods offer a wide range of possibilities to determine which ions remain in the trap. The advantageous properties of ITs (they are compact, cheap, robust and flexible) have made them increasingly popular in conjunction with all types of ionization methods and in combination with other mass analyzers [188, 202, 203].

Particularly in conjunction with soft ionization techniques, which produce intact molecular ions, it is desirable to have a technique for the analysis of ion fragmentation, thereby obtaining useful structural information. Collision-induced dissociation (CID) refers to a method that brings about ion fragmentation as the result of energetic collisions in the gas phase. The molecular ions are accelerated by some electric field in the mass spectrometer and collided with a neutral target gas. In the collisions, part of the translational energy of the ions is converted to internal energy, whose increase can lead to the fragmentation of the ion. Two types of CID can be distinguished: low-energy (using tens of eV) and high-energy (using thousands of eV) CID.

In the usual experiments, termed MS/MS, mass-selected precursor ions are fragmented, and the fragments are again analyzed by their mass. The cycles of such an MS/MS experiment can be separated either in space or in time. In the first case, the ions coming from the first mass analyzer are subjected to CID in a collision cell, the fragment ions are transferred to a second mass analyzer and then detected. The latter case is typical, e.g., for ITs, where the ion of interest is mass-selected by ejecting all the other ions, subsequently energized and fragmented by CID in the trap and then the fragment ions are scanned. The CID is performed by application of resonance excitation, which leads to multiple collisions of the ions with the buffer gas. Noteworthily, in ITs even more MS stages can be performed, although with decreasing intensity. In low enegy CID, the target gas is usually a noble gas, since a chemically

inert gas is required, and being monatomic they are more effective in transferring a large proportion of the kinetic energy to ion internal energy.

If the aim is to determine accurate bond dissociation energies, low energy CID measurements using guided ion beam mass spectrometers can be carried out along with analysis of the energetics of the ions and dissociation processes [121]. However, this technique is only available on custom-built instruments and cannot be implemented on commercial devices, which means a major limitation. On the other hand, CID experiments are easy to perform in IT-MS, but the conversion of the experimental data into absolute binding energies is not straightforward because of the complexity of processes in ITs [202, 203]. Instead of a detailed modeling protocol, empirical procedures can still be used for the quantitative analysis.

The primary data coming from the experiments are the fractional abundances of parent and fragment ions as the function of the relative collision energy (breakdown curves). In any analysis procedure, the conversion to absolute ion internal energies, as well as the determination of the thresholds from the breakdown curves are necessary. For the former, we empirically calibrated the energy scale using well-defined thermochemical data from the literature obtained under single-collision conditions. For the determination of thresholds, we apply a simple method previously derived for CID experiments in multipole mass spectrometers, which has been successfully used for the determination of *AE*s for a variety of gaseous transition-metal ions or their complexes [83, 106, 204–206]. Specifically, the breakdown curves for the fragment ions i and the parent ion P^+ were modeled by sigmoid functions using a least-squares criterion, fitting the following expressions:

$$I_i(E) = \frac{BR_i}{1 + e^{(E_{1/2,i} - E)b_i}}, \tag{2.4}$$

$$I_{P^+}(E) = 1 - \sum_i \frac{BR_i}{1 + e^{(E_{1/2,i} - E)b_i}}. \tag{2.5}$$

Here, BR_i stands for the branching ratio of a particular product ion ($\sum_i BR_i = 1$), $E_{1/2}$ is the energy at which the sigmoid function reaches half of its maximum value, E is the collision energy and b describes the "steepness" of the sigmoid curve and thus the observed energy dependence. The phenomenological appearance energies are then derived from linear extrapolation of the slope of the sigmoid curves at $E_{1/2}$ to the base line. This is a conceptual development over choosing the energy value corresponding to a certain fixed amount of parent ion dissociation (e.g., 5, 10 or 50 %), which has been used extensively in the literature in conjunction with CID in ITs [122, 127, 131, 134, 135].

Our experiments were performed with a Finnigan LCQ ion-trap mass spectrometer as described in the literature [207] and the main parameter settings are summarized in Table 2.1. Note that the software of Finnigan ion traps uses normalized collision energy [208], which is given as a percentage of a standard excitation amplitude. This value takes into account the mass of the parent ion with the aim to achieve a similar amount of excitation for ions with different masses, and thus further mass corrections were not carried out.

Table 2.1: Main parameter settings of the ESI-IT-MS measurements

Parameter	Cu–pyridine	Cu–disulfide
pumping flow rate	5 μl/min	10 μl/min
capillary voltage	4.5 kV	5 kV
capillary temperature	175 °C	200 °C
nebulizer gas	nitrogen	nitrogen
trapping gas	10^{-3} mbar He	10^{-3} mbar He

2.2 TPEPICO Data Analysis

In order to determine bond dissociation energies from the direct experimental results of the TPEPICO measurements (breakdown curves and TOF distributions), a detailed modeling of the processes is carried out. In this section, we will shortly discuss why this is necessary, and then present the corresponding theories and their application to the particular case of TPEPICO experiments.

2.2.1 Measuring Unimolecular Reactions

In the TPEPICO setup, the ions undergo unimolecular reaction(s), i.e., chemical reactions involving only one species as reactant. Depending on the number of product molecules, we can distinguish isomerization (one product) or dissociation (more products). The well-known differential and integrated rate laws for the unimolecular decay describe the concentration of some reacting species A, denoted as $[A]$, over time (t):

$$-\frac{\mathrm{d}[A]}{\mathrm{d}t} = k[A], \tag{2.6}$$

$$[A] = [A]_0 \exp(-kt), \tag{2.7}$$

where k is the unimolecular rate constant and $[A]_0$ is the initial concentration of the species A. The rate constant k can be expressed as a function of the internal energy of A, when the latter is constant over the ensemble ($k(E)$, microcanonical rate constant); or of the temperature, when the system can be described by a thermal equilibrium characterized by a given temperature ($k(T)$, canonical rate constant). The connection between $k(T)$ and $k(E)$ can be written as:

$$k(T) = \int_{E_0}^{\infty} P(E,T)k(E)\,\mathrm{d}E \tag{2.8}$$

where $P(E,T)$ denotes the distribution of internal energies at T temperature. The lower limit of the integration is set to E_0, the activation energy, to emphasize that no

reaction occurs unless the internal energy exceeds this threshold value. For dissociation reactions with no reverse barriers, E_0 corresponds to the *BDE*; whereas for reactions with real barriers, E_0 is equal to the barrier height (note that in this latter case, tunnelling may render $k(E)$ nonzero even for $E < E_0$).

In the TPEPICO measurements, there is a well-defined distribution of the energy of the dissociating ions, but there is no thermal equilibrium, thus $k(E)$ must be used as the basis of the analysis. $k(E)$ decreases with decreasing energy and approaches a minimum value as E goes to E_0. In principle, E_0 could be determined by varying E and detecting the onset of the reaction. However, in practice, the "first appearance" of the products is detected at different energies. One reason is that it is not possible to directly measure rate constants below about 10^3 s^{-1}, because infrared fluorescence cools the parent ions such that decay by dissociation effectively stops [209, 210]; the time frame and sensitivity of the measurements can even set a higher minimum k value at which the product formation can be observed. The excess energy required by this limitation within a certain experiment is called kinetic shift [211, 212]. In addition, the nonzero thermal energy of the sample molecules shifts the observed appearance energy to lower values (thermal shift) [39, 211], which also has to be taken into account in order to obtain accurate energetics. In parallel dissociations, the threshold of the higher energy channel may furthermore suffer from a competitive shift resulting in an elevated *AE* [213]. Thus, careful statistical modeling of the dissociation process is essential, which includes the fitting of the measured part of $k(E)$ to a unimolecular rate theory, and the extrapolation of the $k(E)$ curve over several orders of magnitude in order to correctly determine E_0.

2.2.2 Calculating Energy Dependent Rate Constants

Rice–Ramsperger–Kassel–Marcus Theory

A key element of the TPEPICO data analysis is the calculation of the dissociation rate constant as a function of the ion internal energy. A commonly used approach for determining unimolecular rate constants is the Rice–Ramsperger–Kassel–Marcus (RRKM) theory [214–217], which is also known as quasi-equilibrium theory (QET) and was developed independently by Rosenstock [218] at the same time.

The RRKM theory has three basic assumptions [219]. The first is that the rate constant depends only on the energy and the angular momentum of the ions, and does not depend on where the energy is initially located; all reactant states are assumed to be populated uniformly so that a microcanonical ensemble is maintained throughout the dissociation. This is equivalent to the supposition that internal vibrational relaxation is very fast compared to the rate of dissociation (this also ensures the single exponential decay of the reactant).

The second requirement is that there exists a surface (critical surface or transition state, TS) in the phase space which separates the products and the reactants, and all reactive trajectories cross this surface once (and only once). Thus, we assume

that trajectories cannot recross back to the reactants. Trajectory calculations on potential energy surfaces tested the validity of this assumption. It was found, for instance, that reactive trajectories for the reaction between H and Cl_2 recross several times [220]; on the other hand, the chance for such a recrossing rapidly decreases with increasing system size [221], because the phase space volume increases away from the transition state faster in larger systems than in smaller ones. In addition, the recrossing is least likely at energies close to the dissociation threshold because the phase space is very constricted and because couplings between the reaction coordinate and modes perpendicular to it are weak. For reactions with substantial energy barriers, the critical surface is at the saddle point; whereas for systems with small or no barriers the location of the critical surface depends on the total energy.

The third assumption of the theory actually concerns the mentioned coupling of the reaction coordinate; namely, this coordinate is supposed to be separable from the rest of the degrees of freedom. This is a good approximation at the saddle point, and at low energies, where the vibrational modes can be treated as independent normal modes.

Within the framework of RRKM theory, the unimolecular rate constants can be expressed as follows [219]:

$$k(E) = \frac{\sigma N^{\ddagger}(E - E_0)}{h\rho(E)}. \tag{2.9}$$

In this equation, $\rho(E)$ is the density of states of the reacting species (e.g., dissociating ion), with the energy measured from the bottom of its own potential energy well. $N^{\ddagger}(E - E_0)$ represents the sum of states of the transition state with internal energy ranging from 0 to $E - E_0$, distributed among the nonreactive degrees of freedom. Finally, σ denotes the reaction degeneracy and h is Planck's constant.

There are several approaches to derive the above equation; a simple one neglecting rotations, based on Baer's and Hase's monography [219], is given below. Following this derivation, a unimolecular rection can be viewed as a flux in the phase space. For a molecule having n internal degrees of freedom, this phase space has $2n$ dimensions: n positions (q_i) and n momenta (p_i), completely describing the system at any instant in time. The constant energy molecules (microcanonical system) are limited to a $2n - 1$ dimensional hypersurface, whereas the critical surface with constant energy has a dimensionality of $2n - 2$. If the energy (E) of the species is greater than the activation energy (E_0), it has a chance to reach the critical surface; as described above, trajectories once having passed through the critical surface are supposed to result in products.

The assumption that the reactant states are populated statistically means that the population density over the whole accessible part of the phase space is uniform. In this case, the ratio of the number of molecules close to critical surface to the total number of molecules can be expressed as the ratio of the phase space volume at the critical surface to the total phase space volume. If we denote the separable reaction coordinate by $q^{\ddagger}$, and the associated momentum by $p^{\ddagger}$, then for the $\mathrm{d}\mathbb{N}$ number of molecules being within some $\mathrm{d}q^{\ddagger}$ coordinate range at the critical surface at $q^{\ddagger}$ and

within some $\mathrm{d}p^\ddagger$ momentum range at some specific $p^\ddagger$:

$$\frac{\mathrm{d}\mathbb{N}(q^\ddagger, p^\ddagger)}{\mathbb{N}} = \frac{\mathrm{d}q^\ddagger \mathrm{d}p^\ddagger \int\limits_{H=E-\epsilon_t-E_0} \cdots \int \mathrm{d}q_1^\ddagger \cdots \mathrm{d}q_{n-1}^\ddagger \mathrm{d}p_1^\ddagger \cdots \mathrm{d}p_{n-1}^\ddagger}{\int\limits_{H=E} \cdots \int \mathrm{d}q_1 \cdots \mathrm{d}q_n \mathrm{d}p_1 \cdots \mathrm{d}p_n}, \tag{2.10}$$

where E_0 is again the activation energy and ϵ_t is the translational energy corresponding to the momentum $p^\ddagger$ in the reaction coordinate. The contribution to the reaction rate can be obtained as a flux, by dividing $\mathrm{d}\mathbb{N}$ with the time $\mathrm{d}t$ necessary for these molecules to pass the critical surface (here we assumed that motion along the reaction coordinate is separable from the other degrees of freedom):

$$\text{rate contribution} = \text{flux} = \frac{\mathrm{d}\mathbb{N}(q^\ddagger, p^\ddagger)}{\mathrm{d}t}. \tag{2.11}$$

Now, if these $\mathrm{d}\mathbb{N}$ molecules must pass the critical surface within $\mathrm{d}t$, then $\mathrm{d}q^\ddagger$ is not arbitrary, but it is related to $\mathrm{d}t$ as $\mathrm{d}q^\ddagger/\mathrm{d}t = p^\ddagger/\mu^\ddagger$, where $\mu^\ddagger$ is the reduced mass of the two separating fragments. We can obtain the following expression:

$$\frac{\mathrm{d}\mathbb{N}(q^\ddagger, p^\ddagger)}{\mathrm{d}t} = \mathbb{N}\frac{\frac{p^\ddagger \mathrm{d}p^\ddagger}{\mu^\ddagger} \int\limits_{H=E-\epsilon_t-E_0} \cdots \int \mathrm{d}q_1^\ddagger \cdots \mathrm{d}q_{n-1}^\ddagger \mathrm{d}p_1^\ddagger \cdots \mathrm{d}p_{n-1}^\ddagger}{\int\limits_{H=E} \cdots \int \mathrm{d}q_1 \cdots \mathrm{d}q_n \mathrm{d}p_1 \cdots \mathrm{d}p_n}. \tag{2.12}$$

The energy in the reaction coordinate is $\epsilon_t = p^{\ddagger 2}/2\mu^\ddagger$ and its differential is $d\epsilon_t = p^\ddagger dp^\ddagger/\mu^\ddagger$, thus we get:

$$\frac{\mathrm{d}\mathbb{N}(q^\ddagger, p^\ddagger)}{\mathrm{d}t} = \mathbb{N}\frac{\mathrm{d}\epsilon_t \int\limits_{H=E-\epsilon_t-E_0} \cdots \int \mathrm{d}q_1^\ddagger \cdots \mathrm{d}q_{n-1}^\ddagger \mathrm{d}p_1^\ddagger \cdots \mathrm{d}p_{n-1}^\ddagger}{\int\limits_{H=E} \cdots \int \mathrm{d}q_1 \cdots \mathrm{d}q_n \mathrm{d}p_1 \cdots \mathrm{d}p_n}. \tag{2.13}$$

This equation expresses the contribution to the reaction rate as the number of molecules multiplied by the contribution to the rate constant ($\mathrm{d}k$). The denominator of the latter is the density of states for the reacting species, multiplied by the factor h^n, while the numerator is a density of states for the transition state, multiplied by h^{n-1}. The rate constant contribution can therefore be given as:

$$\mathrm{d}k = \frac{\rho^\ddagger(E - E_0 - \epsilon_t)\,\mathrm{d}\epsilon_t}{h\rho(E)}. \tag{2.14}$$

In order to get the total dissociation rate constant ($k(E)$), we have to integrate over all the possible translational energies in the transition state, from which we obtain:

$$k(E) = \frac{\int_0^{E-E_0} \rho^\ddagger(E - E_0 - \epsilon_t)\,\mathrm{d}\epsilon_t}{h\rho(E)} = \frac{N^\ddagger(E - E_0)}{h\rho(E)}, \tag{2.15}$$

where $N^{\ddagger}(E - E_0)$ is the sum of states of the transition state from 0 up to an internal energy of $E - E_0$. The reaction symmetry can be taken into account by multiplying the above equation by an integer constant (σ, reaction degeneracy).

In the rigid activated complex (RAC) RRKM model, all $n - 1$ modes of the transition state, including those which will be ultimately converted to product rotations or translations (the transitional modes) are treated as vibrations with fixed frequencies; $N^{\ddagger}(E - E_0)$ is a function of those frequencies. This is certainly appropriate for dissociation reactions with reverse barriers. For such reactions, the transition state is located at the critical point on the potential energy surface and does not change with internal energy, because energy is such a dominating factor in determining the transition state sum of states. However, for reactions with no saddle point, the transition state (which is defined by an entropic minimum) shifts closer to the reactant along the reaction coordinate as the energy E is raised. Variational transition state theory (VTST) [222–228] takes this explicitly into account by locating the transition state at the minimum in $N^{\ddagger}(E - V(q^{\ddagger}), q^{\ddagger})$ along the reaction coordinate $q^{\ddagger}$. The existence of such a minimum flux configuration is due to the interplay between the potential energy $V(q^{\ddagger})$ and vibrational frequencies. As the reaction proceeds, the available energy $E - V(q^{\ddagger})$ decreases resulting in reduced sum of states; concomitantly, the lowered transitional vibrational frequencies increase the density (and therefore, the sum) of states. Thus, in VTST, the derivative

$$\frac{\mathrm{d}N^{\ddagger}(E - V(q^{\ddagger}), q^{\ddagger})}{\mathrm{d}q^{\ddagger}} = 0 \tag{2.16}$$

is solved for $q^{\ddagger}$ and the rate is calculated with the sum of states at this particular reaction coordinate value. Although this approach has proven appropriate for reactions without reverse barrier, it employs the full potential energy surface, which is not always available in sufficient precision, and requires much more computational effort than RAC-RRKM. Additional complication may arise in some VTST formulations from the presence of two minima, rather than one, with a maximum inbetween; where the TS at larger $q^{\ddagger}$ stems from the centrifugal barrier [219]. For these reasons, this method was not used in this thesis.

Simplified Statistical Adiabatic Channel Model

As we have discussed, RAC-RRKM may not be particularly appropriate for dissociation reactions without saddle points; whereas more suitable methods like VTST and the statistical adiabatic channel model (SACM [229–233]; its detailed description is beyond the scope of this thesis) require the full potential energy surface and very high amount of computations. In this work, we therefore made use of another statistical rate theory, the simplified statistical adiabatic channel model (SSACM) [219, 234, 235], which is based on phase space theory (PST) [219, 236, 237]. PST is limited to reactions with no reverse barrier and assumes that the decomposition of a molecule is governed by the phase space available to each product under the conservation of energy and

angular momentum. It locates the transition state at either infinity along the reaction coordinate $q^{\ddagger}$, or at the centrifugal barrier. The essential difference with respect to RAC-RRKM is that the transition state is assumed to be product-like, consisting of the product vibrations plus the transitional modes that have become product translations–rotations. Hence, the PST rate constant is calculated from the parameters of the products rather than from an assumed fixed transition state. This treatment is appropriate for reactions where the interaction potential between the products is isotropic at large distances and thus the reaction potential energy surface has no importance in determining the unimolecular rate constant. Unfortunately, PST tends to overestimate the rates and has limited applicability except very near the reaction threshold, but provides an upper limit to the rates.

The overestimation of $k(E)$ in PST can be attributed to the anisotropy of the potential energy surface at finite reaction coordinate values, which lends some "rigidity" to the transition state, as compared to freely translating and rotating products assumed by the theory. The SSACM rate constant takes this anisotropy into account by multiplying the transitional rotational number of states by an energy-dependent rigidity factor. It was shown that by the application of an appropriate rigidity factor, SSACM reproduces well the results of SACM rate theory at low to intermediate internal energies, but only requires similar computational efforts as RAC-RRKM [234, 235].

The functional form of the rigidity factor depends on the type of dissociation; Troe et al. developed useful expressions working well for different cases [234, 235]. For the loss of a polarizable neutral fragment with no dipole moment, where the dissociation is dominated by valence forces at short range and by relatively weak ion–induced dipole forces at long range, a useful form of the factor is given by:

$$f_{\text{rigid}}(E) = \exp\left(-\frac{E - E_0}{c}\right), \tag{2.17}$$

where c is an adjustable parameter, which indicates the relative contribution of the isotropic long-range part of the potential in comparison to the anisotropic short-range part. For the loss of a permanent dipole, when even the long-range part of the potential is markedly anisotropic, a good approximation of the rigidity factor is the following:

$$f_{\text{rigid}}(E) = \left(1 + \left(\frac{E - E_0}{c}\right)^2\right)^{-2/3}. \tag{2.18}$$

Thus, if we choose one of these rigidity factors, SSACM contains two adjustable parameters, E_0 and c. It is worth to note that although SSACM provides good rates at moderate internal energies, thus working well for rates measured by typical PEPICO experiments, it may not perform acceptably at high energies.

2.2.3 Modeling Breakdown Curves and TOF Distributions

The TPEPICO experiments provide TOF distributions, from which breakdown curves can be constructed. The direct kinetic information provided by the former, and the fractional abundances given by the latter were used together in the data analysis. The modeling process in order to obtain accurate *BDE*s is shown in Figure 2.6.

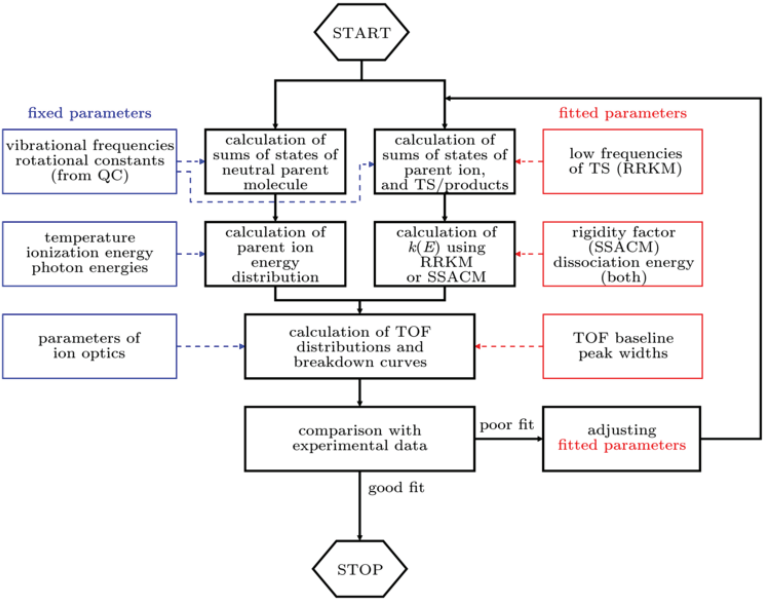

Figure 2.6: Block diagram of the TPEPICO modeling process

The first step of the analysis is the calculation of the density of states and sum of states of the molecular ions (necessary for both rate theories), transition states (for RRKM) and products (for SSACM). The same calculations are also carried out for the neutral precursor molecules, so that the thermal energy distribution of the sample can be taken into account appropriately. Assuming that the degrees of freedom of the system are not coupled, the overall density of states can be obtained by the convolution of the density of states of the separate degrees of freedom, e.g., for two variables:

$$\rho(E) = \int_0^E \rho_1(E')\rho_2(E - E')\,\mathrm{d}E'. \tag{2.19}$$

We can also obtain the overall sum of states, if we compute the convolution of the sum of states for one degree of freedom with the densities of states for the others [219].

Concerning the overall rotational degrees of freedom, the semiclassical rotational density and sum of states of free rotors can be readily calculated and expressed in analytical forms for the different types of species [219]. In our treatment the asymmetric top is approximated as symmetric top, in which two of the rotational constants are replaced by their geometric average [238].

Among the internal degrees of freedom, there may also be some that are better treated as hindered rotor than a vibration. The hindered rotor is a hybrid between a free rotor and a vibration, for which the potential can be given as:

$$V(\theta) = \frac{1}{2} V_0 (1 - \cos n\theta), \tag{2.20}$$

in which θ is the rotation angle, V_0 is the barrier height and n denotes the symmetry number of the rotor [219]. Pitzer has constructed a hindered rotor model [239] in which the energy levels well above the barrier are those of a free rotor but with an energy that is shifted by $V_0/2$. Consequently, at high energy the density of states of the hindered rotor is approximated by that of a free rotor with $E - V_0/2$ energy, while at low energy it is regarded as a harmonic oscillator. In both of the TPEPICO projects of the present thesis, the lowest frequency mode, namely, the cyclopentadienyl ring rotation, was treated using this model [38, 39, 70].

For the remaining internal degrees of freedom, uncoupled harmonic oscillators are assumed, for which the density of states can be determined using the Beyer–Swinehart direct count method [240]. This algorithm works with discrete arrays representing densities, dividing the energy scale into bins. It is capable of computing the convolution of some input array (sum or density of states) with the density of states for an arbitrary number of (possibly different) harmonic oscillators. The algorithm relies on the harmonic oscillators having equally spaced energy levels. The basic idea is that for the calculation of the convoluted array at some E, its values at lower E-s are used. For a single oscillator with ν frequency, the pseudocode is shown below, where the input array is $\rho_{\text{input}}[\,]$ and the result is produced in $\rho[\,]$:

$$\begin{gathered} \text{For all } E \text{ energies from } h\nu \text{ to } E_{\max} \\ \rho[E] \leftarrow \rho_{\text{input}}[E] + \rho[E - h\nu]. \end{gathered} \tag{2.21}$$

To finally obtain the desired rovibrational density or sum of states, the direct count method can be initialized by an input vector containing the rotational density or sum of states (or the convolution of overall rotations with internal hindered rotations). The harmonic frequencies and rotational constants necessary for the above calculations are obtained from quantum chemical calculations (see next section). From the densities of states the energy dependent rate constant can then be calculated by the use of either RAC-RRKM or SSACM theory as described previously.

The internal energy distribution of the molecular ion produced in the TPEPICO experiments is much wider than the energy resolution of the instrumentation (about 10 meV). Thus, it is necessary to interpret the measured decay rates in terms of a distribution of $k(E)$. The thermal energy distribution of the neutral sample molecules at the

temperature of the experiment can be calculated by the use of the Boltzmann formula:

$$P(E) = \frac{\rho(E)\exp(-E/k_{\mathrm{B}}T)}{\displaystyle\int_0^{\infty}\rho(E')\exp(-E'/k_{\mathrm{B}}T)\,\mathrm{d}E'}, \tag{2.22}$$

where $P(E)$ stands for the energy distribution, $\rho(E)$ is the rovibrational density of states, k_{B} is the Boltzmann constant and T denotes the temperature of the experiment. It is assumed that the neutral energy distribution is transposed directly to the ion manifold, thus the energy distribution of the parent ion at a specific photon energy $h\nu$, denoted as $P_{\mathrm{P}^+}(E, h\nu)$, is obtained as the energy distribution of the neutral molecule shifted by the photon energy minus the adiabatic IE, and then convoluted with the energy resolution function of the instrument.

For consecutive dissociation reactions, the product energy distribution for the daughter ion and the leaving neutral fragment needs to be taken into account to describe the second step appropriately [41]. After the parent ions of a particular internal energy, E, dissociate, they leave behind daughter ions in a distribution of internal energies $P_{\mathrm{D}^+}(E_{\mathrm{D}^+}, E)$, with E_{D^+} ranging from 0 to $E - E_0$, where E_0 is the dissociation energy. 0 means that all the excess energy was taken away by the leaving neutral fragment, $E - E_0$ corresponds to the case when all the energy remains in the fragment ion. The probability that E_{D^+} energy remains with the daughter ion can be derived statistically by the following equation:

$$P_{\mathrm{D}^+}(E_{\mathrm{D}^+}, E) = \frac{\rho_{\mathrm{D}^+}(E_{\mathrm{D}^+})\displaystyle\int_{x=0}^{E-E_0-E_{\mathrm{D}^+}}\rho_{\mathrm{F}}(x)\rho_{\mathrm{tr}}(E-E_0-E_{\mathrm{D}^+}-x)\,\mathrm{d}x}{\displaystyle\int_{y=0}^{E-E_0}\rho_{\mathrm{D}^+}(y)\int_{x=0}^{E-E_0-y}\rho_{\mathrm{F}}(x)\rho_{\mathrm{tr}}(E-E_0-y-x)\,\mathrm{d}x\mathrm{d}y}, \tag{2.23}$$

where ρ_{D^+} and ρ_{F} are the densities of states of the daughter ion and the neutral fragment, respectively, and ρ_{tr} is the translational density of states.

One of the experimental results to be modeled is the fractional abundance of the parent and the daughter ions, i.e., the breakdown diagrams. In case of fast dissociation reaction, all ions that have more energy than the dissociation energy will dissociate producing daughter ions. Therefore, the fractional abundance of the parent ion at a certain photon energy ($I_{P+}(h\nu)$) can be simply given as:

$$I_{\mathrm{P}^+}(h\nu) = \int_0^{E_0} P_{\mathrm{P}^+}(E, h\nu)\,\mathrm{d}E, \tag{2.24}$$

where $P_{\mathrm{P}^+}(E, h\nu)$ denotes the parent ion energy distribution [238]. In case of slowly dissociating ions, not all ions above the dissociation limit will fragment within the timescale of the experiments. Therefore, $I_{\mathrm{P}^+}(h\nu)$ contains an additional term describing the ions that do not dissociate within the time required to allow their detection as fragment ions:

$$I_{\mathrm{P}^+}(h\nu) = \int_0^{E_0} P_{\mathrm{P}^+}(E, h\nu)\,\mathrm{d}E + \int_{E_0}^{+\infty} P_{\mathrm{P}^+}(E, h\nu)\exp(-k(E)\tau_{\max})\,\mathrm{d}E, \tag{2.25}$$

where $k(E)$ stands for the microcanonical rate constant as already discussed, and $\tau_{\max}$ is the maximum time within which an ion has to dissociate to be detected as fragment, which depends on the ion optics parameters (voltages, dimensions) [238]. Fractional abundances of daughter ions can be calculated along similar lines.

The direct kinetic information comes from the shape of time-of-flight distributions. Experimentally, the TOF spectrum is collected in a multichannel analyzer, in which channel i counts the ions with time-of-flight between TOF_i and TOF_{i+1}. Having the ion optics parameters at hand, it is relatively easy to determine the TOF corresponding to some dissociation time τ; this $TOF(\tau)$ function can then be inverted numerically to get the $\tau(TOF)$ correspondence. Using this latter function, we can express the daughter ion TOF peak shape, i.e., the ion abundance $F_{\mathrm{D}^+}(i, h\nu)$ detected in some analyzer channel i [238]:

$$F_{\mathrm{D}^+}(i, h\nu) = \int_{E_0}^{+\infty} P_{\mathrm{P}^+}(E, h\nu)\left[\exp\Big(-k(E)\tau(TOF_i)\Big) - \exp\Big(-k(E)\tau(TOF_{i+1})\Big)\right] \mathrm{d}E. \tag{2.26}$$

This expression in itself would give a sharp TOF distribution, therefore it is convoluted by a Gaussian function to account for any broadening process. The total parent ion intensity is given by Equation 2.25, also convoluted by a Gaussian function.

In the modeling procedure, the following parameters are to be determined: the dissociation energy (E_0) for both statistical theories, the lowest few frequencies of the TS for RRKM modeling which turn into product rotation and translation (the transitional modes, five for the loss of a nonlinear fragment, four for a linear, two for an atom), the c parameter in the SSACM modeling, and also some instrumentation parameters, e.g., TOF baselines, TOFs corresponding to channel numbers and the full width at half maximum (FWHM) values of the convoluting Gaussian functions. Note that in the actual calculations, an energy scale referenced to the ground state of the neutral parent molecule is used, which means that the primary fitted parameter is the sum of the adiabatic IE and the bond dissociation energy, which we term as 0 K appearance energy (AE_0). This choice is particularly appropriate, as it was found that the error of the IE_{ad} affects the fitted AE_0s much less than the BDEs [70]. The AE_0 is to be distinguished from the visual appearance energy commonly referred to in experiments in the literature, as the latter also includes measurement-specific thermal and kinetic shifts.

All the above parameters are iteratively adjusted using the downhill simplex algorithm to fit the calculated breakdown curves as well as TOF distributions to the experimental ones. All the PEPICO modeling in this thesis were performed with the recently published PEPICO program [238].

2.3 Quantum Chemical Calculations

The modeling of the TPEPICO experimental data requires vibrational frequencies and rotational constants of the relevant neutral and ionic species (see the previous section); these were determined from quantum chemical calculations. Moreover, the calculations were used to predict 0 K bond dissociation energies for comparison with the experimentally determined ones in both the metallocene and copper–pyridine projects.

In this thesis, all the calculations were carried out using Kohn–Sham density functional theory (KS-DFT). In KS-DFT, the problem of interacting electrons in a static external potential is transferred to the problem of a hypothetical system of noninteracting electrons having the same electron density and moving in an effective one-electron potential. This effective potential includes the interactions with the external field (nuclei), the averaged Coulomb interaction, as well as the exchange and correlation potential, originating from the corresponding energy functionals of the density. KS-DFT is in principle an exact theory, however, the exact form of the exchange–correlation functional is unknown; therefore, approximations have to be used. Several exchange–correlation functionals have been developed, differing in the form of the functional and in the number of fitted parameters (none, a few, many). The reason of the big success and popularity of KS-DFT is that, being formally an independent electron theory, it requires similar amount of computational cost as the Hartree–Fock theory, but it leads to results that are often comparable to elaborate correlated methods. In this thesis, we used the B3LYP functional [241–245], which is one of the most widely used functionals. B3LYP provides reasonable accuracy for various systems, and due to the extensive testing many of the problematic situations have been already identified [246]. In our calculations, the geometry optimizations were carried out using polarized valence triple-ζ basis sets, either 6-311G(d,p) [247–250] or TZVP [251, 252]. Final energetics was obtained in single-point calculations using 6-311++G(2df,2pd) [249, 250, 253–255] or TZVP basis sets, with correction for the basis set superposition error (BSSE) according to the counterpoise procedure [256].

Geometries of the relevant species (neutral molecules, parent ions, daughter ions) were optimized at the above DFT level. Where appropriate, several spin states have been checked and the lowest lying ones were selected. Geometry optimizations were carried out without constraints, and the harmonic frequencies were determined by diagonalizing the mass-weighted second derivative matrix of the energy with respect to nuclear coordinates. The local minima were confirmed by the absence of imaginary frequencies. The computed harmonic frequencies were used to calculate densities of states and sums of states in case of the two TPEPICO projects and to calculate zero-point vibrational energies (ZPVEs) in all cases. No frequency scaling was applied. The rotational constants necessary for the TPEPICO analysis were also determined from the computed equilibrium geometries.

The RAC-RRKM modeling also requires approximate transition state frequencies. On the basis of calculations and experimental studies on related dissociation processes [39, 70, 257, 258], both the Cp loss reactions of the Cp_2M^+ ions (M = Cr, Co, Ni) and

the CX (X = O, S, Se) loss from chalcocarbonyl complexes are expected to be direct dissociation reactions without reverse activation barrier, i.e., the transition states do not correspond to critical points on the potential energy surface. To approximate the structure and vibrational frequencies of the transition states for the RAC-RRKM calculations, the metal–ligand bond distance of the leaving groups were fixed at 5.0 Å, and the geometry was optimized with respect to the remaining coordinates [39]. Since in the RAC-RRKM model, the lowest TS frequencies were only used as starting points in the fitting procedure, their accuracy was not a concern.

The calculated *BDE*s given in the Results and Discussion Chapter refer to ZPVE corrected enthalpy differences at 0 K ($\Delta H_{0\,\mathrm{K}}$). All calculations refer to the gaseous state in that additional solvation, aggregation and other similar effects are deliberately not included. The Gaussian 03 software package [259] was used to carry out the computations. All molecular graphics were drawn using the VMD program [260].

Chapter 3

Results and Discussion

Section 3.1

Chalcocarbonyl Complexes

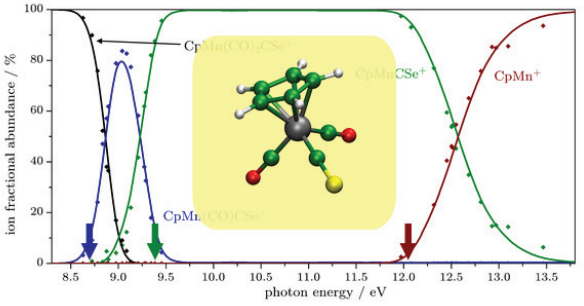

Á. Révész, C. I. Pongor, A. Bodi, B. Sztáray, T. Baer,
Organometallics, **2006**, *25*, 6061–6067

The present section is devoted to the presentation of our TPEPICO studies on chalcocharbonyl complexes aimed at the determination of metal–CS and metal–CSe binding energies. The measurements were carried out on $CpMn(CO)_2CS$ and $CpMn(CO)_2CSe$ samples. These complexes were synthesized under an inert atmosphere by the following procedure [261–266] (THF = tetrahydrofuran, C_8H_{14} = *cis*-cyclooctene):

$$CpMn(CO)_3 \xrightarrow{C_8H_{14},\ UV} CpMn(CO)_2(C_8H_{14}) + CO \tag{3.1}$$

$$CpMn(CO)_2(C_8H_{14}) \xrightarrow{CS_2,\ PPh_3} CpMn(CO)_2CS + Ph_3PS + C_8H_{14} \tag{3.2}$$

$$CpMn(CO)_3 \xrightarrow{THF,\ UV} CpMn(CO)_2(THF) + CO \tag{3.3}$$

$$CpMn(CO)_2(THF) \xrightarrow{CSe_2,\ PPh_3} CpMn(CO)_2CSe + Ph_3PSe + THF \tag{3.4}$$

The samples were purified by in-vacuo sublimation and characterized by their mass and IR spectra.

3.1.1 TOF Distributions and Breakdown Diagrams

The TPEPICO experiments were carried out with the equipment described in Section 2.1.1 (page 18). It was necessary to heat the solid samples to 50 °C ($CpMn(CO)_2CS$) and 55 °C ($CpMn(CO)_2CSe$) to obtain sufficient vapor pressure. The measurements were performed using linear time-of-flight analyzer in conjunction with subsequent deceleration with a −88 V and a −135 V voltage difference in case of $CpMn(CO)_2CS$ and $CpMn(CO)_2CSe$, respectively.

TOF mass spectra of both compounds were collected in the photon energy range of 8.3–13.5 eV. Three sequential dissociation reactions associated with the loss of CO, CO and CX (X = S, Se) are observed for both compounds:

$$\begin{aligned} &CpMn(CO)_2CX^+ \\ &\longrightarrow CpMn(CO)CX^+ + CO \\ &\longrightarrow CpMnCX^+ + 2CO \\ &\longrightarrow CpMn^+ + 2CO + CX \end{aligned} \tag{3.5}$$

Typical time-of-flight distributions with hot electrons subtracted are shown in Figure 3.1 for all three dissociation steps. The experimental data are plotted as dots, and the solid lines are the simulations that take into account the sample's thermal energy distribution and the dissociation rate constants as calculated by RAC-RRKM theory (see below). The spectra at low energies (below 8.8 eV) correspond to the loss of the first CO group. At higher energies (8.8 eV–9.7 eV), the CO loss fragment ion becomes parent ion for the next CO loss reaction. Finally, at still higher energies (above 11.7 eV), the $CpMnCX^+$ ion loses the CX ligand. In the $CpMn(CO)_2CS$ spectra, the 34.2 µs peak

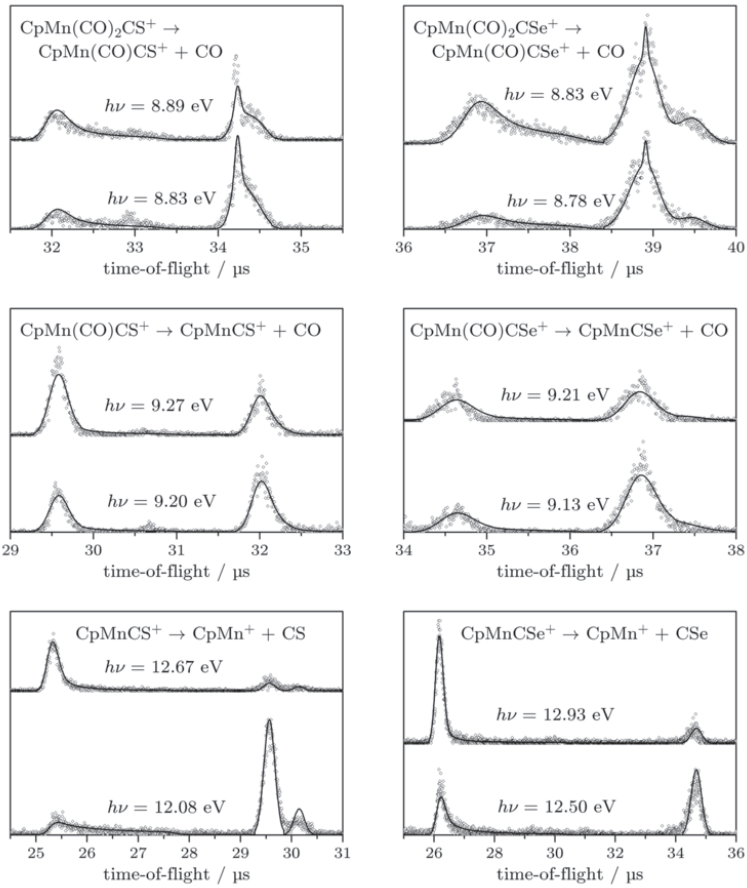

Figure 3.1: Ion time-of-flight distributions at selected photon energies, for the CS (left) and CSe (right) complexes. The points are the experimental data, the solid lines show the results of the modeling.

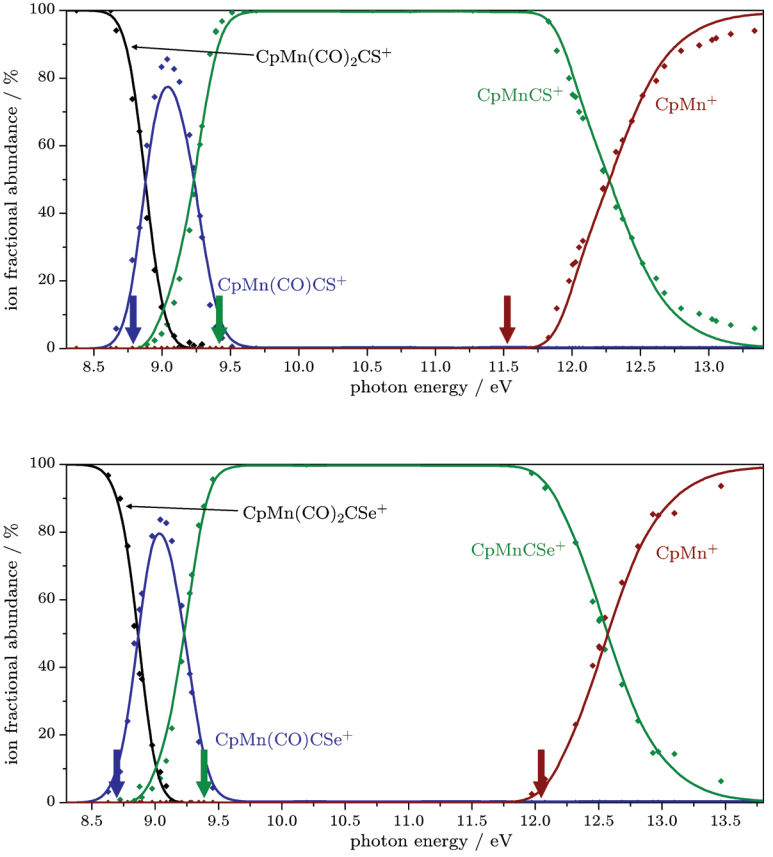

Figure 3.2: Breakdown curves of the three dissociation steps for the CS (top) and CSe (bottom) complexes. The dots are the experimental data, the solid lines are the results of the modeling; the arrows at the axis indicate the determined 0 K appearance energies.

belongs to the molecular ion, $CpMn(CO)_2CS^+$ ($m/z = 220$), and the TOF peaks at 31.7–33.2, 29.4–30.0 and 24.8–27.8 µs correspond to the daughter ions, $CpMn(CO)CS^+$ ($m/z = 192$), $CpMnCS^+$ ($m/z = 164$) and $CpMn^+$ ($m/z = 120$). The shoulder at 34.4 µs and the peak at 30.2 µs are the $CpMn(CO)CS^+$ and $CpMn^+$ drift peaks. The molecular ion and the fragment peaks of the $CpMn(CO)_3$ impurity are observed at 32.9 and 30.7 µs. In the TOF spectra of the selenium complex, the peaks can be assigned analogously. The maximum photon energy available in the instrument is about 14 eV, which is not sufficient to remove the cyclopentadienyl ligand from the $CpMn^+$ ion.

For both samples, the parent ion peak consists of two parts; a central, sharp peak on the top of a broader one. The sharp part results from the effusive jet produced by the sample inlet, while the broad feature is due to the background sample vapor. In order to account for this, we used two Gaussian functions with different FWHM values in the simulations. The product ion TOF distributions are asymmetric at energies close to the corresponding AE_0. This indicates that the ions dissociate while traveling in the first acceleration region of the ion optics. As the average lifetime of the ions is comparable to the time it takes to traverse the acceleration regions, the time-of-flight of the fragment ion is between the precursor and product ion TOF, and a quasi-exponential shape is observed in the product ion peak. As described in the previous chapter, the decay rate will be extracted from the analysis of the peak shapes.

Figure 3.2 shows the breakdown diagram of $CpMn(CO)_2CS^+$ and $CpMn(CO)_2CSe^+$, i.e., the ion fractional abundances are plotted as a function of the photon energy. In the first photodissociation reaction,

$$CpMn(CO)_2CX^+ \longrightarrow CpMn(CO)CX^+ + CO, \tag{3.6}$$

the crossover in the breakdown of the parent ion is quite steep, indicating a narrow distribution of the ion internal energy. The second and the third crossovers, corresponding to the carbonyl loss from $CpMn(CO)CX^+$ and to the thio- and seleno-carbonyl loss from $CpMnCX^+$, are increasingly wider, indicating wider distributions of the ion internal energies. Apparently, the $CpMn(CO)CS^+$ ion is stable only in a small energy range and readily dissociates to $CpMnCS^+$ + CO, which explains the weak $CpMn(CO)CS^+$ ion signal in the electron ionization experiments where the energy resolution is rather poor [27].

3.1.2 Data Analysis

Frequencies and Rotational Constants for Density of States Calculations

The analysis and modeling of the measured TOF distributions and breakdown diagrams were carried out as described in Section 2.2 (page 28). The rovibrational densities of states and numbers of states needed for the calculation of both the thermal energy distributions and rate constants were determined from quantum chemically computed rotational constants and vibrational frequencies, at the B3LYP/6-311G(d,p) DFT

level. The neutral molecules were determined to be singlet, while the lowest energy spin multiplicities $(2S+1)$ are 2, 4, and 6 for the $CpMn(CO)_nCX^+$ ions (X = S or Se; n = 2, 1, and 0, respectively). The cyclopentadienyl ring rotation was treated as a hindered rotor, for which the moment of inertia was obtained from the calculated equilibrium geometries, while for the barrier height, a value used in earlier studies on manganese complexes was employed [38, 70]. As it was mentioned previously (Section 2.3, page 38), we assume that the dissociation steps of our molecules proceed with no reverse barrier. The structure and vibrational frequencies of the transition states were approximated with those of a species having enlarged and fixed metal–carbonyl/chalcocarbonyl bond distance.

Ionization Energies

In order to carry out the modeling procedure, one also needs the adiabatic ionization energies of the complexes. These were obtained from the He I photoelectron spectra [48]. While the vertical *IE* is readily determined from the peak maximum to be (7.84 ± 0.03) and (7.86 ± 0.03) eV for the CS and CSe compounds, respectively, the adiabatic *IE* is difficult to extract from a broad band in the PE spectrum. For $CpMn(CO)_3$, the adiabatic ionization energy was determined more accurately with threshold photoelectron spectroscopy to be (7.69 ± 0.02) eV [38], and for this compound, photoelectron spectroscopy gives a vertical ionization energy of (7.94 ± 0.03) eV [48]. Assuming that the difference of the adiabatic and vertical ionization energies is the same for all three compounds, the $CpMn(CO)_3$ data can be used to estimate the adiabatic *IE*s of the CS- and CSe-substituted complexes from their vertical ionization energies. This method gives an IE_{ad} of (7.59 ± 0.04) and (7.61 ± 0.04) eV, respectively. This approximation is based on the facts that the ionization proceeds from very similar orbitals in these complexes and the vibrational structure in the three complexes is almost identical, such that the Franck–Condon factors should be similar and result in a similar vibrational envelope.

Modeling Procedure and 0 K Appearance Energies

The RAC-RRKM theory was employed to calculate the unimolecular rate constants of the various sequential dissociation reactions using Equation 2.9 (page 30). The symmetry parameter, σ, is 2, 1 and 1 in the three dissociation steps, respectively. The ion TOF distributions and the breakdown diagrams can be calculated using the thermal energy distribution of the neutral $CpMn(CO)_2CX$ molecules, the internal energy distribution and density of states of the dissociating ions, the adiabatic ionization energies, the ion optics parameters, and the transition state vibrational frequencies. The 0 K appearance energies and the lowest four TS vibrational frequencies, which turn into translation and rotation, were adjusted until the best fit to experimental data was obtained. Some of the simulated TOF distributions, and all breakdown diagrams with AE_0 values are shown above in Figures 3.1 and 3.2.

0 K appearance energies for the species $CpMn(CO)CS^+$, $CpMnCS^+$, $CpMn^+$, and $CpMn(CO)CSe^+$, $CpMnCSe^+$, $CpMn^+$ were determined in the fit to be 8.79, 9.42, 11.53, and 8.67, 9.39, 12.05 eV, respectively. All AE_0 values have an uncertainty of 0.05 eV, as discussed below. In the first approximation, each appearance energy is independent of the previous ones because we always start from the neutral parent molecule, such that the error bars do not increase with subsequent photodissociation steps.

The uncertainties for the AE_0s were determined by testing the sensitivity of the fit to the assumed vibrational frequencies by fixing the lowest four TS frequencies at various values and repeating the fitting procedure. This scheme simulates looser and tighter transition states, thereby altering the $k(E)$ rate curves. It was found that a change in the lowest four frequencies of ±50 % was necessary to worsen the quality of the fitted TOF distributions to unacceptable; however, this change did not affect the simulated breakdown diagram significantly. This is because the quasi-exponential shape of the asymmetric daughter ion distributions depends on the absolute dissociation rate, whereas the breakdown diagram depends only on the ratio of the rate constants. The optimized 0 K appearance energies change by ±0.05 eV with the altered transition state frequencies, which suggests an error bar of ±0.05 eV for these parameters.

The 0 K appearance energies for the first CO loss and the CX loss are lower than the crossover energies for both compounds, while the second 0 K appearance energy is slightly higher than its crossover energy. The ideal 0 K breakdown curve with infinitely rapid dissociation steps would exhibit sharp steps (down for the precursor ion and up to the fragment ion) at the 0 K appearance energy. As discussed in detail by Sztáray and Baer [39], the experimentally measured breakdown curve shows the effect of thermal energy distribution of the sample and the kinetic shift of the slow reaction. The thermal energy shifts the crossover energy to a lower energy, while the kinetic shift moves the crossover energy to a higher energy. The rate constant for the first CO loss increases slowly, which results in a large kinetic shift. On the other hand, the low dissociation energy for the second CO loss step results in a rapid dissociation so that the kinetic shift is negligible, and the 0 K appearance energy of the $CpMnCS^+$ ion is located somewhat to the right of the crossover energy. The loss of the final CX group is associated with a slower rate constant, and a significant amount of the energy is lost as translational and rotational energy of the two leaving CO molecules; therefore the AE_0 is again well below the crossover energy.

From the results of the fitting procedure, we can compute the activation entropies of the three consecutive dissociation reactions, which, at a temperature of 600 K, are 41.5, 63.1, 38.1 and 14.9, 40.8, 24.3 $J\,K^{-1}\,mol^{-1}$ for X = S and Se. These numbers indicate that the reactions proceed via loose transition states, as is characteristic of simple bond-breaking processes.

Determining *BDE*s

Using the AE_0s and IE_{ad}s we could obtain the bond dissociation energies:

$$BDE_1 = AE_0[\mathrm{CpMn(CO)CX^+}] - IE_{ad}[\mathrm{CpMn(CO)_2CX}] \tag{3.7}$$

$$BDE_2 = AE_0[\mathrm{CpMnCX^+}] - AE_0[\mathrm{CpMn(CO)CX^+}] \tag{3.8}$$

$$BDE_3 = AE_0[\mathrm{CpMn^+}] - AE_0[\mathrm{CpMnCX^+}] \tag{3.9}$$

From the error bars of adiabatic ionization energies and 0 K appearance energies we estimated the error limits of bond dissociation energies to be 0.06, 0.07, and 0.07 eV for BDE_1, BDE_2, and BDE_3, respectively. Therefore, the 0 K *BDE*s for the consecutive dissociation reactions are (1.20 ± 0.06), (0.63 ± 0.07), (2.12 ± 0.07) and (1.06 ± 0.06), (0.72 ± 0.07), (2.66 ± 0.07) eV for the three dissociation steps of $CpMn(CO)_2CS$ and $CpMn(CO)_2CSe$, respectively.

3.1.3 Thermochemistry

Heats of Formation

In order to convert the 0 K appearance energies into heats of formation ($\Delta_f H^\circ_{0\,K}$), we use the high-energy product ion $CpMn^+$ as an anchor for the heat of formation scale. The heat of formation of this ion was determined in a previous study on the Cp_2Mn system [70]. Thus, the 0 K appearance energy for the

$$\mathrm{CpMn(CO)_2CX} + h\nu \longrightarrow \mathrm{CpMn^+} + 2\mathrm{CO} + \mathrm{CX} \tag{3.10}$$

reaction, together with the heats of formation of the CO and CX molecules, yields the heat of formation of the $CpMn(CO)_2CX$ molecule. The heat of formation of CO is listed with great precision in all compilations; however, the same does not apply for the heat of formation of CS. Although Wagman et al. provides a value of 230 kJ mol^{-1} [267] and Chase gives (277 ± 25) kJ mol^{-1} [268], we used the value based on Okabe's measurements. The latter author determined the appearance energy of the CS A–X fluorescence [269], and obtained the bond energy in the ground state of CS_2 to be (430.6 ± 1.3) kJ mol^{-1}. This, combined with the heat of formation of $\Delta_f H^\circ_{0\,K}[CS_2]$ $= (116.9 \pm 0.8)$ kJ mol^{-1} [268] and the $\Delta_f H^\circ_{0\,K}[S] = (277.17 \pm 0.15)$ kJ mol^{-1} [270] yields $\Delta_f H^\circ_{0\,K}[CS] = (270.4 \pm 1.5)$ kJ mol^{-1} with reasonably small error bars.

Concerning the selenium analogue, Smoes and Drowart measured a C–Se bond dissociation energy of (586.6 ± 5.9) kJ mol^{-1} in CSe from equilibrium measurements using the Knudsen cell method [8]. This bond energy is confirmed by calculations of Deakyne et al. [271]. The heat of formation of the CSe molecule can thus be established with the help of the heat of formation of the Se atom, which is listed as (237.3 ± 0.6) kJ mol^{-1} by Smoes [8] and 226.4 kJ mol^{-1} by Wagman et al. [267]. The latter value, however, seems to be referring to a list prepared in 1964, so we used Smoes's more recent value. This, with the heat of formation of $\Delta_f H^\circ_{0\,K}[C] =$ (716.68 ± 0.45) kJ mol^{-1} [270], gives $\Delta_f H^\circ_{0\,K}[CSe] = (367.4 \pm 5.9)$ kJ mol^{-1}.

The molecular ions' heats of formation can also be obtained from the derived heats of formation of the neutral molecules and their adiabatic ionization energies. By combining the neutral heats of formation with the $CpMn(CO)CX^+$ 0 K appearance energies, the 0 K heats of formation of $CpMn(CO)CX^+$ can be obtained. In a similar way, the heats of formation of $CpMnCX^+$ can also be determined. The derived thermochemical data are collected in Table 3.1.

Table 3.1: 0 K and 298 K heats of formations, and thermal energies. All data are in $kJ\,mol^{-1}$.

	$\Delta_f H^\circ_{0\,K}$	$\Delta_f H^\circ_{298\,K}$	$H^\circ_{298\,K} - H^\circ_{0\,K}$
CO	-113.8 ± 0.2[a]	-110.5 ± 0.2[a]	8.7[b]
CS	270.4 ± 1.5[c]	273.6 ± 1.5[d]	8.7[b]
CSe	367.4 ± 5.9[e]	366.3 ± 5.9[d]	6.2[b]
$CpMn^+$	947 ± 16[f]	935 ± 16[f]	19.5[f]
$CpMn(CO)_3$	-408 ± 17[f]	-424 ± 17[f]	31.9[f]
$CpMn(CO)_2CS$	-123 ± 17[g]	-138 ± 17[d]	32.4[b]
$CpMn(CO)_2CSe$	-76 ± 18[g]	-92 ± 18[d]	33.0[b]
$CpMn(CO)_2CS^+$	609 ± 17[g]	596 ± 17[d]	34.1[b]
$CpMn(CO)_2CSe^+$	656 ± 18[g]	642 ± 18[d]	34.7[b]
$CpMn(CO)CS^+$	838 ± 17[g]	826 ± 17[d]	29.4[b]
$CpMn(CO)CSe^+$	875 ± 18[g]	861 ± 18[d]	29.9[b]
$CpMnCS^+$	1013 ± 17[g]	1011 ± 17[d]	24.7[b]
$CpMnCSe^+$	1058 ± 18[g]	1045 ± 18[d]	25.1[b]

[a] CODATA key values for thermodynamics [270]
[b] Determined from DFT calculated vibrational frequencies
[c] $\Delta_f H^\circ_{0\,K}[CS_2] + BDE[CS_2] - \Delta_f H^\circ_{0\,K}[S]$
[d] Computed from $\Delta_f H^\circ_{0\,K}$ and $H^\circ_{298\,K} - H^\circ_{0\,K}$
[e] $\Delta_f H^\circ_{0\,K}[C] + \Delta_f H^\circ_{0\,K}[Se] - BDE[CSe]$
[f] Li et al. [38, 70]
[g] This study

In order to convert the derived 0 K enthalpies to 298 K values, we calculated the thermal energy function, $H^\circ_{298\,K} - H^\circ_{0\,K}$, for the various species using the B3LYP/6-311G(d,p)-calculated vibrational frequencies. In the thermal contribution of the lowest frequency (Cp ring rotation), a rotational degree of freedom was used instead of a harmonic vibration. Using these data together with the $H^\circ_{298\,K} - H^\circ_{0\,K}$ values of the elements (C, 1.051 $kJ\,mol^{-1}$; H_2, 8.467 $kJ\,mol^{-1}$; Mn, 4.994 $kJ\,mol^{-1}$; O_2, 8.683 $kJ\,mol^{-1}$; S, 4.412 $kJ\,mol^{-1}$; Se, 6.199 $kJ\,mol^{-1}$ [268, 270]), we calculated the room temperature heats of formation of the $CpMn(CO)_2CX$ molecules and the ionic species; these are also listed in Table 3.1. Throughout these calculations, the

Rosenstock (ion) convention [272] was used, in which the heat of capacity of the electron was treated as 0.0 kJ mol^{-1} at all temperatures.

Chalcocarbonyl *BDE*s in All Studied Ions

Although experimentally only the Mn–CO bond breaking can be observed in the first two steps of the TPEPICO experiments, one can also get the Mn–CX bond energies in each dissociating ion. For this, the heats of formation derived above are to be combined with the heats of formation of the $CpMn(CO)_n^+$ (n = 2, 1, 0) species, determined in an earlier study [38] and later revised due to a more precise $CpMn^+$ heat of formation [70]. Figure 3.3 shows the 0 K thermochemistry of the $CpMn(CO)_2CX$ system, and the derived bond energies are listed in Table 3.2. It can be seen that in both of our compounds, the Mn–CX bond is significantly stronger than the Mn–CO bond: the Mn–CX (CX = S, Se) bond energies are larger than the Mn–CO bond energies by ∼1 and ∼1.6 eV on the average. This agrees well with the general observation that the CX ligand is more strongly bound to the metal center than the carbonyl ligand in transition-metal organometallic complexes [18, 25–27] and also with the lack of CX loss from $CpMn(CO)_2CX^+$ and $CpMn(CO)CX^+$ in our experiments.

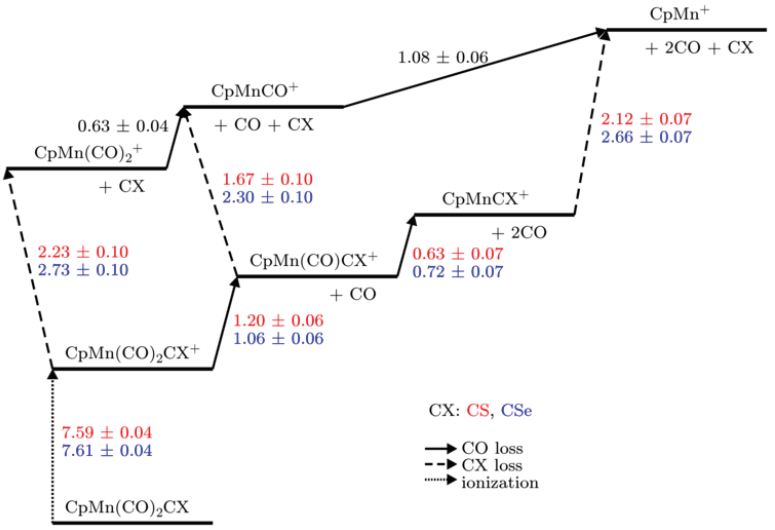

Figure 3.3: Thermochemistry of the $CpMn(CO)_2CX$ (X = S, Se) systems. Adiabatic ionization energies and bond dissociation energies are indicated in eV with their uncertainties. Values for the X = S system are in red, and listed above those for the X = Se system, shown in blue.

Table 3.2: Bond dissociation energies. Values are given in eV.

	BDE of $[L_nMn–CO]^+$	*BDE* of $[L_nMn–CX]^+$
$CpMn(CO)_3^+$	1.11 ± 0.04[a]	
$CpMn(CO)_2CS^+$	1.20 ± 0.06[b]	2.23 ± 0.10[b]
$CpMn(CO)_2CSe^+$	1.06 ± 0.06[b]	2.73 ± 0.10[b]
$CpMn(CO)_2^+$	0.63 ± 0.04[a]	
$CpMn(CO)CS^+$	0.63 ± 0.07[b]	1.67 ± 0.10[b]
$CpMn(CO)CSe^+$	0.72 ± 0.07[b]	2.30 ± 0.10[b]
$CpMnCO^+$	1.08 ± 0.06[a]	
$CpMnCS^+$		2.12 ± 0.07[b]
$CpMnCSe^+$		2.66 ± 0.07[b]

[a] Li et al. [38, 70]
[b] This study

From Table 3.2, it can also be deduced that the carbonyl replacement with chalcocarbonyls has only a slight effect on the Mn–CO bond dissociation energy, usually resulting in a weak stabilization of the Mn–CO bond. Consequently, the CO ⟷ CX change should have a minor influence on the initial CO loss step in possible catalytic cycles of $CpMn(CO)_3$, and transition-metal carbonyls in general.

Ligand Exchange Enthalpies in the Neutral Molecules

The *BDE*s in Figure 3.3 refer to the ionic species. However, bond energies in neutral species are of more interest to organometallic chemists. Although the absolute values of the neutral bond energies cannot be determined from the present work without the ionization energies of the unstable intermediate complexes, using the 0 K appearance energy of $CpMn^+$ from $CpMn(CO)_3$ determined in an earlier study [38, 70] and the appearance energy of $CpMn^+$ from $CpMn(CO)_2CX$ we can determine the reaction enthalpies for the ligand exchange reactions

$$CpMn(CO)_3 + CX \longrightarrow CpMn(CO)_2CX + CO \tag{3.11}$$

to be $\Delta_r H^\circ_{0\,K} = (-99 \pm 8)$ kJ mol^{-1} and (-149 ± 8) kJ mol^{-1} for X = S and Se, respectively. It is important to point out that, since the reaction enthalpies are determined as the difference of two 0 K appearance energies, the error bars of these enthalpies depend only on the errors of the AE_0s. The room temperature substitution heat was derived to be $\Delta_r H^\circ_{298\,K} = (-99 \pm 8)$ kJ mol^{-1} and (-145 ± 8) kJ mol^{-1} for X = S and Se, respectively (Table 3.3). The substitution heats, which in fact are the differences in the Mn–CO and Mn–CX bond energies, appear to be quite exothermic, in accordance with the fact that the CX ligands are bonded stronger to the transition-metal center than the CO ligand. To justify these quite significant stabilizations

Table 3.3: Enthalpies for the substitution reactions of $CpMn(CO)_3$ (Equation 3.11), derived from the heats of formation. Values are given in kJ mol^{-1}.

reaction	$\Delta_r H^\circ_{0\,K}$			$\Delta_r H^\circ_{298\,K}$
	B3LYP/6-311G(d,p)	G2	exp.	exp.
CO ⟷ CS	−87.5	−70.3	−99 ± 8	−99 ± 8
CO ⟷ CSe	−98.6	−94.6	−149 ± 8	−145 ± 8

found experimentally, they were compared with the results of quantum chemical calculations at the B3LYP/6-311G(d,p) and G2 levels of theory. In the former case, ZPVE corrections were done using the unscaled harmonic frequencies. As can be seen in Table 3.3, the calculated values differ significantly from the experimental values, but their order magnitude seems to support the surprisingly large bond enthalpy differences.

3.1.4 Conclusions

The TPEPICO experimental results along with the RAC-RRKM analysis of the dissociation rates provided Mn–CO bond dissociation energies in $CpMn(CO)_nCX^+$ (n = 2, 1; X = S, Se) ions and Mn–CX bond energies in $CpMnCX^+$ species. By the use of the results of previous $CpMn(CO)_3$ measurements, the Mn–CX bond energies in all $CpMn(CO)_nCX^+$ (n = 2, 1, 0; X = S, Se) complexes have been determined (Table 3.2). From the known heat of formation of the final product, $CpMn^+$, it was possible to determine the heats of formation of both the molecular ions and the various fragment ions, as well as that of the neutral sample molecules (Table 3.1). Combining the AE_0s of the present study with the AE_0s previously measured for $CpMn(CO)_3$, the enthalpies of the carbonyl replacement with CS and CSe ligands in the neutral complexes were also obtained (Table 3.3).

The results show that CS is always more strongly bound to the transition-metal center than CO, and CSe forms even stronger bonds than CS. This is in accordance with the widely accepted better σ-donor and π-acceptor properties of CX [14–17], and also with their increasing π-donor ability, which was determined in the PES study of these cyclopentadienyl manganese compounds in our laboratory [48]. On the other hand, the CX substitution hardly affects the other Mn–CO bond dissociation energies.

Section 3.2

Metallocenes

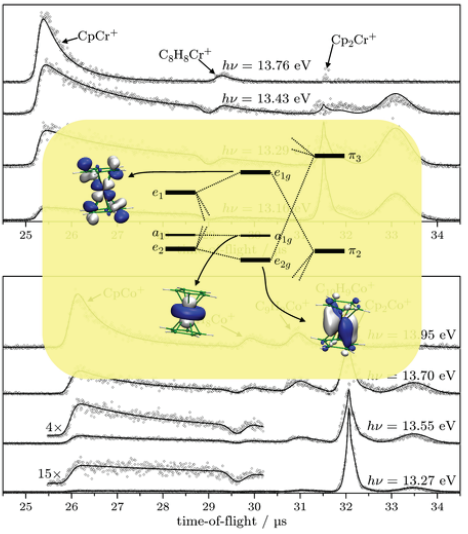

Á. Révész, L. Szepes, T. Baer, B. Sztáray,
Journal of the American Chemical Society, **2010**, *132*, 17795–17803

Following our TPEPICO work on the chalcocarbonyls, we carried out measurements using a similar procedure on chromocene, cobaltocene, and nickelocene, with the aim of determining $[M–Cp]^+$ bond dissociation energies in the cations. We took advantage of the methodological development, and carried out the analysis not only with RAC-RRKM but also with SSACM theory, which is supposed to provide better results for dissociations without reverse barrier. For the experiments, the chromocene, cobaltocene and nickelocene samples were purchased from Strem Chemicals and were used without further purification.

3.2.1 TOF Distributions and Breakdown Diagrams

All the three metallocenes were investigated with the linear time-of-flight mass analyzer of the TPEPICO apparatus (see Section 2.1.1, page 18). In order to investigate the H_2 loss from the parent ion of nickelocene (see later), this compound was also measured with a reflectron time-of-flight setup, which gives better mass resolution allowing good separation of the parent ion peak and the peak of H_2 loss. In all cases, samples were leaked into the ionization region of the TPEPICO spectrometer through the temperature-controlled direct sample inlet system. The solid sample was heated to 60 °C (Cp_2Cr), 70 °C (Cp_2Co), and 55 °C (Cp_2Ni) to obtain sufficient vapor pressure.

TOF spectra were recorded in the photon energy range of 12.2–14.0 eV for chromocene, 12.8–14.4 eV for cobaltocene, and 11.7–13.4 eV for nickelocene. Typical experimental time-of-flight distributions with the contribution of hot electrons subtracted, together with the results of modeling (see below) are shown in Figure 3.4. The major fragmentation belongs to cyclopentadienyl loss in all cases, but other minor channels appear as well. In the spectra of chromocene (Figure 3.4/1), the peak at 31.5 µs belongs to the Cp_2Cr^+ molecular ion, whereas the fragment ions appear as asymmetric peaks between 25 and 29 µs and between 29 and 31 µs. The former corresponds to $CpCr^+$, while the latter is due to C_2H_2 loss, yielding $C_8H_8Cr^+$. For cobaltocene (Figure 3.4/2), the Cp_2Co^+ peak is at 32 µs. In a minor channel, the parent ion can lose a hydrogen atom, giving a peak at 31.9 µs, which cannot be separated from the parent ion peak in the LinTOF experiment, but the TOF peak shape makes the assignment as H loss possible. The other fragment ions are $CpCo^+$ (25.5–29.5 µs), $C_8H_8Co^+$ (29.5–30.5 µs), and $C_9H_9Co^+$ (30.5–31.5 µs). In the TOF distributions of nickelocene (Figure 3.4/3), the parent ion can be found at 32.0 and 32.2 µs (nickel has two major isotopes with an abundance ratio of about 5 : 2). The two most important dissociation channels in the nickelocene PEPICO TOF spectra are the direct loss of the Cp ligand, giving $CpNi^+$ with a flight time between 25.6 and 29.6 µs, and the H_2 loss, yielding a peak at 31.9 µs, overlapping with the parent ion peak. Two further fragments can also be seen in the TOF distributions, which belong to $C_8H_8Ni^+$ and $C_9H_9Ni^+$, at flight times of 29.7–30.6 µs and 30.6–31.6 µs, respectively. As mentioned earlier, the TOF distributions of nickelocene were also recorded with the reflectron setup, in order to investigate the H_2 loss with better mass resolution. It was found that only H_2 loss takes place and there is no concomitant H

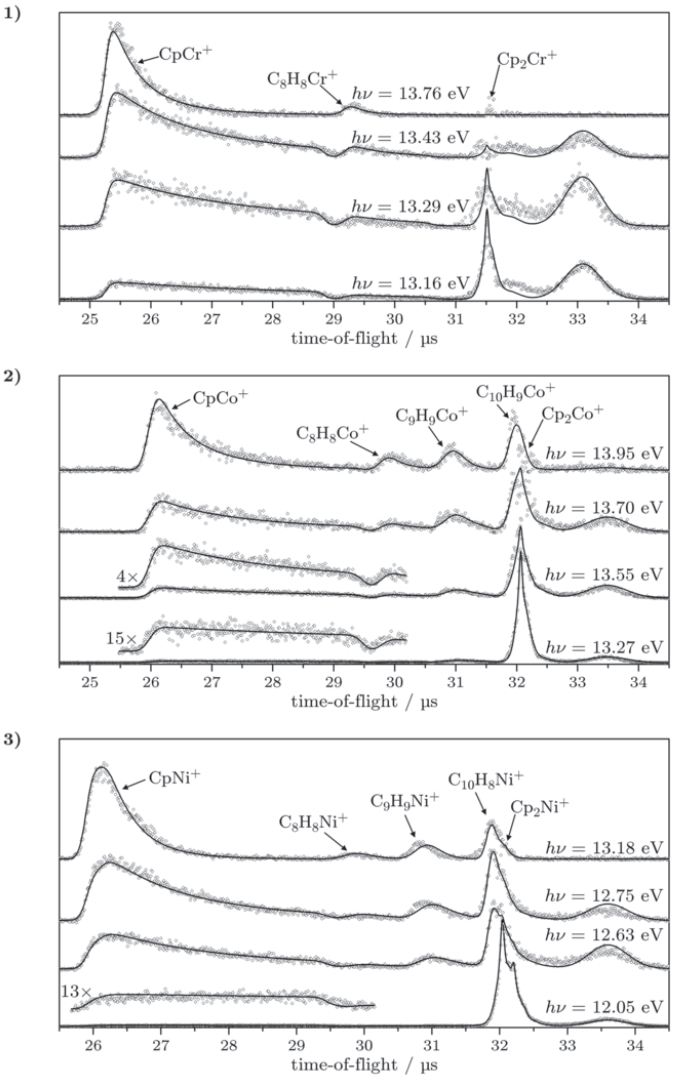

Figure 3.4: Ion time-of-flight distributions at selected photon energies for Cp_2Cr^+ (**1**), Cp_2Co^+ (**2**) and Cp_2Ni^+ (**3**) complexes. The points are the experimental data, the solid lines show the results of the SSACM modeling. Practically the same quality fit was obtained using RAC-RRKM modeling.

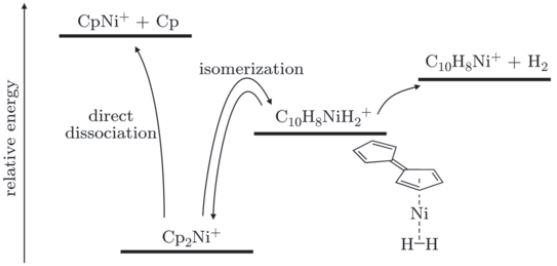

Figure 3.5: The cyclopentadienyl and H_2 loss channels of nickelocene cation

loss from the nickelocene ion. Because of the high bond energy of the H_2 molecule, it is very likely that instead of the quick sequential loss of two H atoms, the H_2 loss occurs in one step, and this dissociation channel presumably follows the isomerization of Cp_2Ni^+ into a $C_{10}H_8NiH_2^+$ ion (see Figure 3.5). In all cases, the peaks on the right-hand side of the parent ions are the drift peaks. The maximum photon energy available in the instrument is about 14 eV, which is not sufficient to remove the cyclopentadienyl ligand from any of the studied CpM^+ ions.

Some features of the observed TOF spectra are typical for such TPEPICO measurements, and are thus reminiscent to the chalcocarbonyl case. Namely, the molecular ion peaks comprise a central sharp peak on top of a broader peak (effusive jet of sample inlet and background vapor, modeled with two Gaussians); the daughter ion TOF distributions are asymmetric (dissociation in the acceleration region, producing TOFs between parent and daughter ion peak; the quasi-exponential peak shape is used to determine decay rate). Similarly to the chalcocarbonyl case, we also analyze the fractional abundances of the parent and daughter ions as a function of the photon energy, i.e., the breakdown curves; these are shown in Figure 3.6.

3.2.2 Data Analysis

Frequencies and Rotational Constants for Density of States Calculations

The analysis of the measured TOF distributions and breakdown curves were carried out using RAC-RRKM and SSACM statistical theory as described in Section 2.2 (page 28). The rotational constants and frequencies of the neutral molecules and parent ions required for both theories and energy distribution calculations were determined from quantum chemical calculations at the B3LYP/6-311G(d,p) level of theory. The spin state of the neutral molecules was determined to be the triplet for chromocene, doublet for cobaltocene, and triplet for nickelocene, while these are quartet, singlet and doublet in the corresponding ions, respectively. The lowest-energy spin multiplicities for the Cp-loss dissociation products were calculated to be quintet, quartet, and triplet for CpM^+ with M = Cr, Co, and Ni. Although the dissociation of singlet Cp_2Co^+ to

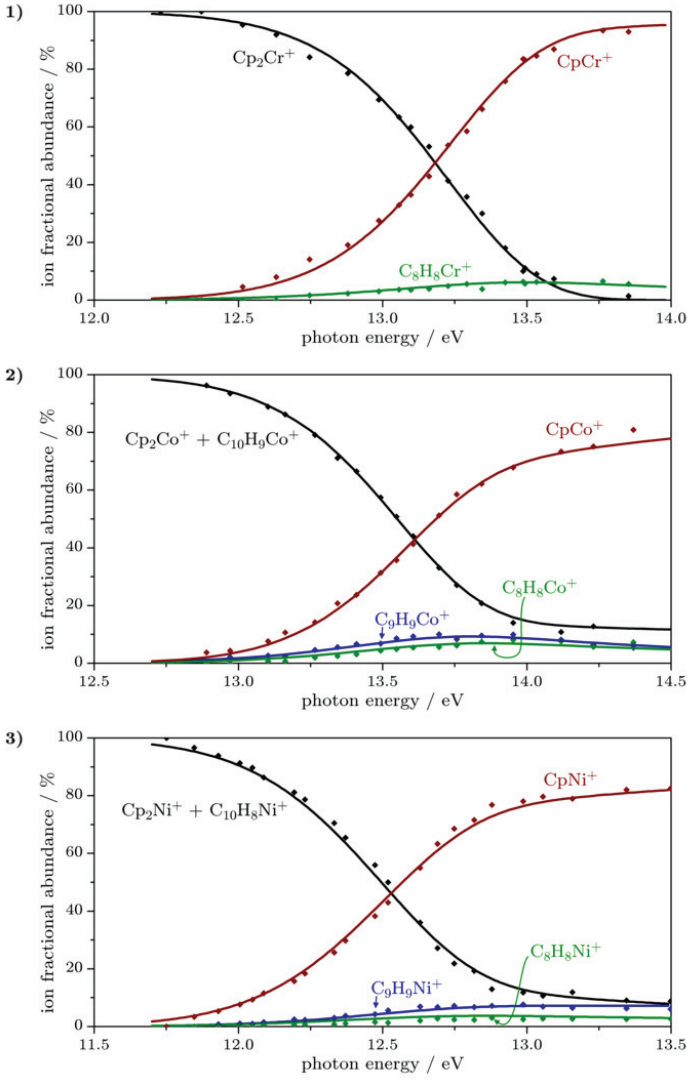

Figure 3.6: Breakdown diagrams of Cp_2Cr^+ (**1**), Cp_2Co^+ (**2**) and Cp_2Ni^+ (**3**) ions. The symbols are the experimental data, the solid lines show the results of the SSACM modeling. RAC-RRKM curves look essentially identical.

quartet $CpCo^+$ is formally spin-forbidden, TPEPICO studies on a similar $CpMn(CO)_3^+$ ion clearly showed that spin conservation laws can be violated in such dissociations [38]. For the Cp ring rotation, our DFT calculations indicate that the energy barrier is less than 5 kJ mol^{-1} for each metallocene; therefore this internal rotation was treated as a hindered (Pitzer) rotor [219, 239] in the kinetic modeling. The necessary moments of inertia were obtained from the calculated structure of the equilibrium states, while for the barrier heights, the DFT estimated values were used. Structure and frequencies were also computed for the $C_{10}H_8NiH_2^+$ species (where $C_{10}H_8$ = pentafulvalene), formed via isomerization of Cp_2Ni^+.

The Cp loss reactions of the Cp_2M^+ ions are expected to be direct dissociation reactions without reverse activation barrier [70]. In addition, we handled the other channels as direct dissociations as well, which gave a good fit for cobaltocene and nickelocene and resulted in an adequate description of the minor dissociation channel of chromocene. To approximate the structure and vibrational frequencies of the transition states for the RAC-RRKM calculations, the metal–cyclopentadienyl bond distance of the leaving cyclopentadienyl group was enlarged and fixed, and the frequencies of this species were used. In the case of the minor dissociation channels, namely, H, CH, C_2H_2, and H_2 loss, the precursor ions' frequencies were used as estimates for the frequencies of the transition states, and one frequency, which was assigned as the critical frequency for the dissociation step, was deleted. The lowest few frequencies of the transition states were subject of optimization to fit the calculated TOF distributions and breakdown diagrams to the experimental ones.

In the SSACM analysis, one needs the vibrational frequencies of the product ions and neutral fragments instead of those of the rigid transition states. Thus, calculations were carried out for the Cp, C_2H_2, CH, and H_2 neutrals and the $C_8H_8Cr^+$, $C_{10}H_9Co^+$, $C_9H_9Co^+$, $C_8H_8Co^+$, $C_9H_9Ni^+$, $C_8H_8Ni^+$, $C_{10}H_8Ni^+$, and CpM^+ (M = Cr, Co, Ni) ions. According to the lowest energy geometries in our calculations, the $C_9H_9M^+$ species contain a cyclopentadienyl and a cyclobutadienyl ligand, whereas in $C_8H_8M^+$ there is a cyclopentadienyl and an allyl group bound to the metal center (M = Co, Ni). While a C_2H_2 loss leading to this latter complex seems quite reasonable, it is hard to find a qualitative explanation for the CH loss channel, even if *cyclo*-C_4H_4 is quite stable complexed to a transition-metal center; nevertheless, its modeling as direct dissociation provided an acceptable fit. In the case of $C_8H_8Cr^+$, there are two other species besides the above-mentioned structure that are very close in energy: the first one has a cyclooctatetraene ligand, while the other one contains a dihydropentalene group. Since there is not enough experimental information to distinguish the three alternative dissociation pathways, the C_2H_2 loss was treated analogously to the Co and Ni-containing species in the data analysis. However, the existence of the other dissociation channels cannot be excluded and may warrant a variable-energy cross-beam experiment, such as the one described by Dutuit and coworkers [273], to search for isomer-specific association reactions. Again, the geometry optimizations were carried out with several spin states, and the equilibrium structures of the lowest-energy species were employed.

Ionization Energies

The adiabatic ionization energies of Cp_2M (M = Cr, Co, Ni) are also necessary for the data analysis. There are several vertical ionization energy values of metallocenes in the literature, derived from He I photoelectron spectra. Rabalais [55] determined the *IE* of Cp_2M to be 5.69 and 6.40 eV (no error bars given) for M = Cr and Ni, while values of (5.70 ± 0.1) eV (Cp_2Cr), (5.55 ± 0.1) eV (Cp_2Co), and (6.50 ± 0.1) eV (Cp_2Ni) were published by Cauletti et al. [56]. These latter values are in good agreement with Evans et al. [57], who suggested vertical ionization energies of 5.71, 5.56, and 6.51 eV (no error bars given) for the three compounds, respectively. While the vertical *IE* is readily determined from the peak maximum in the photoelectron spectrum, the adiabatic *IE* is more difficult to extract from a broad band and, accordingly, the adiabatic values of 5.50 eV (Cp_2Cr) and 6.20 eV (Cp_2Ni) by Rabalais [55], listed without confidence intervals, are of uncertain accuracy. Thus, the adiabatic ionization energies used in the modeling were calculated instead from the experimental Gibbs free energies of ionization, being 533.5 $kJ\,mol^{-1}$ [(5.529 ± 0.065) eV] for Cp_2Cr, 516.7 $kJ\,mol^{-1}$ [(5.355 ± 0.065) eV] [274] for Cp_2Co, and 601.7 $kJ\,mol^{-1}$ [(6.236 ± 0.065) eV] [275] for Cp_2Ni. These values by Ryan et al. [274,275] refer to 350 K and they were determined by Fourier transform ion cyclotron resonance mass spectrometry in which gas-phase electron transfer equilibrium reactions were investigated between the metallocenes and a variety of reference compounds whose adiabatic ionization energies are well known.

In order to convert these $\Delta G_{\text{ioniz}}(350\ \text{K})$ values to $\Delta H_{\text{ioniz}}(350\ \text{K})$, we used the calculated $\Delta S_{\text{ioniz}}(350\ \text{K})$ of -1.10, -43.03, and $-3.82\ J\,K^{-1}\,mol^{-1}$ for Cp_2Cr, Cp_2Co, and Cp_2Ni, respectively. The entropic contribution of the Cp ring rotation—essentially a free rotor in all cases—was assumed to cancel out for the Cp_2M and Cp_2M^+ complexes [275,276] and was thus neglected in calculating ΔS_{ioniz}. The multiplicities and orbital degeneracies were used to calculate the electronic entropies, assuming ground state to ground state transitions. The entropy of ionization of cobaltocene is quite different from the other two metallocenes because the cobaltocene reaches the very stable 18-electron configuration upon the ejection of an antibonding electron, which results in a significant entropy decrease, largely due to the tightening of the vibrational modes. The ionization entropies yield $T\Delta S$ terms of -0.004, -0.156, and -0.014 eV for Cp_2M where M = Cr, Co, and Ni, respectively ($T = 350\,K$). From these values, we obtained $\Delta H_{\text{ioniz}}(350\ \text{K})$ of 5.53 eV (Cp_2Cr), 5.20 eV (Cp_2Co), and 6.22 eV (Cp_2Ni). These can be converted to $\Delta H_{\text{ioniz}}(0\ \text{K}) = IE_{\text{ad}}$ by the use of calculated $H^\circ_{350\,\text{K}} - H^\circ_{0\,\text{K}}$ values, which finally yields adiabatic ionization energies of 5.53, 5.24, and 6.22 eV for our three compounds.

The error in the electron transfer equilibria were quoted as $\pm 6\ kJ\,mol^{-1}$ [274,275]; the conversion to $\Delta H_{\text{ioniz}}(0\ \text{K})$ is likely to contribute an error less than 2 $kJ\,mol^{-1}$ (0.02 eV) for the chromium and nickel complexes, whereas $\sim 5\ kJ\,mol^{-1}$ (0.05 eV) may be expected for the cobalt complex, which undergoes significant tightening upon ionization. Therefore, the adiabatic ionization energies that we used in our data analysis are (5.53 ± 0.07) eV (Cp_2Cr), (5.24 ± 0.08) eV (Cp_2Co), and (6.22 ± 0.07) eV

(Cp_2Ni). These numbers, coming from equilibrium measurements, are currently the most reliable available adiabatic ionization energies and are furthermore in very good agreement with Rabalais's adiabatic *IE*s determined from photoelectron spectra.

Modeling Procedure and Appearance Energies

As discussed in details in the theoretical chapter, the RAC-RRKM model treats the transitional modes as vibrations with fixed frequencies, which is less appropriate for reactions without a reverse barrier (like the Cp loss channels here), where the transition state shifts along the reaction coordinate with varying energy. For such reactions it was shown in the TPEPICO study on halobenzene ions [277] that, contrary to RAC-RRKM, the SSACM does not only fit the experimental rates properly but was also found to extrapolate to the known thresholds within the reported experimental errors. The large number of internal degrees of freedom in neutral metallocene molecules and the asymmetric peak shape of the CpM^+ ions in the TOF distributions over a wide energy range indicate a very significant kinetic shift for the Cp loss from Cp_2M^+, highly demanding an accurate extrapolation procedure. Therefore, in the modeling of the TPEPICO data, both RAC-RRKM and SSACM were employed, the latter to obtain accurate and reliable thermochemistry of these ions, and the former to compare the two theories as well as the results with literature data.

In analogy with the chalcocarbonyl case, the RAC-RRKM fit of the TOF distributions and breakdown diagram can be calculated from the following information: the adiabatic ionization energy; the thermal energy distribution of neutral Cp_2M molecules, which in combination with the energy resolution function of the instrument leads to the internal energy distribution of the dissociating ions; the ion optics parameters (acceleration electric fields and the acceleration and drift distances); and the reactant and transition-state densities of states. The zero-kelvin appearance energies and the lowest five TS vibrational frequencies were then adjusted until the best fit was obtained to both the TOF distributions and breakdown curves. The optimized frequencies were significantly lower than the initial estimates from the constrained DFT optimization at a fixed metal-to-Cp distance, indicating a loose transition state. The forward and backward barriers of the isomerization process of nickelocene ion and the lowest few frequencies of the isomerization transition state were obtained from analysis of the reflectron measurements and were used without refitting in the modeling of the linear TOF experiments. The following AE_0s were determined for the CpM^+ fragment ions: (10.14 ± 0.10), (10.83 ± 0.11), and (9.88 ± 0.14) eV for M = Cr, Co, and Ni, respectively.

As described previously, the uncertainties for the AE_0s were estimated by testing the sensitivity of the fit to changes in the lowest five TS frequencies, simulating looser and tighter transition states. Upon changing the frequencies by ±30% and fixing them, the quality of the fit to the TOF distributions became significantly worse, and the obtained AE_0 values were then accepted as the error bars. As before, this alteration did not affect the simulated breakdown diagram significantly, because the

latter mainly depends on the ratio of rate constants, and does not contain much information about the kinetic shifts.

In a similar way, we also carried out SSACM modeling. Dissociation rates were calculated using reactant and product densities of states, and the transitional rotational number of states was multiplied by the energy-dependent rigidity factor suggested for polarizable neutral fragments (Equation 2.17, page 33). Since SSACM is limited to reactions with no reverse activation energy, the isomerization process of nickelocene was treated with the RAC-RRKM theory. In these modeling calculations, the zero kelvin appearance energies and the SSACM rigidity factor c parameters were optimized to fit the time-of-flight distributions and breakdown curves to the experimental data. The optimized values for c were 279, 1942, and 581 cm^{-1} for the Cp loss in Cp_2Cr^+, Cp_2Co^+, and Cp_2Ni^+, respectively. As known, the role of this energy-dependent rigidity factor is to correct the PST rates to the experimentally measured values; indeed, without this SSACM correction the PST rates were 1.1–1.4 orders of magnitude higher than the SSACM rates for the nickelocene ions in the range of the experimental rate constants, if the same AE_0 was assumed. While the difference for cobaltocene was somewhat smaller, for chromocene the fastest measured rate was more than 2 orders of magnitude slower than the PST calculated one. The best fit to the TOF distributions and breakdown diagrams was obtained with the 0 K appearance energies for $CpCr^+$, $CpCo^+$, and $CpNi^+$ of (10.57 ± 0.10), (11.01 ± 0.08), and (10.18 ± 0.09) eV, respectively. The error bars of the AE_0s were obtained in this case by repeating the fitting procedure with various fixed c parameters. The simulated time-of-flight distributions and breakdown diagrams are shown as solid curves in Figures 3.4 and 3.6 above (pages 56 and 58); however, it must be noted that we could get practically the same quality of fit with RAC-RRKM modeling as well.

The agreement between the calculated and measured breakdown curves and TOF distributions is very good; even the branching ratios of the C_2H_2-loss channel from Cp_2Cr^+ could be reproduced with suitable accuracy by modeling this channel as a direct dissociation, although isomerization might play a role here. We have checked the importance of the CH and C_2H_2 losses in the modeling of the two other metallocenes; it turned out that neglect of the minor channels decreases the determined CpM^+ 0 K appearance energies by approximately 30 meV.

We furthermore computed activation entropy values, which we found to be more than 50 $J\,K^{-1}\,mol^{-1}$ at 600 K for all of the investigated metallocene ions; these large positive values indicate that the dissociation of Cp proceeds via a loose transition state, as expected for simple bond-breaking reactions.

Comparison of Rate Theories and Model Error Bars

Concerning the two rate theories, it was found that the RAC-RRKM AE_0s are systematically smaller than the SSACM values, by up to 0.4 eV in the case of $[CpCr–Cp]^+$. The considerably larger difference between RAC-RRKM and SSACM in the case of the $[CpCr–Cp]^+$ reaction compared to the halobenzene dissociation [277] can

be attributed to the much slower reaction here and thus the much larger kinetic shift. As evident in the breakdown diagram for $[CpCr–Cp]^+$ in Figure 3.6/1, the (SSACM) derived dissociation onset of 10.57 eV is about 2 eV below the phenomenological onset, which greatly increases the extrapolation error in the RAC-RRKM model [277].

For a comparison of the models, we show the RAC-RRKM and SSACM calculated rate curves for the cyclopentadienyl loss channels in Figure 3.7 along with the experimentally determined rate points. To determine these experimental points, we still need to carry out some fitting, as the width of the energy distribution of the ions at a certain photon energy is small but nonnegligible. We employed RAC-RRKM theory to fit the TOF distribution and the corresponding relative abundances at each photon energy separately. We thus obtained at each point a $k(E)$ function; and as experimental rate point we accepted the E and corresponding $k(E)$ values where $E = h\nu - IE_{ad} + E_{th}$ with E_{th} being the most probable energy in the thermal energy distribution. The error limits were established by varying the $k(E)$ function (essentially, the TS frequencies) until the fit to the TOF distribution at the given photon energy no longer seemed reasonable. From the comparison of the such derived experimental points with the modeling results in Figure 3.7 it is evident that both the RAC-RRKM and the SSACM models can fit the experimental rate constants over 3 orders of magnitude in $k(E)$, but provide notably different extrapolated values. This is the result of the large kinetic shift; in the vicinity of AE_0, the reaction is very slow (not shown); and even 3 eV above the 0 K appearance energies, the daughter ion peak shape in the TOF distributions is still asymmetric.

Although we cannot distinguish the two rate models by the goodness of the fit, we expect SSACM to be superior for barrierless dissociation reactions with a very large kinetic shift. In the only quantitative test of SSACM, the halide loss from the halobenzene ions, the derived SSACM AE_0 were correct to within the experimental uncertainty of the known thermochemistry (±20 meV). Furthermore, it was noted in that study that the accuracy of the fit is greatly improved by good rate data down to 10^3 s^{-1}, which is close to the lowest rate that can be measured without interference from IR radiative cooling [209, 210]. Even when it is considered that the kinetic shift is much larger here than in the case of the halobenzenes, the uncertainty from the SSACM modeling is not expected to be more than 0.1 eV. When this uncertainty is added to the SSACM error derived from the fitting quality, we arrive at the following recommended 0 K appearance energies: (10.57 ± 0.14) eV for $CpCr^+$, (11.01 ± 0.13) eV for $CpCo^+$, and (10.18 ± 0.13) eV for $CpNi^+$.

Determining *BDE*s and Comparison with Literature Values

From the CpM^+ AE_0 values (M = Cr, Co, Ni) and adiabatic ionization energies, we obtained the $[CpM–Cp]^+$ bond dissociation energies via

$$BDE = AE_0[CpM^+] - IE_{ad}[Cp_2M]. \tag{3.12}$$

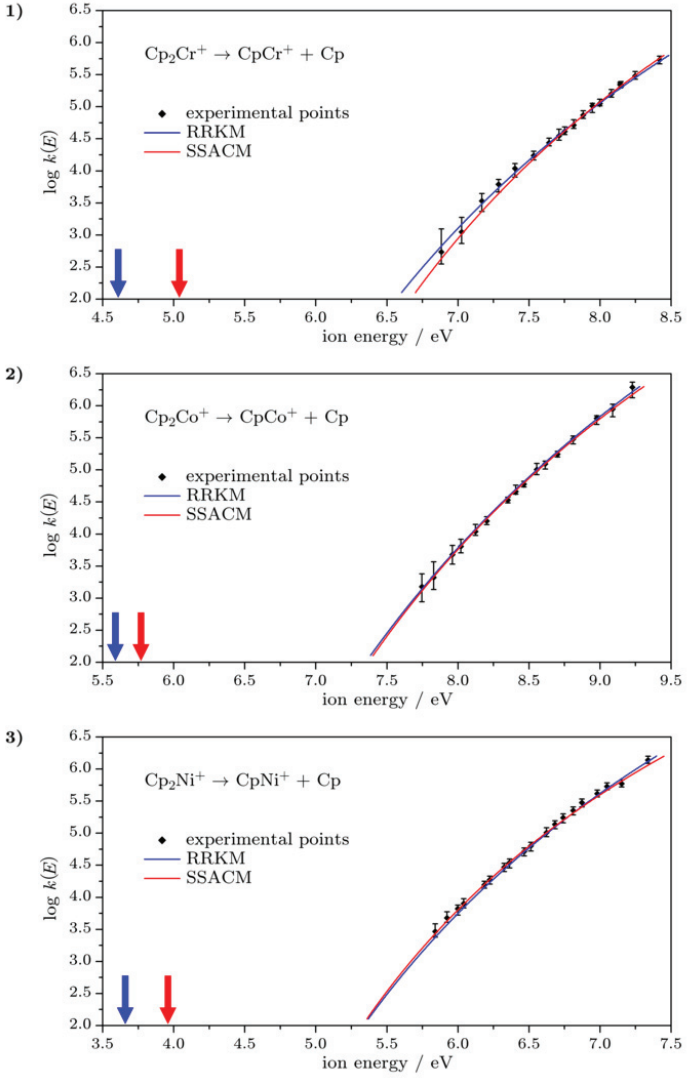

Figure 3.7: Comparison of rate curves predicted by RAC-RRKM and SSACM models to experimentally determined rate points of cyclopentadienyl loss from Cp_2Cr^+ (**1**), Cp_2Co^+ (**2**) and Cp_2Ni^+ (**3**). The arrows at the axis show the extrapolated dissociation thresholds. Determination of the rate points and their error bars is described in the text.

Table 3.4: Experimental, calculated, and literature $[CpM–Cp]^+$ *BDE*s and molecular orbital occupation of metallocene ions

	bond dissociation energies (eV)				orbital occupation[a]	
	TPEPICO[b]		calc.[c]	literature	CpM^+	Cp_2M^+
	RAC-RRKM	SSACM				
Cp_2Cr^+	4.61 ± 0.12[d]	5.04 ± 0.12[d]	4.0	6.55 ± 0.15[e]	$e_2^2a_1^1e_1^1$	$e_{2g}^2a_{1g}^1$
Cp_2Mn^+	3.43 ± 0.17[f]		2.8		$e_2^2a_1^1e_1^2$	$e_{2g}^2a_{1g}^1e_{1g}^1$
Cp_2Fe^+			3.6	3.7 ± 0.3[g]	$e_2^3a_1^1e_1^2$	$e_{2g}^3a_{1g}^2$
				3.95 ± 0.5[h]		
				6.7 ± 0.2[i]		
Cp_2Co^+	5.59 ± 0.14[d]	5.77 ± 0.11[d]	4.0	7.79 ± 0.15[e]	$e_2^4a_1^1e_1^2$	$e_{2g}^4a_{1g}^2$
				6.3 ± 1.0[j]		
				4.86 ± 0.5[k]		
Cp_2Ni^+	3.66 ± 0.16[d]	3.96 ± 0.11[d]	3.0	5.43 ± 0.15[e]	$e_2^4a_1^2e_1^2$	$e_{2g}^4a_{1g}^2e_{1g}^1$
				5.2 ± 1.0[j]		
				3.24 ± 0.07[l]		

[a] Cauletti et al. and Evans et al. [56,57] [b] Recommended values with the model uncertainty taken into account: (5.04 ± 0.16) eV for Cp_2Cr^+, (5.77 ± 0.15) eV for Cp_2Co^+, and (3.96 ± 0.15) eV for Cp_2Ni^+ [c] Calculated values at the BSSE-corrected B3LYP/6-311++G(2df,2pd)//B3LYP/6-311G(d,p) level of theory [d] This work [e] Müller and D'Or [71] [f] Li et al. [70] [g] Faulk and Dunbar [279] [h] Han et al. [280] [i] Barfuss et al. [281] [j] Pignataro and Lossing [72] [k] Opitz [75] [l] Lin and Dunbar [78]

This yields ionic bond dissociation energies of (5.04 ± 0.16), (5.77 ± 0.15), and (3.96 ± 0.15) eV for M = Cr, Co, and Ni, respectively. The derived and literature bond energies with the obtained uncertainties are summarized in Table 3.4. As usual, the early electron impact appearance energies and bond dissociation energies are much larger than the TPEPICO values [71–74,76,77]. Interestingly, the most recent electron ionization study of Opitz [75] suggests a $CpCo^+$ appearance energy of 10.21 eV and $[CpCo–Cp]^+$ bond energy of (4.86 ± 0.5) eV, which is significantly lower than our result, possibly due to neglect of the thermal energy distribution in data analysis. A time-resolved photodissociation study using an RAC-RRKM model gave a $[CpNi–Cp]^+$ bond energy of (3.24 ± 0.07) eV [78], smaller than our SSACM values by about 0.7 eV. The large difference can be attributed to the lack of detailed rate data as the calculated RAC-RRKM rate curve was fitted to only two rate points. It is important to note, however, that the lower rate point in this experiment is clearly far outside the uncertainty of either the SSACM or the RAC-RRKM rate curves that fit to our measured dissociation rates, possibly due to comparable IR emission rate at this energy. Moreover, the use of RAC-RRKM is likely to contribute a difference of several tenths of electronvolts compared to SSACM [234, 277, 278].

Our experimentally determined bond dissociation energies were compared to calculations at the BSSE-corrected B3LYP/6-311++G(2df,2pd)//B3LYP/6-311G(d,p) level of theory. It seems that the agreement between calculated and measured values is poor; the B3LYP results are usually lower than the experiments, by different amounts

for the different species; although some trends along the series are predicted correctly. The most probable reason for the failure is that this theoretical approach cannot provide a detailed account for the effects arising from the changes in the partially filled metal *d* shells upon dissociation.

3.2.3 Bond Dissociation Energy Trend

In order to analyze the trends in the $[CpM–Cp]^+$ *BDE*s along the first row of transition metals, we complemented the data coming from the present work with values for manganocene and ferrocene (Table 3.4). The bond energy data of the manganocene ion comes from an earlier TPEPICO study [70]. For the $[CpFe–Cp]^+$ dissociation energy, there is no agreement in the literature on a reliable bond energy. We listed two low values, both based on time-resolved laser photodissociation experiment by Faulk and Dunbar [279]. The slightly higher value of 3.95 eV [280] uses one extra rate point to correct the RAC-RRKM extrapolation in the original Dunbar paper. A photoionization mass spectrometry study by Barfuss et al. [281] concludes a $[CpFe–Cp]^+$ bond energy that is 3 eV higher but fails to take kinetic shift into account and, therefore, represents only a far upper limit.

The trends in the $[CpM–Cp]^+$ *BDE*s can be interpreted qualitatively on the basis of electronic structure changes upon dissociation. In Figure 3.8, we depict the orbital interactions upon the formation of Cp_2M from CpM and Cp fragments. For the metallocenes, only the orbitals with varying occupation numbers are indicated; a detailed description of the orbital structures of Cp_2M and CpM can be found in the organometallic literature [58]. The labeling in Figure 3.8 corresponds to D_{5d} (Cp_2M) and C_{5v} (CpM) symmetries. The e_{2g} orbital of Cp_2M has a bonding character with respect to the CpM–Cp bond, due to the favorable overlap of π_3 and the metal-centered lobes of e_2, while e_{1g} is an antibonding combination originating mainly from e_1 and π_2. Note that the increase of symmetry puts restrictions on how the fragment orbitals will mix to form these higher-symmetry orbitals (see reference [58]), but this does not affect the present considerations. Both a_1 and a_{1g} are essentially nonbonding metal-centered d_{z^2}-type orbitals with 4–8 % s character.

Interpretation of *BDE* changes along the Cr . . . Ni series is now possible if we examine the stepwise changes in the electronic configuration of CpM^+ and Cp_2M^+. It must be noted that the following analysis neglects the correlation interaction among the electrons, the variation of metallocene orbital energies with the metal, and the Jahn–Teller distortion; it is therefore not expected to explain all subtleties of the *BDE* trends. On the basis of the low coordination number and analogous literature results for benzene complexes [282], we assume that all CpM^+ species have high-spin configurations involving the e_2, a_1, and e_1 orbitals. These orbital occupations (from ${e_2}^2{a_1}^1{e_1}^1$ for Cr up to ${e_2}^4{a_1}^2{e_1}^2$ for Ni) of the CpM^+ ions are listed in Table 3.4. For the Cp_2M^+ ions, the electronic configurations were obtained from He I photoelectron spectra [56, 57], and these configurations are also collected in Table 3.4. As found by

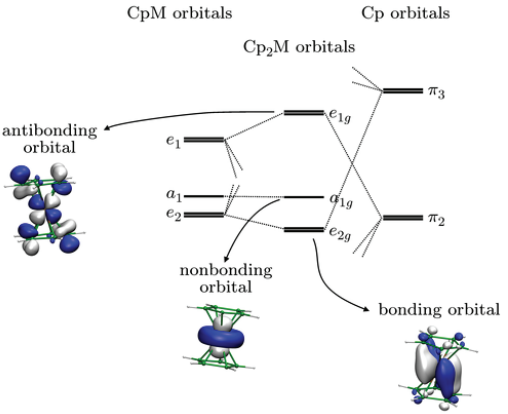

Figure 3.8: Part of the molecular orbital structure in metallocenes and its formation from CpM and Cp fragments

Long [54], simple quantum chemical calculations could not always reproduce the most stable configurations; in this analysis we used the experimental ones.

In order to understand the trends in the bond energies, one has to consider the trend in the changes upon dissociation (or, oppositely, upon bond formation) rather than just the trend in the Cp_2M^+ molecular orbital occupations themselves. The clearest argument for this is probably the striking difference between the Cr–Mn and Co–Ni pairs, where the addition of an extra e_{1g} electron results in a *BDE* decrease of 1.2 eV versus 1.8 eV. For all five metallocenes considered, after bond formation the electrons originally occupying the a_1 and e_2 orbitals in CpM^+ are now on the a_{1g} and e_{2g} orbitals, respectively. Also, a common motif is that one e_1 electron together with the three Cp π_2 electrons completes the doubly degenerate bonding orbital formed by the overlap of the e_1 and the π_2 orbitals. The main difference in the series is what happens to the other e_1 electron. For Mn and Ni, the extra electron is promoted to the antibonding e_{1g} orbital, while for Fe and Co, it is stabilized on the a_{1g} orbital. In $CpCr^+$, there is no second e_1 electron. According to this, Cp_2Fe^+ and Cp_2Co^+ should have the highest *BDE* and Cp_2Mn^+ and Cp_2Ni^+ should have the least stable bond, with Cp_2Cr^+ in between. The difference between bonding in the manganocene and nickelocene ions is the stabilization of two extra e_2 electrons to the e_{2g} orbital due to favorable overlap with the π_3 orbital of the Cp ring. Therefore, Cp_2Ni^+ is likely to have a higher *BDE* than Cp_2Mn^+. Similar arguments hold between the ferrocene and cobaltocene ions, with the latter having an extra e_2 electron. Furthermore, the cobaltocene ion exhibits the most stable 18-electron configuration, which results in extra stabilization. This is in line with the calculations on the entropy of ionization as well. The above reasoning suggest a *BDE* trend of $Cp_2Mn^+ < Cp_2Ni^+$

$< Cp_2Cr^+ < Cp_2Fe^+ < Cp_2Co^+$. Comparison with the experimental *BDE* values in Table 3.4 indeed confirms this trend with the notable exception of ferrocene, for which we do not have TPEPICO data, due to the high ionization energy. If the above considerations based on orbital occupation are correct, the bond energy from the laser photodissociation study of Faulk and Dunbar [279] is probably too low, and a synchrotron-based PEPICO study of ferrocene is warranted.

3.2.4 Conclusions

In the TPEPICO experiments for chromocene, cobaltocene, and nickelocene, the dissociation of the Cp_2M^+ ions was found to proceed by the parallel loss of neutral cyclopentadienyl ligand, CH, and C_2H_2 groups. In addition, isomerization of nickelocene occurs, yielding a complex with pentafulvalene $C_{10}H_8$ and H_2 ligands, subsequently undergoing H_2 loss.

The SSACM modeling of the measured TOF distributions and breakdown diagrams provided reliable 0 K appearance energies of CpM^+ ions and by combining them with the adiabatic ionization energies, $[CpM–Cp]^+$ bond dissociation energies were obtained.

In accordance with an earlier study [277], a comparison of the rigid activated complex RAC-RRKM model with SSACM indicates that both theories are capable of fitting the rates over a broad range, but RAC-RRKM predicts significantly lower AE_0s.

The trend in the experimental $[M–Cp]^+$ bond dissociation energies determined in this work agrees well with the predictions from a simple molecular orbital picture of the electronic structure of the Cp_2M^+ and CpM^+ ions with the notable exception of Cp_2Fe^+, for which there is no PEPICO data available.

Section 3.3

Copper–Pyridine Complexes

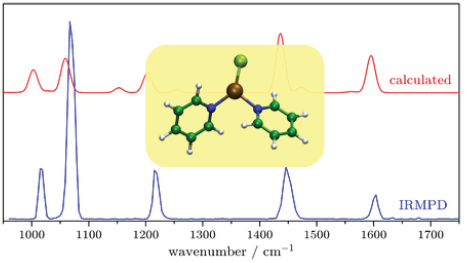

Á. Révész, P. Milko, J. Žabka, D. Schröder, J. Roithová
Journal of Mass Spectrometry, **2010**, *45*, 1246–1252

We carried out collision-induced dissociation mass spectrometric (CID-MS) experiments, coupled with electrospray ionization (ESI), in order to probe the effect of pyridine ligand on the stability of Cu^{II} species, and to further investigate the possibility of obtaining approximate bond dissociation energies using this instrumentation. The copper-containing ions of interest were generated from the water solution of copper(II) chloride with added pyridine; we also added about 1 % ammonia to prevent the precipitation of copper(II) hydroxide.

3.3.1 Mass Spectra and Breakdown Diagrams

ESI of aqueous copper(II) chloride, $CuCl_2$, in the presence of traces of pyridine leads to the formation of intense signals due to the cationic species $(py)_2CuCl^+$ under soft ionization conditions. Upon gradual enforcement of the conditions of ionization, the major copper-containing cations correspond to the formal Cu^I species, namely $(py)_2Cu^+$, $(py)Cu^+$ and finally bare Cu^+ [198].

CID spectra of the mass-selected cations $(py)_2Cu^+$ and $(py)_2CuCl^+$ in the IT-MS were recorded at several collision energies; typical results are shown in Figure 3.9. In the CID spectra of the Cu^I-containing cation $(py)_2Cu^+$ ($m/z = 221$ for the ^{63}Cu isotope), two fragment ions are observed. One of them corresponds to the loss of pyridine (Reaction 3.13, see below) resulting in $(py)Cu^+$ ($m/z = 142$), whereas the other one corresponds to $(py)Cu(H_2O)^+$ ($m/z = 160$). The two channels appear practically at the same collision energy (see in subsequent paragraphs), which indicates that the $(py)Cu(H_2O)^+$ is formed via the sequential occurrence of Reactions 3.13 and 3.14; namely, $(py)_2Cu^+$ first loses a pyridine ligand, and in the second step, the monoligated $(py)Cu^+$ gains a water molecule present in the IT-MS as a background forming the $(py)Cu(H_2O)^+$ cation.

$$(py)_2Cu^+ \longrightarrow (py)Cu^+ + py \tag{3.13}$$

$$(py)Cu^+ + H_2O \longrightarrow (py)Cu(H_2O)^+ \tag{3.14}$$

$$(py)_2CuCl^+ \longrightarrow (py)_2Cu^+ + Cl^\bullet \tag{3.15}$$

$$(py)_2CuCl^+ \longrightarrow (py)CuCl^+ + py \tag{3.16}$$

In the case of $(py)_2CuCl^+$ ($m/z = 256$), a formal Cu^{II} species, the major fragmentation is the loss of Cl leading to $(py)_2Cu^+$ as ionic fragment (Reaction 3.15). A small amount of $(py)CuCl^+$ ($m/z = 177$) can be observed only at elevated energies (Reaction 3.16).

From the energy-dependent CID spectra, the corresponding breakdown diagrams are derived by plotting the relative fractional abundances as a function of the collision energies applied (see Figure 3.10). In this representation, the points correspond to the experimental data, whereas the solid lines show the result of a fitting by sigmoid functions. We note in passing that in the breakdown diagrams, a minor amount of $(py)_2CuCl(H_2O)^+$ was added to $(py)_2CuCl^+$ parent ion. Additional support to this simplification is lent by CID experiments at increased trapping times which leads to increased abundance of this secondary product.

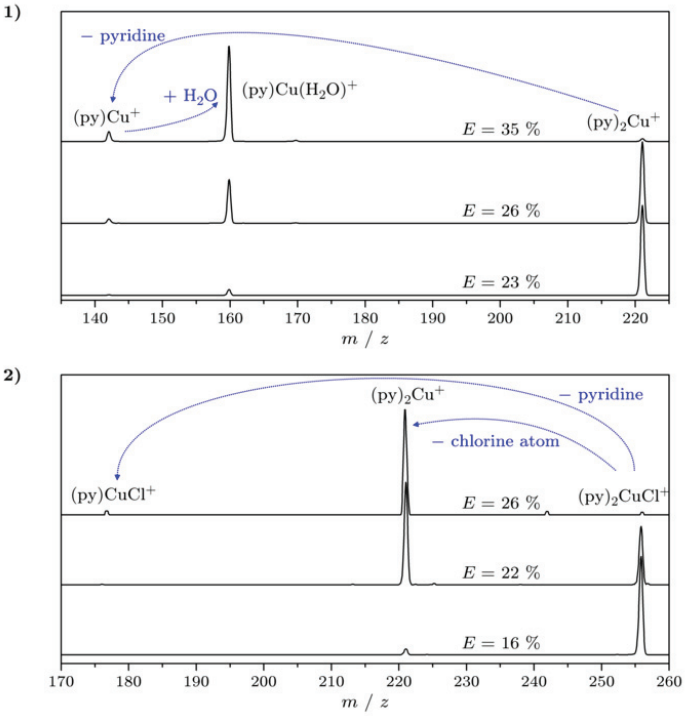

Figure 3.9: CID spectra of mass-selected $(py)_2Cu^+$ (**1**) and mass-selected $(py)_2CuCl^+$ (**2**) at selected relative collision energies

3.3.2 Data Analysis

In Figures 3.9 and 3.10, the collision energies are given as percentages of the maximal excitation amplitude. In order to provide a crude conversion of these relative collision energies into absolute values, the breakdown curves were first fitted by sigmoid functions (Equations 2.4 and 2.5, page 27). The appearance energies (*AE*s) were obtained by linear extrapolation of the slope of the breakdown curve at $E_{1/2}$ to the baseline (this procedure compensates for differences in slopes) and then the energy scale was calibrated using well-established data from the literature. Note that the appearance energies here correspond to the process of forming daughter ions from parent ions, i.e., within the errors of the method they directly correspond to the bond dissociation energies.

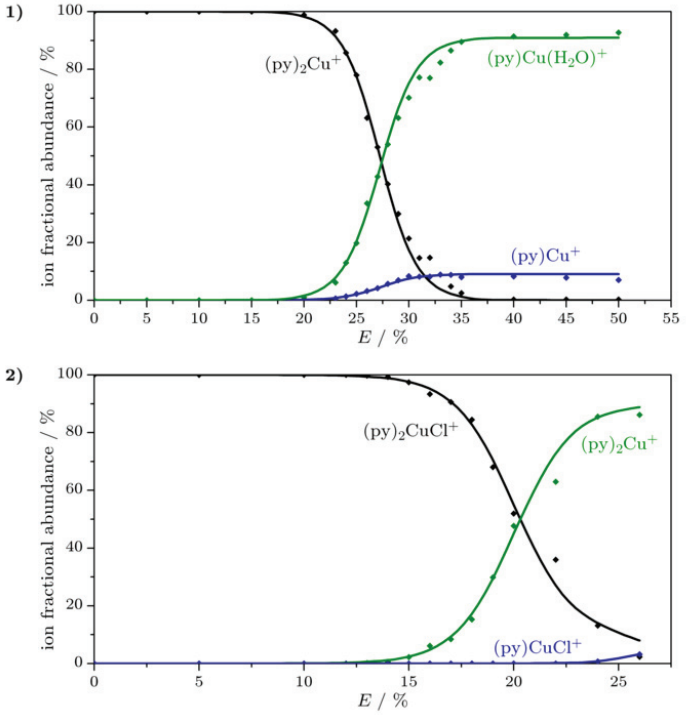

Figure 3.10: Breakdown diagrams of mass-selected $(py)_2Cu^+$ (**1**) and mass-selected $(py)_2CuCl^+$ (**2**) as a function of relative collision energies. The dots are the experimental data and the solid lines are the sigmoid functions used for analysis.

As it was mentioned earlier, the complicated situation in IT-MS does not allow us to directly model the processes occuring in the ion trap. However, this purely phenomenological approach appears to be a fair first-order approximation for an estimation of dissociation threshold. Considering the conditions in the ion trap indeed leads to a shape reasonably close to sigmoid functions. Namely, after mass-selection, the parent ion is trapped in helium buffer gas at a pressure of about 10^{-3} mbar at a timescale from milliseconds to several seconds, where it undergoes multiple collisions with helium, which have been proposed to bring about ion thermalization [203]. Collision-induced dissociation is carried out by applying an AC pulse which kinetically excites the parent ion such that energizing collisions with the helium buffer gas occur. Due to the small mass of helium, the occurrence of numerous collisions is required

prior to ion dissociation. Hence, to a first approximation, we may consider this mode of excitation as thermal activation in the multicollision regime. Accordingly, an Arrhenius-type behavior might be assumed, i.e., the rate constant of dissociation k_{CID} is given by the following equation:

$$k_{\mathrm{CID}} = A_0 \exp\left(-\frac{E_0}{k_{\mathrm{B}} T_{\mathrm{eff}}}\right) \tag{3.17}$$

where A_0 is the preexponential factor, E_0 is the activation energy, k_{B} is Boltzmann's constant and T_{eff} is an effective temperature describing ion dissociation without a direct physicochemical meaning. In the experiments described here, the dissociation time t_{diss} is kept constant ($t_{\mathrm{diss}} = 20$ ms), while the excitation amplitude is varied which may be expressed as increase of T_{eff}. The amount of dissociation as expressed by the relative abundance of daughter ions is thus given by:

$$I_{\mathrm{D}^+} = 1 - I_{\mathrm{P}^+} = 1 - \exp(-k_{\mathrm{CID}} \times t_{\mathrm{diss}}) \tag{3.18}$$

If the AC energy deposited in the parent ion does not suffice for fragmentation, I_{D^+} is zero, at a certain threshold, dissociation starts to occur and I_{D^+} increases until no parent is left and the plateau value of $I_{\mathrm{D}^+} = 1$ is reached. If we model the dissociation of a hypothetical parent ion using Equation 3.17 and 3.18 with an activation energy set to $E_0 = 2\,\mathrm{eV}$ and $t_{\mathrm{diss}} = 20\,\mathrm{ms}$ as well as $A_0 = 10^7\,\mathrm{s}^{-1}$ as the only additional parameters, we end up with curves that closely resemble sigmoids. We would like to point out that this pragmatic view does not address the actual situation of the ions excited in the trap, as their internal energy is not only determined by the excitation pulse, but simultaneously by cooling in collisions with helium.

For the two fragmentation channels of $(py)_2Cu^+$, i.e. $(py)Cu^+$ and $(py)Cu(H_2O)^+$ this method yields appearance energies of (23.5±0.5) % and (23.6±0.6) %, respectively, in the relative energy scale of the IT-MS. The error bars were determined by changing the parameters of the sigmoid curve up to a point where the fit became unacceptable. The fact that the fragments $(py)Cu^+$ and $(py)Cu(H_2O)^+$ have practically identical *AE*s leads to the above conclusion that the formation of $(py)Cu(H_2O)^+$ occurs in a stepwise manner, i.e., first Reaction 3.13, then Reaction 3.14 (page 70). Instead, for a one-step ligand-switching reaction, the *AE* of $(py)Cu(H_2O)^+$ should be significantly lower than that of $(py)Cu^+$ by $[(py)Cu\text{–}H_2O]^+ = (1.63 \pm 0.09)$ eV bond dissociation energy [283].

We used the loss of pyridine from $(py)_2Cu^+$ as a reference to calibrate the energy sclale of our IT-MS for which a bond energy of $[(py)Cu\text{–}py]^+ = (2.45 \pm 0.09)$ eV has been established [113, 114]. Further, following a suggestion of O'Hair et al. [135], we additionally subjected the mass-selected cations $Ag(CH_3OH)^+$ (*BDE* = (1.58 ± 0.08) eV) and $Ag(CH_3OH)_2^+$ (*BDE* = (1.43 ± 0.07) eV) [284] to CID. Both cations could be generated by ESI of a dilute methanolic solution of silver(I) tosylate, and we obtained appearance energies of (15.35 ± 0.5) and (13.45 ± 0.5) %, respectively, for the loss of a methanol molecule from them. Likewise, ferrocenylium ion Cp_2Fe^+ (literature *BDE* = (3.95 ± 0.05) eV [280]) was generated by ESI of ferrocenylium hexafluorophosphate, and gave an appearance energy of (37.6 ± 1.0) % for the loss

Table 3.5: Derived and literature bond dissociation energies (in eV)

	Theory	Experiment	
Complex	B3LYP/TZVP[a,b]	IT-MS[b]	Literature[c]
$[Cu–py]^+$	2.80		2.72 ± 0.08
$[(py)Cu–py]^+$	2.42	–[d]	2.45 ± 0.09
$[(py)_2Cu–py]^+$	0.57		0.85 ± 0.02
$[(py)_2Cu–Cl]^+$	1.24	1.73 ± 0.16[e]	
$[(py)CuCl–py]^+$	1.94	2.61 ± 0.27[e]	

[a] BSSE-corrected B3LYP/TZVP on B3LYP/TZVP geometries.
[b] This work.
[c] From TCID measurements [113, 114].
[d] Anchor value for the conversion factor.
[e] The final uncertainties of the bond dissociation energies include the error of the conversion factor, the error of the experimental thresholds and the error of the reference value. These errors are independent from each other; therefore we used the error propagation in terms of square roots.

of one Cp unit. From the linear correlation of the reference binding energies and the measured appearance energies with the constraint to meet the origin, we derive a phenomenological factor of (0.105 ± 0.002) eV $\%^{-1}$ for the conversion of the relative collision energies in percentage into 0 K *BDE*s in eV under our experimental conditions ($t_{\mathrm{diss}} = 20$ ms, $q_z = 0.25$).

Accordingly, we modeled the breakdown curves of the measurements of $(py)_2CuCl^+$ in order to determine the copper–chlorine and copper–pyridine *BDE*s of $(py)_2CuCl^+$. As Figure 3.10/2 shows, the pyridine loss appears as a minor channel at elevated energies besides the predominating chlorine atom loss. Using the same fitting procedure and the conversion factor derived above, we arrive at $[(py)_2Cu–Cl]^+ = (1.73 \pm 0.16)$ eV and a rough estimate of $[(py)CuCl–py]^+ = (2.61 \pm 0.27)$ eV, where the increased uncertainty of the latter is due to the low intensity of this channel (see Table 3.5). Note that the provided error bars of the obtained bond energies does not contain the inherent inaccuracy of the present method; its quantification requires a more detailed assessment. Some work has already been done along these lines [285].

3.3.3 Structural and Energetic Trends

Computed Structure of Copper–Pyridine Complexes

In order to analyze the trends among simple copper complexes in more detail, we carried out quantum chemical calculations at the B3LYP/TZVP level. The optimized geometries of the investigated species are shown in Figure 3.11. The results suggest

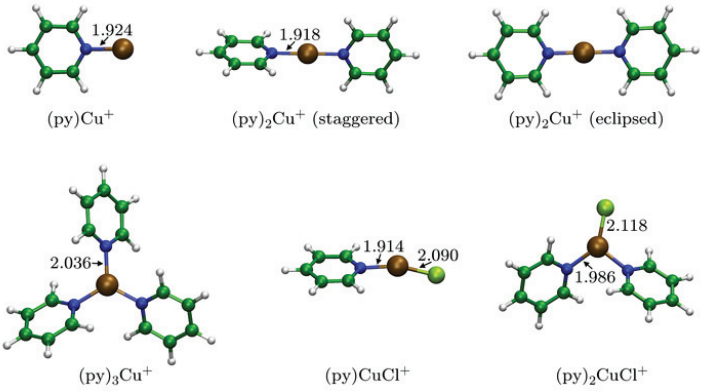

Figure 3.11: B3LYP/TZVP-optimized geometries of the relevant ionic species

that Cu^{I}/Cu^{II} prefers to bind to the lone pair(s) of electrons on the nitrogen atoms rather than the π system of the aromatic ring(s) in all investigated complexes. This preference was earlier found in several Cu^{I} species with a wide variety of aromatic *N*-donor ligands [113–117, 286]. The π-type structures—if any local minima at all—were found to be higher in energy by more than 1 eV. In addition, the arrangement of the ligands around Cu^{+} approaches the ideal structures predicted by the valence shell electron pair repulsion model. Thus, the species $(py)Cu^{+}$ is obviously planar, whereas $(py)_2Cu^{+}$ might have two geometries, that is, the two pyridine moieties can lie in orthogonal (staggered) or planar (eclipsed) conformation. In accordance with previous results, our computations predict the staggered conformation to be more stable. On the contrary, Wang et al. found, based on zero electron kinetic energy spectroscopic measurements, that the eclipsed conformation is more probable [286]. However, the calculated barrier between the two conformers is quite small, such that free rotation around the Cu–N bonds is likely to occur in the experiments conducted at 298 K. Interestingly, $(py)CuCl^{+}$ was found to have a bent geometry; similarly, in $(py)_2CuCl^{+}$ and $(py)_3Cu^{+}$, the arrangement around the copper is trigonal planar but the two NCuCl angles in the former and the three NCN angles in the latter species are not identical; Jahn–Teller distortion might be responsible for these effects. The changes in geometry of the pyridine ligand upon binding to Cu^{I}/Cu^{II} are minor and are largest for monoligated $(py)Cu^{+}$ while decreasing with increasing number of ligands. The Cu–N bond lengths in $(py)Cu^{+}$ and $(py)_2Cu^{+}$ are very close to each other, whereas in $(py)CuCl^{+}$ it is slightly below both of them, which can be understood as a result of an increased electrostatic attraction between copper and pyridine due to the presence of the electron-withdrawing chloro ligand [287, 288]. Coordination of another pyridine molecule to both $(py)_2Cu^{+}$ and $(py)CuCl^{+}$ causes elongation of

the Cu–N bond, which can be attributed to increased steric demands. Similarly, the Cu–Cl bond length is larger in $(py)_2CuCl^+$ than in $(py)CuCl^+$.

IRMPD Results on $(py)_2CuCl^+$

As an additional experimental probe of the structure of the $(py)_2CuCl^+$ cation, the infrared spectrum of the mass-selected ion has been recorded with a Bruker Esquire 3000 IT-MS mounted to the beamline of a free electron laser at CLIO (Centre Laser Infrarouge Orsay, France) [289]. The $(py)_2CuCl^+$ ions generated via ESI were transferred into the ion trap, and after mass selection, infrared multiphoton dissociation (IRMPD) [290, 291] was induced by admittance of four pulses of IR laser light to the ion trap, resulting in a total trapping time of about 0.4 second. In the 45 MeV range in which CLIO was operated in these experiments, the IR light covers a spectral range from about 950 to 1750 cm^{-1}. Note that in this kind of action spectra, the assumption that the amount of ion fragmentation is proportional to the IR absorbance is not always justified due to the multiphotonic nature of IRMPD and the major weight is therefore put on the peak positions, rather than the peak heights in the IRMPD spectra [292, 293]. As far as the band positions are concerned, a very good agreement between experiment and theory is obtained in the spectral range sampled (Figure 3.12). With regard to the sensitivity of IR spectra for the molecular structure, we note that the different conformers arising from different orientations of one of the σ-bonded pyridine ligand to the other have very similar infrared patterns and thus, a distinction by means of IRMPD is impossible. In contrast, ions with different binding modes are often quite distinguished. For example, the computed structure of $(py)_2CuCl^+$ with one σ- and one π-type pyridine ligand has three intense bands in the region around 1600

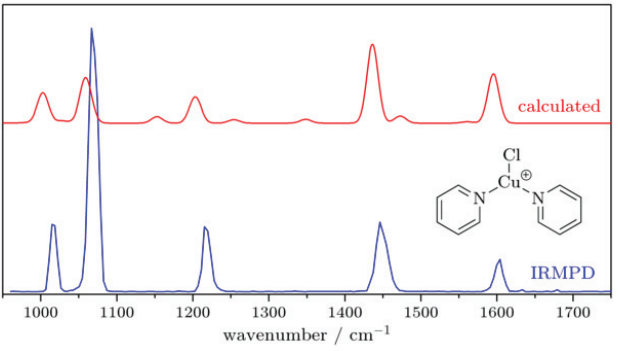

Figure 3.12: Measured IRMPD (blue) and calculated IR (red) spectra of $(py)_2CuCl^+$ in the range between 950 and 1750 cm^{-1}. For the calculated frequencies, a scaling factor of 0.97 was used.

cm^{-1}. Given only a single adsorption in this range in Figure 3.12, the contribution of the π-type isomer to the experimental IRMPD spectrum can thus safely be excluded.

Discussion of Bond Dissociation Energies

The calculated B3LYP/TZVP bonding energies of pyridine, $[Cu–py]^+_{calc} = 2.80$ eV and $[(py)Cu–py]^+_{calc} = 2.42$ eV are in reasonable agreement with the experimental values (2.72 and 2.45 eV, respectively) [113,114]. The experimentally derived *AE*s for chlorine atom and pyridine losses from $(py)_2CuCl^+$ are (1.73 ± 0.16) and (2.61 ± 0.27) eV, respectively. Both values are somewhat larger than the calculated values of $[(py)_2Cu–Cl]^+_{calc} = 1.24$ eV and $[(py)CuCl–py]^+_{calc} = 1.94$ eV. On taking the approximate character of the conversion scheme for the collision energies into account as well as due to the fact that the calculations underestimate the dissociation energies by 0.2–0.3 eV when copper has more than two ligands [113,114], the agreement is considered reasonable, however. Moreover, the pyridine loss is likely to bear an elevated *AE* due to the operation of competitive shift [213]. We note in passing that in the particular case of the loss of atomic chlorine from $(py)_2CuCl^+$, entropic effects may play a role which could shift the threshold associated with loss of the atom upwards by about 0.10 eV [294].

The experiments thus indicate that the coordinative bond to the pyridine ligand is significantly stronger than the covalent bond between copper and chlorine. Stace and coworkers derived similar conclusions in their studies of the stability of redox states as a function of microsolvation [90, 93, 96], and also in the case of gaseous Au^I/Au^{II}, such cases are known [295, 296]. The preference for the loss of Cl atom may originate from the fact that it leads to $(py)_2Cu^+$, in which Cu^I is coordinated by two nitrogen ligands in linear geometry, an ideal situation for Cu^I [92]. In the alternative fragmentation route leading to $(py)CuCl^+$ as the second fragment ion, the copper stays in the formal oxidation state II. As Cu^{II} is better stabilized by having more ligands (four to six) [91], the generation of this ion is less favorable. In line with this, the dissociation energy of $[(py)_2Cu–py]^+$ is significantly smaller not only than $[(py)Cu–py]^+$, but also than $[(py)CuCl–py]^+$ and $[(py)_2Cu–Cl]^+$. We note in passing that this finding explains also the very efficient reaction of $(py)Cu^+$ with the background water (Reaction 3.14, page 70).

3.3.4 Conclusions

Upon CID, $(py)_2Cu^+$ loses a pyridine ligand, whereas the major fragmentation of $(py)_2CuCl^+$ corresponds to a loss of chlorine atom. The observed trends in dissociation energies and fragmentation pathways can be explained as a response of the Cu^I/Cu^{II} redox couple to the changes of the coordination sphere. In particular, the Cu^{II} species $(py)_2CuCl^+$ prefers to lose a chlorine radical and thereby to convert into a Cu^I complex with two pyridine ligands, whereas the alternative loss of a closed shell pyridine ligand is less favorable due to the decreased stability of the resulting Cu^{II} species $(py)CuCl^+$.

These studies furthermore indicate that IT-MS can be used for estimation of *BDE*s, however, in order to get more justification, more systems, ions of different mass ranges as well as sizes need to be included in the test of the calibration process. Inital studies appear motivating to go further in this direction [285].

Section 3.4

Copper–Disulfide Interaction

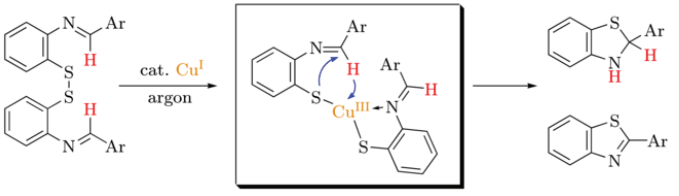

J. Srogl, J. Hývl, **Á. Révész**, D. Schröder,
Chemical Communications, **2009**, 3463–3465

Our studies directed toward the investigation of copper–disulfide interaction have been carried out on the intramolecular reaction shown in Figure 3.13. In the synthetic experiments, one equivalent of the imine disulfide (where Ar = 2-chloro-4-nitrophenyl, **1a**) was treated with catalytic amount of copper(I) 3-methylsalicylate under inert atmosphere using acetic acid as solvent. Under these conditions, the starting material was converted to a 1 : 1 mixture of 2-arylbenzothiazole and 2,3-dihydro-2-arylbenzothiazole.

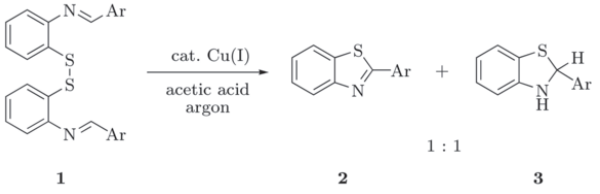

Figure 3.13: Intramolecular disproportionation reaction of imine disulfide **1** catalyzed by copper(I), yielding oxidized (**2**) and reduced (**3**) products

3.4.1 Experimental Studies

The role of the Cu^{I} as a Lewis acid resulting in a sulfur-centered cationic species was already ruled out by a simple modification of the above protocol; namely, the mixture of the imine disulfide **1a** (Ar = 2-chloro-4-nitrophenyl) and styrene was treated under the same conditions. The styrene as a nucleophile is supposed to trap the presumed electrophilic sulfur species [150]. This experiment led to same products as above, while styrene remained intact, and no other products were observed. This finding strongly suggests that no free sulfur electrophiles are formed as intermediates which could react with external nucleophiles.

An option for an alternative route is a Cu^{I} oxidative addition into the disulfidic S–S bond with subsequent hydrogen transfer leading to overall disproportionation of the imine disulfide into the corresponding benzothiazole and its dihydroderivative. In order to lend further evidence to this mechanistic proposal, the unimolecular behavior of the isolated Cu^{I} complex of imine disulfide (Ar = phenyl, denoted as **1b**) in the gas phase was investigated by mass spectrometry. Specifically, a diluted mixture of the reactant **1b** and the catalyst in methanol was probed via electrospray ionization. Schröder's group already used ESI-MS in a recent study for the direct sampling of a reactive solution in copper catalysis [105]. Under mild conditions of ionization, the reactant complex $[\mathbf{1b}{\cdot}Cu]^{+}$ is observed as a major cationic species, whose assignment is confirmed by the characteristic isotope pattern, shown in the inset of Figure 3.14. The main part of the Figure shows the collision-induced dissociation mass spectrum of mass-selected $[\mathbf{1b}{\cdot}Cu]^{+}$ (m/z = 487 for the ^{63}Cu isotope) with a product ion with m/z = 276 as major fragment, which formally corresponds to the complex of the reduced product 2,3-dihydro-2-phenylbenzothiazole (**3b**) with Cu^{I}, while the oxidized

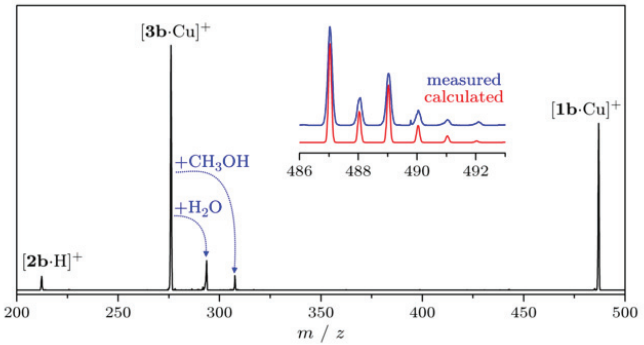

Figure 3.14: CID spectrum of mass-selected $[\mathbf{1b}{\cdot}\mathrm{Cu}]^+$ (m/z = 487 for the ^{63}Cu isotope) showing the highly preferential loss of neutral **2b** to formally afford $[\mathbf{3b}{\cdot}\mathrm{Cu}]^+$ (m/z 276). The protonated benzothiazole $[\mathbf{2b}{\cdot}\mathrm{H}]^+$ (m/z 212) arises from consecutive loss of neutral CuH from $[\mathbf{3b}{\cdot}\mathrm{Cu}]^+$. The signals at m/z 294 and 308 are due to subsequent addition of water and methanol, respectively, present as residuals from the spray solvent in the background of the mass spectrometer. The inset shows the measured and calculated isotope pattern of the $[\mathbf{1b}{\cdot}\mathrm{Cu}]^+$ precursor ion.

2-phenylbenzothiazole (**2b**) is lost as a neutral fragment. Hence, the interaction of the substrate with a single copper cation in the gas phase can bring about the same products as observed in the preparative reaction (Figure 3.13). At elevated collision energies, the primary fragment ion with m/z = 276 undergoes further dissociation to afford an ion with m/z = 212 concomitant with a loss of neutral CuH, thereby corresponding formally to $[\mathbf{2b}{\cdot}\mathrm{H}]^+$. Figure 3.14 also shows peaks at m/z = 294 and 308, which can be assigned to additions of water and methanol, respectively, present in the background of the vacuum system of the IT-MS.

The apparent threshold of this fragmentation of about 1.9 eV, determined with method described in Section 3.3.2 (page 71), is qualitatively consistent with a reaction in the condensed phase occurring at ambient conditions. Thus, the gas-phase experiments demonstrate a purely intramolecular reaction of a mononuclear copper species as a viable scenario for the overall reaction. To further support these conclusions, also the Cu^I complex of the 2-chloro-5-nitrophenyl derivative of the imine disulfide reactant (**1a**) and an isotopolog with both N=CH moieties deuterated ([D_2]-**1a**) were investigated by means of ESI-MS. Again, loss of the neutral benzothiazole is observed as the by far predominating fragmentation of mass-selected reactant complex, and for the deuterated derivative, the deuterium label is completely left in the ionic product, as expected.

3.4.2 Mechanistic Proposal

It was demonstrated that a single copper atom is sufficient for providing a plausible mechanistic rationale in the gas phase; and no free electrophiles were detected in the solution. Accordingly, we propose an oxidative addition of Cu^{I} into the S–S bond of disulfide as the first step of the catalytic cycle of the condensed-phase reaction (Figure 3.15). The resulting intermediate **X**, formally a Cu^{III} compound, subsequently undergoes a hydrogen transfer, either via a CuH species (as shown) or directly. This yields the oxidized product **2** and copper complex of **3** or that of the corresponding thiol moiety, where the latter easily forms the dihydrobenzothiazole **3** under the reaction conditions. The acidic solvent may serve to return Cu^{I} back to the catalytic cycle. An alternative to the proposed mechanism may be the reaction pathway involving a multicentered transition state [297–299], i.e., simultaneous cleavage of the S–S bond with the formation of a new C–S bond, and accompanied by hydrogen migration. This scenario would thus circumvent the oxidative addition of copper to the disulfide. Note that the loss of neutral CuH from $[\mathbf{3}{\cdot}Cu]^{+}$ (Figure 3.14) might provide an indirect evidence for the involvement of an intermediate with Cu–H bond.

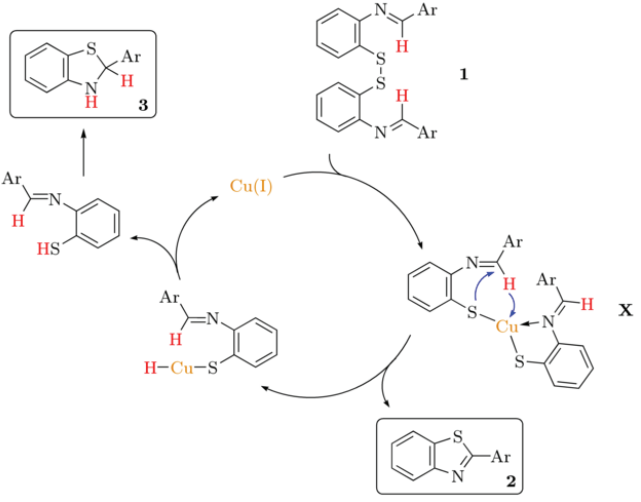

Figure 3.15: Tentative mechanism of the Cu^{I}-catalyzed intramolecular imine oxidation reaction. Imine hydrogens for which deuterium was substituted in $[D_2]$-**1a** are highlighted in red.

3.4.3 Conclusions

The intramolecular disproportionation of imine disulfides, a reaction demonstrating the possibility of using disulfides as an oxidant for Cu^{I}, was studied by ESI-MS measurements. The results show that a single Cu^{I} is sufficient for the catalytic process. On the basis of the experimental results, the involvement of an oxidative addition to form Cu^{III} species seems plausible.

Summary and Outlook

During my Ph.D. work, I have been involved in several projects that provide some examples of the wide diversity of questions gas-phase measurements can answer. Due to their advantages, like the ability of studying well-defined species in a controlled way, they are capable of producing accurate data, valuable chemical trends and mechanistic insights, complementing the information available in other experiments.

Using the TPEPICO approach, there is a possibility of generating ions with a known and narrow energy distribution, allowing the quantitative study of their decomposition kinetics. The resulting highly precise thermochemical data of transition-metal complexes not only allow understanding the various factors of metal complex stability, but they can also be used, for example, as anchor values for benchmarking quantum chemical calculations on these challenging systems.

From the TPEPICO investigation of chalcocarbonyl complexes, we were able to determine Mn–CO, and Mn–CX (X = S, Se) bond energies in $CpMn(CO)_nCX^+$ ions, and a series of related thermochemical data. The obtained values unequivocally show the much stronger CX binding to the metal center as compared to CO. Furthermore, it turned out that the changing of one CO to CS or CSe does not influence the other Mn–CO bond dissociation energies.

By the use of TPEPICO technique, we also determined the $[CpM–Cp]^+$ bond dissociation energies for M = Cr, Co, Ni. The observed trend including the manganocene data coming from an earlier study can be nicely explained on the basis of a simple model of the electronic structure of the metallocene ions. Interestingly, literature values of *BDE* for ferrocene cation do not fit this trend; the reasons remain to be explored, perhaps using supposedly more accurate syncrothron-based TPEPICO measurements.

The TPEPICO technique requires a detailed kinetic modeling to extract the data of interest. The underlying rate theory has to be chosen adequately; in agreement with previous studies, it was found for the metallocenes that RAC-RRKM leads to notably smaller bond energies than the presumably more suited SSACM theory. Future work, both theoretical and experimental, is expected to be done along these lines, which will allow more detailed conclusions on the reliability of the methods.

When there is no need for very accurate thermochemical results, but wider availability and easier evaluation are important, some other approach, such as the IT-MS, may be the method of choice. As part of the copper–pyridine project, the viability

of this technique for the determination of approximate fragmentation threshold of gaseous ions was demonstrated. Since then, this has also been confirmed by further tests on various benzylpyridinium ions [285]. In addition, the method found its use in unraveling the chemistry of several further systems [300–302].

Using IT-MS with electrospray ionization, we determined trends and approximate *BDE*s for the fragmentation of $(py)_2CuCl^+$, a model copper(II) compound containg *N*-donor ligands. This species was found to prefer the loss of the chlorine atom instead of the datively bound pyridine, which was explained to be the consequence of the formation of a species having ideal coordination sphere for Cu^I.

In the last part of this thesis, an example was shown where the determination of gas-phase fragmentation thresholds and pathways can contribute to mechanistic understanding of chemical reactions. In a preliminary study, an intramolecular disproportionation of imine disulfides was found to proceed with catalysis by a single copper atom; on the basis of this, a tentative mechanism of the reaction was proposed. In order to answer the questions left open, detailed quantum chemical investigations and further gas-phase experiments including IRMPD and H/D exchange measurements are in progress.

References

[1] L. Mond, *J. Chem. Soc.* **1890**, *57*, 749.

[2] C. Elschenbroich, *Organometallics*, WILEY-VCH, Weinheim, **2006**.

[3] N. N. Greenwood, A. Earnshaw, *Chemistry of the Elements*, Pergamon Press, Oxford, **1984**.

[4] G. W. Bethke, M. K. Wilson, *J. Chem. Phys.* **1957**, *26*, 1118.

[5] T. Ogura, R. D. Mounts, Q. Fernando, *J. Am. Chem. Soc.* **1973**, *95*, 951.

[6] W. Kutzelnigg, *Angew. Chem., Int. Ed.* **1984**, *23*, 272.

[7] W. G. Richards, *Trans. Faraday Soc.* **1967**, *63*, 257.

[8] S. Smoes, J. Drowart, *J. Chem. Soc., Faraday Trans. 2* **1977**, *73*, 1746.

[9] S. Rosenwaks, I. W. M. Smith, *J. Chem. Soc., Faraday Trans. 2* **1973**, *69*, 1416.

[10] K. J. Klabunde, C. M. White, W. E. Efner, *Inorg. Chem.* **1974**, *13*, 1778.

[11] R. Steudel, *Angew. Chem., Int. Ed.* **1967**, *6*, 635.

[12] R. Steudel, *Z. Anorg. Allg. Chem.* **1968**, *361*, 195.

[13] R. Steudel, *Z. Anorg. Allg. Chem.* **1968**, *361*, 180.

[14] P. V. Broadhurst, *Polyhedron* **1985**, *4*, 1801.

[15] G. M. Bodner, *Inorg. Chem.* **1974**, *13*, 2563.

[16] D. Cozak, I. S. Butler, I. M. Baibich, *J. Organomet. Chem.* **1979**, *169*, 381.

[17] J. P. Hickey, I. M. Baibich, I. S. Butler, L. Todd, *J. Spectrosc. Lett.* **1978**, *11*, 671.

[18] A. Efraty, D. Liebman, M. H. A. Huang, C. A. Weston, R. J. Angelici, *Inorg. Chem.* **1978**, *17*, 2831.

[19] M. V. McCabe, J. F. Terapane, M. Orchin, *J. Org. Chem.* **1975**, *14*, 281.

[20] F. Hebrard, P. Klack, *Chem. Rev.* **2009**, *109*, 4272.

[21] D. Evans, J. A. Osborn, G. Wilkinson, *J. Chem. Soc. A* **1968**, 3133.

[22] D. Mansuy, J. P. Battioni, J. C. Chottard, *J. Am. Chem. Soc.* **1978**, *100*, 4311.

[23] P. Braunstein, M. Knorr, E. Villaroya, A. De Cian, J. Fischer, *Organometallics* **1991**, *10*, 3714.

[24] L. Busetto, A. Palazzi, *Inorg. Chim. Acta* **1976**, *19*, 233.

[25] G. D. Michels, G. D. Flesch, H. J. Svec, *Inorg. Chem.* **1980**, *19*, 479.

[26] G. Simonneaux, G. Jaouen, R. Dabard, P. Guenot, *J. Organomet. Chem.* **1977**, *132*, 231.

[27] A. Efraty, M. H. A. Huang, C. A. Weston, *Inorg. Chem.* **1975**, *14*, 2796.

[28] A. Efraty, D. Liebman, M. H. A. Huang, C. A. Weston, *Inorg. Chim. Acta* **1980**, *39*, 105.

[29] A. Efraty, M. H. A. Huang, *Inorg. Chem.* **1980**, *19*, 2296.

[30] I. Kretzschmar, D. Schröder, H. Schwarz, C. Rue, P. B. Armentrout, *J. Phys. Chem. A* **2000**, *104*, 5046.

[31] I. Kretzschmar, D. Schröder, H. Schwarz, P. B. Armentrout, *Int. J. Mass Spectrom.* **2003**, *228*, 439.

[32] D. Schröder, I. Kretzschmar, H. Schwarz, C. Rue, P. B. Armentrout, *Inorg. Chem.* **1999**, *38*, 3474.

[33] I. Kretzschmar, D. Schröder, H. Schwarz, P. B. Armentrout, *Int. J. Mass Spectrom.* **2006**, *249*, 263.

[34] G. H. Jeung, *J. Am. Chem. Soc.* **1992**, *114*, 3211.

[35] C. Von Wüllen, *J. Chem. Phys.* **1996**, *105*, 5485.

[36] S. Dapprich, U. Pidun, A. W. Ehlers, G. Frenking, *Chem. Phys. Lett.* **1995**, *242*, 521.

[37] J. Y. Saillard, D. Grandjean, P. Caillet, A. Le Beuze, *J. Organomet. Chem.* **1980**, *190*, 371.

[38] Y. Li, B. Sztáray, T. Baer, *J. Am. Chem. Soc.* **2001**, *123*, 9388.

[39] B. Sztáray, T. Baer, *J. Am. Chem. Soc.* **2000**, *122*, 9219.

[40] Y. Li, J. E. McGrady, T. Baer, *J. Am. Chem. Soc.* **2002**, *124*, 4487.

[41] B. Sztáray, T. Baer, *J. Phys. Chem. A* **2002**, *106*, 8046.

[42] D. Cozak, I. S. Butler, *Spectrosc. Lett.* **1976**, *9*, 673.

[43] I. S. Butler, D. Cozak, *Can. J. Spectrosc.* **1982**, *27*, 141.

[44] G. C. Barna, I. S. Butler, K. R. Plowman, *Can. J. Chem.* **1976**, *54*, 110.

[45] I. S. Butler, D. A. Johansson, *Inorg. Chem.* **1975**, *14*, 701.

[46] I. S. Butler, Z. H. Xu, R. S. Werbowyj, F. St.-Germain, *Appl. Spectrosc.* **1987**, *41*, 149.

[47] D. L. Lichtenberger, R. F. Fenske, *Inorg. Chem.* **1976**, *15*, 2015.

[48] C. I. Pongor, Z. Gengeliczki, B. Sztáray, manuscript in preparation

[49] J. Thiele, *Ber. Deut. Chem. Ges.* **1901**, *34*, 68.

[50] T. J. Kealy, P. L. Pauson, *Nature* **1951**, *168*, 1039.

[51] E. O. Fischer, W. Pfab, *Z. Naturforsch. B* **1952**, *7*, 377.

[52] G. Wilkinson, M. Rosenblum, M. C. Whiting, R. B. Woodward, *J. Am. Chem. Soc.* **1952**, *74*, 2125.

[53] R. B. Woodward, M. Rosenblum, M. C. Whiting, *J. Am. Chem. Soc.* **1952**, *74*, 3458.

[54] N. J. Long, *Metallocenes*, Blackwell Science, Oxford, **1998**.

[55] J. W. Rabalais, *J. Chem. Phys.* **1972**, *57*, 1185.

[56] C. Cauletti, J. C. Green, M. R. Kelly, P. Powell, J. van Tilborg, J. Robbins, J. Smart, *J. Electron. Spectrosc. Rel. Phenom.* **1980**, *19*, 327.

[57] S. Evans, M. L. Green, B. Jewitt, G. H. King, A. F. Orchard, *J. Chem. Soc., Faraday Trans. 2* **1974**, *70*, 356.

[58] T. A. Albright, *Tetrahedron* **1982**, *38*, 1339.

[59] L. Resconi, L. Cavallo, A. Fait, F. Piemontesi, *Chem. Rev.* **2000**, *100*, 1253.

[60] G. G. Hlatky, *Chem. Rev.* **2000**, *100*, 1347.

[61] C. P. Lenges, M. Brookhart, B. E. Grant, *J. Organomet. Chem.* **1997**, *528*, 199.

[62] X. X. Luo, X. Zhao, S. S. Xu, B. Q. Wang, *Polymer* **2009**, *50*, 796.

[63] R. Blom, I. M. Dahl, O. Swang, *J. Catal.* **2000**, *194*, 352.

[64] M. Hoshino, F. Ebisawa, *J. Appl. Polym. Sci.* **1998**, *70*, 441.

[65] P. A. Dowben, O. Kizilkaya, J. Liu, B. Montag, K. Nelson, I. Sabirianov, J. I. Brand, *Mater. Lett.* **2009**, *63*, 72.

[66] L. Brissoneau, R. Sahnoun, C. Mijoule, C. Vahlas, *J. Electrochem. Soc.* **2000**, *147*, 1443.

[67] R. Xiang, G. H. Luo, Z. Yang, Q. Zhang, W. Z. Qjan, F. Wei *Mater. Lett.* **2009**, *63*, 84.

[68] I. Kunadian, R. Andrews, M. P. Menguc, D. Quian, *Chem. Eng. Sci.* **2009**, *64*, 1503.

[69] R. M. Yadav, P. S. Dobal, T. Shripathi, R. S. Katiyar, O. N. Srivastava, *Nanoscale Res. Lett.* **2009**, *4*, 197.

[70] Y. Li, B. Sztáray, T. Baer, *J. Am. Chem. Soc.* **2002**, *124*, 5843.

[71] J. Müller, L. D'Or, *J. Organomet. Chem.* **1967**, *10*, 313.

[72] S. Pignataro, F. P. Lossing, *J. Organomet. Chem.* **1967**, *10*, 531.

[73] J. P. Puttemans, A. Hanson, *Ing. Chim.* **1971**, *53*, 17.

[74] G. M. Begun, R. N. Compton, *J. Chem. Phys.* **1973**, *58*, 2271.

[75] J. Opitz, *Int. J. Mass Spectrom.* **2003**, *225*, 115.

[76] P. Schissel, D. J. McAdoo, E. Hedaya, D. W. McNeil, *J. Chem. Phys.* **1968**, *49*, 5061.

[77] G. D. Flesch, G. A. Junk, H. J. Svec, *J. Chem. Soc., Dalton Trans.* **1972**, 1102.

[78] C.-Y. Lin, R. C. Dunbar, *J. Phys. Chem.* **1995**, *99*, 1754.

[79] J. W. Warren, *Nature* **1950**, *165*, 810.

[80] Y. Li, T. Baer, *J. Phys. Chem. A* **2002**, *106*, 9820.

[81] M. K. Beyer, *Mass Spectrom. Rev.* **2007**, *26*, 517.

[82] N. G. Tsierkezos, J. Roithová, D. Schröder, I. E. Molinou, H. Schwarz, *J. Chem. Phys. B* **2008**, *112*, 4365.

[83] B. Jagoda-Cwiklik, P. Jungwirth, L. Rulíšek, P. Milko, J. Roithová, J. Lemaire, P. Maitre, J. M. Ortega, D. Schröder, *Chem. Phys. Chem.* **2007**, *8*, 1629.

[84] F. Tureček, *Mass Spectrom. Rev.* **2007**, *26*, 563.

[85] J. Roithová, D. Schröder, *Coord. Chem. Rev.* **2009**, *253*, 666.

[86] T. Lino, K. Ohashi, K. Inoue, K. Judai, N. Nishi, H. Sekiya, *J. Chem. Phys.* **2007**, *126*, 194302.

[87] K. Inoue, K. Ohashi, T. Lino, K. Judai, N. Nishi, H. Sekiya, *Phys. Chem. Chem. Phys.* **2007**, *9*, 4793.

[88] B. J. Duncombe, K. Duale, A. Buchanan-Smith, A. J. Stace, *J. Phys. Chem. A* **2007**, *111*, 5158.

[89] A. Bérces, T. Nukada, P. Margl, T. Ziegler, *J. Phys. Chem. A* **1999**, *103*, 9693.

[90] A. J. Stace, *J. Phys. Chem. A* **2002**, *106*, 7993.

[91] A. Pasquarello, I. Petri, P. S. Salmon, O. Parisel, R. Car, É. Tóth, D. H. Powell, H. E. Fischer, L. Helm, A. E. Merbach, *Science* **2001**, *291*, 856.

[92] J. Blumberger, L. Bernasconi, I. Tavernelli, R. Vuilleumier, M. Sprik, *J. Am. Chem. Soc.* **2004**, *126*, 3928.

[93] L. Puskar, H. Cox, A. Goren, G. D. C. Aitken, A. J. Stace, *Faraday Discuss.* **2003**, *124*, 259.

[94] M. Gerloch, *Inorg. Chem.* **1981**, *20*, 638.

[95] J. Chaboy, A. Muñoz-Páez, P. J. Merkling, E. S. Marcos, *J. Chem. Phys.* **2006**, *124*, 064509.

[96] N. R. Walker, R. R. Wright, P. E. Barran, J. N. Murell, A. J. Stace, *J. Am. Chem. Soc.* **2001**, *123*, 4223.

[97] W. Levason, M. D. Spicer, *Coord. Chem. Rev.* **1987**, *76*, 45.

[98] S. Riedel, M. Kaupp, *Coord. Chem. Rev.* **2009**, *253*, 606.

[99] T. V. Popova, N. V. Aksenova, *Russ. J. Coord. Chem.* **2003**, *29*, 803.

[100] R. M. Roat-Malone, *Bioinorganic Chemistry – A Sort Course*, John Wiley & Sons, Hoboken, **2002**.

[101] W. Harnischmacher, R. Hoppe, *Angew. Chem., Int. Ed.* **1973**, *12*, 582.

[102] L. Basumallick, R. K. Szilagyi, Y. Zhao, J. P. Shapleigh, C. P. Scholes, E. I. Solomon, *J. Am. Chem. Soc.* **2003**, *125*, 14784.

[103] L. Basumallick, R. Sarangi, S. D. George, B. Elmore, A. B. Hooper, B. Hedman, K. O. Hodgson, E. I. Solomon, *J. Am. Chem. Soc.* **2005**, *127*, 3531.

[104] E. I. Solomon, M. J. Baldwin, M. D. Lowery, *Chem. Rev.* **1992**, *92*, 521.

[105] J. Roithová, D. Schröder, *Chem. Eur. J.* **2008**, *14*, 2180.

[106] P. Milko, J. Roithová, D. Schröder, J. Lemaire, H. Schwarz, M. C. Holthausen, *Chem. Eur. J.* **2008**, *14*, 4318.

[107] P. Milko, J. Roithová, N. G. Tsierkezos, D. Schröder, *J. Am. Chem. Soc.* **2008**, *130*, 7186.

[108] A. Tintaru, L. Charles, P. Milko, J. Roithová, D. Schröder, *J. Phys. Org. Chem.* **2009**, *22*, 229.

[109] N. G. Tsierkezos, M. Buchta, P. Holý, D. Schröder, *Rapid Commun. Mass Spectrom.* **2009**, *23*, 1550.

[110] J. Roithová, P. Milko, *J. Am. Chem. Soc.* **2010**, *132*, 1281.

[111] E. I. Solomon, P. J. Clendeling, H. B. Gray, F. J. Grunthaner, *J. Am. Chem. Soc.* **1975**, *97*, 3878.

[112] K. Paraskevopoulos, M. Sundararajan, M. A. Hough, R. R. Eady, I. H. Hilier, S. S. Hasnain, *Dalton Trans.* **2006**, 3067. PDB code: 2CCW.

[113] M. T. Rodgers, J. R. Stanley, R. Amunugama, *J. Am. Chem. Soc.* **2000**, *122*, 10969.

[114] N. S. Rannulu, M. T. Rodgers, *J. Phys. Chem. A* **2007**, *111*, 3465.

[115] S. Than, H. Maeda, M. Irie, S. Itoh, K. Kikukawa, K. Mishima, *J. Phys. Chem. A* **2007**, *111*, 5988.

[116] N. S. Rannulu, R. Amunugama, Z. Yang, M. T. Rodgers, *J. Phys. Chem. A* **2004**, *108*, 6385.

[117] R. Amunugama, M. T. Rodgers, *J. Phys. Chem. A* **2001**, *105*, 9883.

[118] T. Baer, J. A. Booze, K. M. Weitzel, in *Vacuum Ultraviolet Photoionization and Photodissociation of Molecules and Clusters, p. 259*, C. Y. Ng (ed), World Scientific, Singapore, **1991**.

[119] F. S. Huang, R. C. Dunbar, *J. Am. Chem. Soc.* **1990**, *112*, 8167.

[120] C. Lifshitz, *Int. J. Mass Spectrom. Ion Proc.* **1991**, *106*, 159.

[121] P. B. Armentrout, *Top. Curr. Chem.* **2003**, *225*, 233.

[122] A. Colorado, J. S. Brodbelt, *J. Am. Soc. Mass. Spectrom.* **1996**, *7*, 1116.

[123] M. Satterfield, J. S. Brodbelt, *Inorg. Chem.* **2001**, *40*, 5393.

[124] M. L. Reyzer, J. S. Brodbelt, S. M. Kerwin, D. Kumar, *Nucleic Acids Res.* **2001**, *29*, E103.

[125] W. M. David, J. S. Brodbelt, *J. Am. Soc. Mass. Spectrom.* **2003**, *14*, 383.

[126] M. C. Crowe, J. S. Brodbelt, *J. Am. Soc. Mass. Spectrom.* **2003**, *14*, 1148.

[127] J. Zhang, J. S. Brodbelt, *J. Am. Soc. Mass. Spectrom.* **2005**, *16*, 139.

[128] K. J. Hart, S. A. McLuckey, *J. Am. Soc. Mass. Spectrom.* **1994**, *5*, 250.

[129] E. E. Jellen, A. M. Chappell, V. Ryzhov, *Rapid Commun. Mass Spectrom.* **2002**, *16*, 1799.

[130] L. A. Hayes, A. M. Chappell, E. E. Jellen, V. Ryzhov, *Int. J. Mass Spectrom.* **2003**, *227*, 111.

[131] N. Vinocur, V. Ryzhov, *J. Mass. Spectrom.* **2004**, *39*, 1268.

[132] T. Gozet, L. Huynh, D. K. Bohme, *Int. J. Mass Spectrom.* **2009**, *279*, 113.

[133] A. M. Fernandes, J. A. P. Coutinho, I. M. Marrucho, *J. Mass. Spectrom.* **2009**, *44*, 144.

[134] T. Waters, R. A. J. O'Hair, A. G. Wedd, *J. Am. Chem. Soc.* **2003**, *125*, 3384.

[135] R. A. J. O'Hair, A. K. Vrkic, P. F. James, *J. Am. Chem. Soc.* **2004**, *126*, 12173.

[136] G. N. Khairallah, R. A. J. O'Hair, *Angew. Chem., Int. Ed.* **2005**, *44*, 728.

[137] T. Punniyamurthy, S. Velusamy, J. Iqbal, *Chem. Rev.* **2005**, *105*, 2329.

[138] S.-J. Jin, P. K. Arora, L. M. Sayre, *J. Org. Chem.* **1990**, *55*, 3011.

[139] M. E. Bluhm, M. Ciesielski, H. Görls, O. Walter, M. Döring, *Inorg. Chem.* **2003**, *42*, 8878.

[140] P. Chaudhuri, M. Hess, U. Flörke, K. Wieghardt, *Angew. Chem., Int. Ed.* **1998**, *37*, 2217.

[141] P. Gamez, I. W. C. E. Arends, J. Reedjik, R. A. Sheldon, *Chem. Commun.* **2003**, 2414.

[142] W.-J. Yoo, C.-J. Li, *J. Org. Chem.* **2006**, *71*, 6266.

[143] Z. Li, C.-J. Li, *J. Am. Chem. Soc.* **2004**, *126*, 11810.

[144] M. Taki, S. Itoh, S. Fukuzumi, *J. Am. Chem. Soc.* **2001**, *123*, 6203.

[145] J. Shearer, C. X. Zhang, L. N. Zakharov, A. L. Rheingold, K. D. Karlin, *J. Am. Chem. Soc.* **2005**, *127*, 5469.

[146] O. Sander, A. Henß, C. Näther, C. Würtele, M. C. Holthausen, S. Schindler, F. Tuczek, *Chem. Eur. J.* **2008**, *14*, 9714.

[147] C. A. Schalley, R. Wesendrup, D. Schröder, T. Weiske, H. Schwarz, *J. Am. Chem. Soc.* **1995**, *117*, 7711.

[148] C. A. Schalley, R. Wesendrup, D. Schröder, K. Schroeter, H. Schwarz, *J. Am. Chem. Soc.* **1995**, *117*, 12235.

[149] R. Wesendrup, C. A. Schalley, D. Schröder, H. Schwarz, *Chem. Eur. J.* **1995**, *1*, 608.

[150] N. Taniguchi, *J. Org. Chem.* **2006**, *71*, 7874.

[151] R. P. Houser, J. A. Halfen, V. G. Young, N. J. Blackburn, W. B. Tolman, *J. Am. Chem. Soc.* **1995**, *117*, 10745.

[152] S. Itoh, M. Nagagawa, S. Fukuzumi, *J. Am. Chem. Soc.* **2001**, *123*, 4087.

[153] Y. Ueno, Y. Tachi, S. Itoh, *J. Am. Chem. Soc.* **2002**, *124*, 12428.

[154] T. Kondo, S.-Y. Uenoyama, K.-I. Fujita, T.-A. Mitsudo, *J. Am. Chem. Soc.* **1999**, *121*, 482.

[155] T. Gärtner, W. Henze, R. M. Gschwind, *J. Am. Chem. Soc.* **2007**, *129*, 11362.

[156] E. R. Bartholomew, S. H. Bertz, S. Cope, M. Murphy, C. A. Ogle, *J. Am. Chem. Soc.* **2008**, *130*, 11244.

[157] W. Henze, T. Gärtner, R. M. Gschwind, *J. Am. Chem. Soc.* **2008**, *130*, 13718.

[158] P. Brandt, M. Södergren, P. G. Andersson, P.-O. Norby, *J. Am. Chem. Soc.* **2000**, *122*, 8013.

[159] T. Cohen, J. Wood, A. G. Dietz, *Tetrahedron Lett.* **1974**, *40*, 3555.

[160] C. Savarin, J. Srogl, L. S. Liebeskind, *Org. Lett.* **2002**, *4*, 4309.

[161] J. Hyvl, J. Srogl, *Eur. J. Org. Chem.* **2010**, 2849.

[162] M. Chakraborty, K. J. Jin, A. C. Brewer, H.-L. Peng, M. S. Platz, M. Novak, *Org. Lett.* **2009**, *11*, 4862.

[163] C. Rodrigues-Rodrigues, N. S. de Groot, A. Rimola, A. Alvarez-Larena, V. Lloveras, J. Vidal-Gancedo, S. Ventura, J. Vendrell, M. Sodupe, P. Gonzalez-Duarte, *J. Am. Chem. Soc.* **2009**, *131*, 1436.

[164] B. Brehm, E. v. Puttkamer, *Z. Naturforsch. A* **1967**, *22*, 8.

[165] A. S. Werner, T. Baer, *J. Chem. Phys.* **1975**, *62*, 2900.

[166] O. Dutuit, T. Baer, C. Metayer, J. Lemaire *Int. J. Mass Spectrom. Ion Proc.* **1991**, *110*, 67.

[167] P. R. Das, T. Nishimura, G. G. Meisels, *J. Phys. Chem.* **1985**, *89*, 2808.

[168] H. M. Rosenstock, R. Stockbauer, A. C. Parr, *J. Chem. Phys.* **1980**, *73*, 773.

[169] K. Norwood, J. H. Guo, C. Y. Ng, *J. Chem. Phys.* **1989**, *90*, 2995.

[170] K. M. Weitzel, J. Mahnert, H. Baumgartel, *Ber. Bunsenges. Phys. Chem.* **1993**, *97*, 134.

[171] R. Stockbauer, *J. Chem. Phys.* **1973**, *58*, 3800.

[172] R. Thissen, C. Alcaraz, J. W. Hepburn, M. Vervloet, O. Dutuit, *Int. J. Mass Spectrom.* **2000**, *199*, 201.

[173] J. W. Keister, T. Baer, M. Evans, C. Y. Ng, C.-W. Hsu, *J. Phys. Chem. A* **1997**, *101*, 1866.

[174] J. A. Booze, T. Baer, *J. Chem. Phys.* **1993**, *98*, 186.

[175] O. A. Mazyar, T. Baer, *Chem. Phys. Lett.* **1998**, *288*, 327.

[176] T. Baer, Y. Li, *Int. J. Mass Spectrom.* **2002**, *219*, 381.

[177] T. Baer, B. Sztáray, J. P. Kercher, A. F. Lago, A. Bödi, C. Skull, D. Palathinkal, *Phys. Chem. Chem. Phys.* **2005**, *7*, 1507.

[178] K. Furuya, K. Kimura, T. Hirayama, *J. Chem. Phys.* **1992**, *97*, 1022.

[179] D. M. Smith, R. P. Tuckett, K. R. Yoxall, K. Codling, P. A. Harherly, *Chem. Phys. Lett.* **1993**, *216*, 493.

[180] T. Baer, W. B. Peatman, E. W. Schlag, *Chem. Phys. Lett.* **1969**, *4*, 243.

[181] R. Spohr, P. M. Guyon, W. A. Chupka, J. Berkowitz, *Rev. Sci. Instrum.* **1971**, *42*, 1872.

[182] T. Hsieh, J. Gilman, M. Meiss, G. G. Meisels, P. M. Hierl, *Int. J. Mass Spectrom. Ion Proc.* **1980**, *36*, 317.

[183] B. P. Tsai, T. Baer, M. L. Horowitz, *Rev. Sci. Instrum.* **1974**, *45*, 494.

[184] B. Sztáray, T. Baer, *Rev. Sci. Instrum.* **2003**, *74*, 3763.

[185] Z. Gengeliczki, L. Szepes, B. Sztáray, T. Baer, *J. Phys. Chem. A* **2007**, *111*, 7542.

[186] J. P. Kercher, Z. Gengeliczki, B. Sztáray, T. Baer, *J. Phys. Chem. A* **2007**, *111*, 16.

[187] B. Hornung, A. Bodi, C. I. Pongor, Z. Gengeliczki, T. Baer, B. Sztáray, *J. Phys. Chem. A* **2009**, *113*, 8091.

[188] W. Henderson, J. S. McIndoe, *Mass Spectrometry of Inorganic, Coordination and Organometallic Compounds: Tools – Techniques – Tips*, John Wiley & Sons, England, **2005**.

[189] N. B. Cech, C. J. Enke, *Mass Spectrom. Rev.* **2001**, *20*, 362.

[190] P. Jayaweera, A. T. Blades, M. G. Ikonomou, P. Kebarle, *J. Am. Chem. Soc.* **1990**, *112*, 2452.

[191] M. Dole, L. L. Mack, R. L. Hines, R. C. Mobley, L. D. Ferguson, M. B. Alice, *J. Chem. Phys.* **1968**, *49*, 2240.

[192] M. Yamashita, J. B. Fenn, *J. Phys. Chem.* **1984**, *88*, 4451.

[193] M. Yamashita, J. B. Fenn, *J. Phys. Chem.* **1984**, *88*, 4671.

[194] J. B. Fenn, *J. Am. Soc. Mass. Spectrom.* **1993**, *4*, 524.

[195] see: http://nobelprize.org/

[196] P. Kebarle, M. Peschke, *Analytica Chimica Acta* **2000**, *406*, 11.

[197] J. V. Iribarne, B. A. Thomson, *J. Chem. Phys.* **1976**, *64*, 2287.

[198] D. Schröder, T. Weiske, H. Schwarz, *Int. J. Mass Spectrom.* **2002**, *219*, 729.

[199] R. G. Cooks, R. E. Kaiser, *Acc. Chem. Res.* **1990**, *23*, 213.

[200] R. E. March, *J. Mass. Spectrom.* **1997**, *32*, 351.

[201] W. Paul, H. Reinhard, V. Zahn, *Z. Phys.* **1959**, *156*, 1.

[202] R. A. J. O'Hair, *Chem. Commun.* **2006**, 1469.

[203] S. Gronert, *Mass Spectrom. Rev.* **2005**, *24*, 100.

[204] D. Schröder, M. Engeser, M. Brönstrup, C. Daniel, J. Spandl, H. Hartl, *Int. J. Mass Spectrom.* **2003**, *228*, 743.

[205] P. Gruene, C. Trage, D. Schröder, H. Schwarz, *Eur. J. Inorg. Chem.* **2006**, 4546.

[206] T. Gozet, L. Huynh, D. K. Bohme, *Int. J. Mass Spectrom.* **2009**, *279*, 113.

[207] A. Tintaru, J. Roithová, D. Schröder, L. Charles, I. Jušinski, Z. Glasovac, M. Eckert-Maksić, *J. Phys. Chem. A* **2008**, *112*, 12097.

[208] Normalized collision energy^{TM}. Finnigan Product Support Bull. 104. http://www.thermo.com/eThermo/CMA/PDFs/Articles/articlesFile_21418.pdf

[209] B. Asamoto, R. C. Dunbar, *J. Phys. Chem.* **1987**, *91*, 2804.

[210] R. C. Dunbar, J. H. Chen, H. Y. So, B. Asamoto, *J. Chem. Phys.* **1987**, *86*, 2081.

[211] W. A. Chupka, *J. Chem. Phys.* **1959**, *30*, 191.

[212] C. Lifshitz, *Eur. J. Mass Spec.* **2002**, *8*, 85.

[213] M. R. Rodgers, P. B. Armentrout, *J. Chem. Phys.* **1998**, *109*, 1787.

[214] L. S. Kassel, *J. Phys. Chem.* **1928**, *32*, 225.

[215] O. K. Rice, H. C. Ramsperger, *J. Am. Chem. Soc.* **1927**, *49*, 1617.

[216] O. K. Rice, H. C. Ramsperger, *J. Am. Chem. Soc.* **1928**, *50*, 617.

[217] R. A. Marcus, O. K. Rice, *J. Phys. Colloid Chem.* **1951**, *55*, 894.

[218] H. M. Rosenstock, M. B. Wallenstein, A. L. Wahrhaftig, H. Eyring, *Proc. Natl. Acad. Sci.* **1952**, *38*, 667.

[219] T. Baer, W. L. Hase, *Unimolecular Reaction Dynamics: Theory and Experiments*, Oxford University Press, New York, **1996**.

[220] B. C. Garrett, D. G. Truhlar, *J. Phys. Chem.* **1980**, *84*, 805.

[221] W. H. Miller, *Acc. Chem. Res.* **1976**, *9*, 306.

[222] D. L. Bunker, M. Pattengill, *J. Chem. Phys.* **1968**, *48*, 772.

[223] W. L. Hase, *J. Chem. Phys.* **1972**, *57*, 730.

[224] W. L. Hase, *J. Chem. Phys.* **1976**, *64*, 2442.

[225] D. M. Wardlaw, R. A. Marcus, *Chem. Phys. Lett.* **1984**, *110*, 230.

[226] D. M. Wardlaw, R. A. Marcus, *J. Chem. Phys.* **1985**, *83*, 3462.

[227] W. J. Chesnavich, *J. Chem. Phys.* **1986**, *84*, 2615.

[228] S. J. Klippenstein, R. A. Marcus, *J. Chem. Phys.* **1989**, *91*, 2280.

[229] F. H. Mies, *J. Chem. Phys.* **1969**, *51*, 798.

[230] A. I. Maergoiz, E. E. Nikitin, J. Troe, V. G. Ushakov, *J. Chem. Phys.* **2002**, *117*, 4201.

[231] J. Troe, V. G. Ushakov, A. A. Viggiano, *Z. Phys. Chem.* **2005**, *219*, 715.

[232] J. Troe, V. G. Ushakov, A. A. Viggiano, *Z. Phys. Chem.* **2005**, *219*, 699.

[233] L. Zülicke, A. Merkel, *Int. J. Quantum Chem.* **1990**, *38*, 191.

[234] J. Troe, V. G. Ushakov, A. A. Viggiano, *J. Phys. Chem. A* **2006**, *110*, 1491.

[235] J. Troe, *Z. Phys. Chem.* **2009**, *223*, 347.

[236] J. C. Light, *J. Chem. Phys.* **1964**, *40*, 3221.

[237] P. Pechukas, J. C. Light, *J. Chem. Phys.* **1965**, *42*, 3281.

[238] B. Sztáray, A. Bodi, T. Baer, *J. Mass. Spectrom.* **2010**, *45*, 1233.

[239] K. S. Pitzer, *Quantum Chemistry*, Prentice Hall, New York, **1953**.

[240] T. Beyer, D. F. Swinehart, *ACM Commun.* **1973**, *16*, 379.

[241] S. H. Vosko, L. Wilk, M. Nusair, *Can. J. Phys.* **1980**, *58*, 1200.

[242] C. Lee, W. Yang, R. G. Parr, *Phys. Rev. B* **1988**, *37*, 785.

[243] A. D. Becke, *Phys. Rev. A* **1988**, *38*, 3098.

[244] A. D. Becke, *J. Chem. Phys.* **1993**, *98*, 5648.

[245] P. J. Stephens, F. J. Devlin, C. F. Chabalowski, A. D. Becke, M. J. Frisch, *J. Phys. Chem.* **1994**, *98*, 11623.

[246] C. Cramer, D. Truhlar, *Phys. Chem. Chem. Phys.* **2009**, *11*, 10757.

[247] R. Krishnan, J. S. Binkley, R. Seeger, J. A. Pople, *J. Chem. Phys.* **1980**, *72*, 650.

[248] J.-P. Blaudeau, M. P. McGrath, L. A. Curtiss, L. Radom, *J. Chem. Phys.* **1997**, *107*, 5016.

[249] A. J. H. Wachters, *J. Chem. Phys.* **1970**, *52*, 1033.

[250] P. J. Hay, *J. Chem. Phys.* **1977**, *66*, 4377.

[251] A. Schaefer, C. Huber, R. Ahlrichs, *J. Chem. Phys.* **1994**, *100*, 5829.

[252] A. Schaefer, H. Horn, R. Ahlrichs, *J. Chem. Phys.* **1992**, *97*, 2571.

[253] T. Clark, J. Chandrasekhar, G. W. Spitznagel, P. v. R. Schleyer, *J. Comput. Chem.* **1983**, *4*, 294.

[254] M. J. Frisch, J. A. Pople, J. S. Binkley, *J. Chem. Phys.* **1984**, *80*, 3265.

[255] R. Krishnan, G. W. Trucks, *J. Chem. Phys.* **1989**, *91*, 1062.

[256] S. F. Boys, F. Bernardi, *Mol. Phys.* **1970**, *19*, 553.

[257] D. V. Dearden, K. Hayashibara, J. L. Beauchamp, N. J. Kirchner, P. A. M. Van Koppen, M. T. Bowers, *J. Am. Chem. Soc.* **1989**, *111*, 2401.

[258] R. H. Schultz, K. C. Crellin, P. B. Armentrout, *J. Am. Chem. Soc.* **1991**, *113*, 8590.

[259] M. J. Frisch, G. W. Trucks, H. B. Schlegel, G. E. Scuseria, M. A. Robb, J. R. Cheeseman, J. A. Montgomery, Jr., T. Vreven, K. N. Kudin, J. C. Burant, J. M. Millam, S. S. Iyengar, J. Tomasi, V. Barone, B. Mennucci, M. Cossi, G. Scalmani, N. Rega, G. A. Petersson, H. Nakatsuji, M. Hada, M. Ehara, K. Toyota, R. Fukuda, J. Hasegawa, M. Ishida, T. Nakajima, Y. Honda, O. Kitao, H. Nakai, M. Klene, X. Li, J. E. Knox, H. P. Hratchian, J. B. Cross, V. Bakken, C. Adamo, J. Jaramillo, R. Gomperts, R. E. Stratmann, O. Yazyev, A. J. Austin, R. Cammi, C. Pomelli, J. W. Ochterski, P. Y. Ayala, K. Morokuma, G. A. Voth, P. Salvador, J. J. Dannenberg, V. G. Zakrzewski, S. Dapprich, A. D. Daniels, M. C. Strain, O. Farkas, D. K. Malick, A. D. Rabuck, K. Raghavachari, J. B. Foresman, J. V. Ortiz, Q. Cui, A. G. Baboul, S. Clifford, J. Cioslowski, B. B. Stefanov, G. Liu, A. Liashenko, P. Piskorz, I. Komaromi, R. L. Martin, D. J. Fox, T. Keith, M. A. Al-Laham, C. Y. Peng, A. Nanayakkara, M. Challacombe, P. M. W. Gill, B. Johnson, W. Chen, M. W. Wong, C. Gonzalez, J. A. Pople, *Gaussian 03, Revision E.01*, Gaussian, Inc., Wallingford CT, **2004**.

[260] W. Humphrey, A. Dalke, K. Schulten, *J. Molec. Graphics* **1996**, *14*, 33.

[261] I. S. Butler, A. E. Fenster, *J. Chem. Soc. D, Chem. Commun.* **1970**, 933.

[262] A. E. Fenster, I. S. Butler, *Can. J. Chem.* **1972**, *50*, 598.

[263] I. S. Butler, N. J. Coville, A. E. Fenster, *Inorg. Synth.* **1973**, *16*, 53.

[264] I. S. Butler, N. J. Coville, D. Cozak, S. R. Desjardins, A. E. Fenster, K. R. Plowman, D. A. Slack, M. C. Baird, *Inorg. Synth.* **1979**, *19*, 188.

[265] I. S. Butler, D. Cozak, S. R. Stobart, *J. Chem. Soc., Chem. Commun.* **1975**, 103.

[266] I. S. Butler, D. Cozak, S. R. Stobart, K. R. Plowman, P. V. Yaneff, R. O. Harris, *Inorg. Synth.* **1979**, *19*, 193.

[267] D. D. Wagman, W. H. E. Evans, V. B. Parker, R. H. Schum, I. Halow, S. M. Mailey, K. L. Churney, R. L. Nuttal, *The NBS Tables of Chemical Thermodynamic Properties, J. Phys. Chem. Ref. Data*, Vol. 11, Suppl. 2, NSRDS, U.S. Government Printing Office, Washington DC, **1982**.

[268] M. W. Chase, *NIST-JANAF Thermochemical Tables, J. Phys. Chem. Ref. Data Monogr.*, 4th edition, **1998**.

[269] H. Okabe, *J. Chem. Phys.* **1972**, *56*, 4381.

[270] J. D. Cox, D. D. Wagman, V. A. Medvedev, *CODATA Key Values for Thermodynamics*, Hemisphere Publishing Corp., New York, **1984**.

[271] C. A. Deakyne, L. Li, W. Zheng, D. Xu, J. F. Liebman, *J. Chem. Thermodyn.* **2002**, *34*, 185.

[272] H. M. Rosenstock, K. Draxl, B. W. Steiner, J. T. Herron, *Energetics of gaseous ions, J. Phys. Chem. Ref. Data*, Vol. 6, American Chemical Society, Washington DC, **1977**.

[273] H. Palm, C. Alcaraz, P. Milié, O. Dutuit, *Int. J. Mass Spectrom.* **2006**, *249*, 31.

[274] M. F. Ryan, D. E. Richardson, D. L. Lichtenberger, N. E. Gruhn, *Organometallics* **1994**, *13*, 1190.

[275] M. F. Ryan, J. R. Eyler, D. E. Richardson, *J. Am. Chem. Soc.* **1992**, *114*, 8611.

[276] D. E. Richardson, *Inorg. Chem.* **1993**, *32*, 1809.

[277] W. Stevens, B. Sztáray, N. Shuman, T. Baer, J. Troe, *J. Phys. Chem. A* **2009**, *113*, 573.

[278] N. S. Shuman, A. Bodi, T. Baer, *J. Phys. Chem. A* **2010**, *114*, 232.

[279] J. D. Faulk, R. C. Dunbar, *J. Am. Chem. Soc.* **1992**, *114*, 8596.

[280] S.-J. Han, M. C. Yang, C. H. Hwang, D. H. Woo, J. R. Hahn, H. Kang, Y. Chung, *Int. J. Mass Spectrom.* **1998**, *181*, 59.

[281] S. Barfuss, R.-H. Emrich, W. Hirschwald, P. A. Dowben, N. M. Boag, *J. Organomet. Chem.* **1990**, *391*, 209.

[282] F. Meyer, F. A. Khan, P. B. Armentrout, *J. Am. Chem. Soc.* **1995**, *117*, 9740.

[283] P. B. Armentrout, B. L. Kickel, *Organometallic Ion Chemistry*, Kluwer, Dordrecht, **1996**.

[284] H. Koizumi, M. Larsen, P. B. Armentrout, D. Feller, *J. Phys. Chem. A* **2003**, *107*, 2829.

[285] E.-L. Zins, C. Pepe, D. Schröder, *J. Mass. Spectrom.* **2010**, *45*, 1253.

[286] X. Wang, B. R. Sohnlein, S. Li, J. F. Fuller, D. S. Yang, *Can. J. Chem* **2007**, *85*, 714.

[287] D. Schröder, H. Schwarz, *Int. J. Mass Spectrom.* **2003**, *227*, 121.

[288] M. Ončák, P. Slavíček, *J. Comput. Chem.* **2010**, *31*, 2294.

[289] L. MacAleese, A. Simon, T. B. McMahon, J. M. Ortega, D. Scuderi, J. Lemaire, P. Maitre, *Int. J. Mass Spectrom.* **2006**, *249*, 14.

[290] N. C. Polfer, J. Oomens, *Phys. Chem. Chem. Phys.* **2007**, *9*, 3804.

[291] O. Dopfer, *J. Phys. Org. Chem.* **2006**, *19*, 540.

[292] D. Schröder, H. Schwarz, P. Milko, J. Roithová, *J. Phys. Chem. A* **2006**, *110*, 8346.

[293] D. Schröder, L. Ducháčková, I. Jušinski, M. Eckert-Maksić, J. Heyda, L. Tůma, P. Jungwirth, *Chem. Phys. Lett.* **2010**, *490*, 14.

[294] D. Schröder, J. Loos, H. Schwarz, R. Thissen, O. Dutuit, *Inorg. Chem.* **2001**, *40*, 3161.

[295] D. Schröder, J. Hrušák, I. C. Tornieporth-Oetting, T. M. Klapötke, H. Schwarz, *Angew. Chem., Int. Ed.* **1994**, *33*, 212.

[296] D. Schröder, J. Hrušák, R. H. Hertwig, W. Koch, P. Schwerdtfeger, H. Schwarz, *Organometallics* **1995**, *14*, 312.

[297] P. A. M. van Koppen, M. T. Bowers, E. R. Fisher, P. B. Armentrout, *J. Am. Chem. Soc.* **1994**, *116*, 3780.

[298] M. C. Holthausen, A. Fiedler, H. Schwarz, W. Koch, *Angew. Chem., Int. Ed.* **1995**, *34*, 2282.

[299] D. F. A. Ranatunga, Y. D. Hill, B. S. Freiser, *Organometallics* **1996**, *15*, 1242.

[300] D. Schröder, L. Ducháčková, J. Tarábek, M. Karwowska, K. J. Fijalkowski, M. Ončák, P. Slavíček, *J. Am. Chem. Soc.* **2011**, *133*, 2444.

[301] M. Remeš, J. Roithová, D. Schröder, E. D. Cope, C. Perera, S. N. Senadheera, K. Stensrud, C.-c. Ma, R. S. Givens, *J. Org. Chem.* **2011**, *76*, 2180.

[302] J. J. Dytrtová, M. Jakl, D. Schröder, E. Čadková, M. Komárek, *Rapid Commun. Mass Spectrom.* **2011**, *25*, 1037.

Abstract

Gas-phase studies of transition-metal compounds can provide valuable data and reveal important trends, which can significantly contribute to the understanding of numerous industrially and biochemically relevant systems. During my Ph.D., I have been involved in studying model compounds using two techniques. Threshold photoelectron photoion coincidence spectroscopy (TPEPICO) is appropriate for investigating unimolecular dissociation of energy-selected ions in the gas phase, with the ability of providing accurate bond energies and thermochemistry. Ion-trap mass spectrometry coupled with electrospray ionization (ESI-IT-MS) allows the gas-phase study of species present in solution, including their energy-dependent fragmentation using empirical calibration.

Employing TPEPICO, we addressed the effect of replacing carbonyls with carbon monosulfide or monoselenide on metal–ligand bond dissociation energies. Our results on the chalcocarbonyl analogues of $CpMn(CO)_3$ indicate that chalcocarbonyls are more strongly bound to the metal center than CO, which is in agreement with their better σ-donor, π-donor and π-acceptor properties. On the other hand, they do not influence the bonding of the other CO ligands.

We furthermore used the TPEPICO technique to study metal–Cp dissociation in chromocene, cobaltocene, and nickelocene ions. Motivated by the absence of reliable thermochemical data in the literature, we determined $[M–Cp]^+$ bond dissociation energies and described the accompanying dissociation and isomerization pathways. We explained the bond energy trend including earlier data on manganocene on the basis of a simple molecular orbital picture.

ESI-IT-MS experiments were carried out to examine the influence of the *N*-heterocyclic model ligand pyridine on the stability of gaseous copper(II) species. The $(py)_2CuCl^+$ ion was found to prefer the loss of the chlorine atom instead of the datively bound pyridine, which was explained to be the consequence of the formation of a species having ideal coordination sphere for copper(I). Furthermore, the measurements demonstrate the possibility of the determination of approximate fragmentation thresholds using IT-MS.

In a preliminary ESI-IT-MS study on an intramolecular redox reaction of imine disulfides, the reaction was found to be catalyzed by a single copper atom; a tentative mechanism could thus be formulated that supposedly involves copper(III) intermediates.

Összefoglalás

Átmenetifém-komplexek gázfázisú vizsgálatával értékes adatokat nyerhetünk, és fontos trendeket állapíthatunk meg, ami nagy mértékben hozzájárulhat ezen ipari és biokémiai szempontból is jelentős rendszerek megértéséhez. Ph.D. munkám során kétféle technikát használtam különböző modellvegyületek tanulmányozására. A küszöb fotoelektron–fotoion koincidencia spektroszkópia (TPEPICO) energiaszelektált ionok unimolekuláris disszociációjának analízisét teszi lehetővé, segítségével pontos kötési energiákat és termokémiai adatokat határozhatunk meg. Az elektrospray ionizációval kombinált ioncsapdás tömegspektrometria (ESI-IT-MS) oldatfázisban jelenlévő részecskék gázfázisú vizsgálatára alkalmas; empirikus kalibráció segítségével a fragmentáció ionenergiától való függéséről is kaphatunk információt.

A TPEPICO módszert használva vizsgáltuk karbonilligandumok szén-monoszulfidra vagy szén-monoszelenidre való cseréjének hatását a fém–ligandum kötési energiákra. A $CpMn(CO)_3$ kalkokarbonil-analogonjaira kapott eredményeink alapján a kalkokarbonilok erősebben kötődnek a fémcentrumhoz, mint a CO, ami összhangban van jobb σ-donor, π-donor és π-akceptor tulajdonságukkal. Nincs hatásuk ugyanakkor a többi CO ligandum kötődésére.

TPEPICO-val tanulmányoztuk a fém–Cp disszociációt kromocén, kobaltocén, és nikkelocén ionokban. Mivel megbízható adatok nem találhatók az irodalomban, meghatároztuk az $[M–Cp]^+$ kötési energiákat, és jellemeztük a kísérő disszociációs és izomerizációs utakat. A kötési energiákban tapasztalható trendet, felhasználva a manganocénre korábban mért adatot is, egy egyszerű molekulapálya-alapú modellel magyaráztuk.

ESI-IT-MS kísérleteket végeztünk annak érdekében, hogy feltárjuk egy *N*-heterociklusos modell-ligandum, a piridin, gázfázisú réz(II)-specieszek stabilitására gyakorolt hatását. A $(py)_2CuCl^+$ ion esetében megállapítottuk, hogy a klóratom vesztésével járó fragmentáció kedvezőbb, mint a datívan kötött piridinligandum leszakítása, amit a réz(I) számára megfelelőbb koordinációs szférával rendelkező komplex képződésével magyaráztunk. Ezek a mérések azt is alátámasztják, hogy az IT-MS segítségével lehetőség van közelítő fragmentációs küszöbenergiák meghatározására.

Imin-diszulfidok egy intramolekuláris redoxreakciójában előzetes ESI-IT-MS mérésekkel megállapítottuk, hogy a reakció katalíziséhez egy rézatom elegendő. Az eredmények alapján mechanizmusjavaslatot adtunk, mely szerint feltételezhető, hogy a folyamatban egy réz(III)-intermedier is részt vesz.